Die approbierte Originalversion dieser Dissertation ist in der Hauptbibliothek der Technischen Universität Wien aufgestellt und zugänglich.
http://www.ub.tuwien.ac.at

The approved original version of this thesis is available at the main library of the Vienna University of Technology.
http://www.ub.tuwien.ac.at/eng

TECHNISCHE UNIVERSITÄT WIEN
Vienna University of Technology

Dissertation

Fission Fragment Angular Distributions in Neutron-Induced Fission of ^{235}U Measured with a Time Projection Chamber

Ausgeführt zum Zwecke der Erlangung des akademischen Grades einer
Doktorin der technischen Wissenschaften
unter der Leitung von

Ao. Univ. Prof. Helmut Leeb
Institut Nummer E141
Atominstitut

eingereicht an der
Technischen Universität Wien
Fakultät für Physik

von

Dipl.-Ing. Verena Kleinrath
Matrikelnummer 0425437
Stickelberg 58, A-2812 Hollenthon

Wien, am 16. Dezember 2015

Zusammenfassung

Präzise Kerndaten spielen eine wichtige Rolle in allen Anwendungen der Kernphysik; die Qualität von Simulationen und Modellen ist abhängig von verfügbaren Daten und deren Messunsicherheiten. Die Winkelverteilungen von Spaltfragmenten der Neutronen-induzierten Kernspaltung können Aufschluss über die Form der Spaltbarriere und Energieniveaus am Sattelpunkt geben, beides wichtige Informationen für die theoretische Entwicklung von Spaltmodellen. Zusätzlich sind die Winkelverteilungen wertvolle Kenngrößen für die Bestimmung von relativen Spaltquerschnitten, wenn diese für die beiden verwendeten Isotope verschieden sind. Die "Neutron Induced Fission Fragment Tracking Experiment" (NIFFTE) Kooperation verwendet eine Time Projection Chamber (fissionTPC) um fundamentale Kerndaten mit hoher Präzision zu messen. Das neuartige Instrument erlaubt eine komplette dreidimensionale Rekonstruktion von Teilchenbahnen, die eine direkte Messung von Winkelverteilungen und Emissions-Anisotropien von Spaltfragmenten in der Neutronen-induzierten Kernspaltung ermöglicht. Die Analyse von Strahldaten, die am Los Alamos Neutron Science Center gemessenen wurden, liefert Winkelverteilungen für die Reaktion ^{235}U(n,f) als Funktion der Neutronenenergie von 160 keV bis 230 MeV. Das vorliegende ^{235}U(n,f) Anisotropieresultat gibt Aufschluss über die Struktur der Anisotropiekurve zwischen 1 und 20 MeV. In diesem Energiebereich folgt die Kurve dem Spaltwirkungsquerschnitt, was mit theoretischen Überlegungen im Rahmen des statistischen Modells der Kernspaltung übereinstimmt.

Abstract

Nuclear data play a vital role in nuclear energy and defense applications; the community heavily relies on simulations and modeling, and therefore on available data and their uncertainties. Fission fragment angular distributions in neutron-induced fission can provide insights into fission barrier shapes and level densities at the saddle point, both important quantities for fission theory developments. In addition, fragment emission anisotropies are valuable for precision cross section ratio measurements, if the distributions are different for the two isotopes used in the ratio. Available angular data is sparse, especially at neutron energies above 5 MeV. The Neutron Induced Fission Fragment Tracking Experiment (NIFFTE) collaboration employs a fission time projection chamber (fissionTPC) to measure fundamental nuclear data with unprecedented precision. The novel instrument enables complete three-dimensional tracking of charged particles providing a direct measurement of angular distributions and emission anisotropies of fission fragments in neutron-induced fission. Analysis of in-beam data collected at the Los Alamos Neutron Science Center provides angular distributions for ^{235}U(n,f) as a function of incident neutron energy from 160 keV to 230 MeV. The current ^{235}U(n,f) anisotropy result delivers new insights into the structure of the anisotropy curve between 1 and 20 MeV. The curve seems to follow the fission cross section closely in that energy range, which is consistent with theoretical considerations within the statistical model of nuclear fission.

Acknowledgments

Many people have contributed to this research project and actively supported me over the last five years. It has been quite a journey from Austria to Idaho, to New Mexico, and back, and I am grateful to all the people who have helped me along the way.

First, I want to thank my two advisors: Helmut Leeb at Vienna University of Technology, who gave me the freedom to follow my own path while still supporting me when needed. And Fredrik Tovesson at Los Alamos National Laboratory, who not only guided my research, but has become a trusted mentor always ready to offer words of wisdom and encouragement. I also want to thank my collaborators in the NIFFTE project, especially Lucas Snyder with whom I assembled and disassembled the TPC countless times: I learned so much from you and had a blast while doing so. And Tony Hill, who introduced me to the project and helped me get started.

My colleagues at Los Alamos National Laboratory deserve credit for making the lab a great place to work. Patrick Talou and Eric Lynn in theory division had an open door for me with my theory questions. A big thank you goes to all present and past members of the amazing 'team fission'. Brett, thanks for taking the TPC off my hands and always bringing a smile to everyone's face. And thank you Dana, queen of fission and connoisseur of Rhône varietals, for being my office mate and my friend. Denise and Daniel, my Austrian family in the US: Thanks for the Gulasch, the board game nights, and the discussions on covariance matrices. Thank you to many more friends in Los Alamos, who made this place a home and starting point to plenty of adventures: Heidi, Kathy,

Molly and Erik, and the wonderful bunch of people with the Pajarito Mountain Ski Patrol.

I would like to also express my gratitude to Los Alamos National Laboratory and Idaho State University for granting me graduate research positions. This work was additionally supported by the Austrian UNESCO Commission with a L'Oréal For Women in Science fellowship, the Austrian Marshall Plan Foundation with a Marshall Plan scholarship, and Vienna University of Technology with a Förderstipendium.

Lastly I want to thank those who stayed home but supported me unconditionally through this adventure: My friend Iris, my parents Ilse and Manfred, my sister Viktoria, and Hermann - the love of my life.

Contents

1 Introduction **1**

1.1 Nuclear Data and Fission Cross Sections 2

1.2 Predictive Fission Modeling 5

1.3 Document Structure 6

2 Theory **8**

2.1 An Introduction to Fission Theory 8

2.1.1 The Liquid Drop Model 9

2.1.2 The Fission Barrier 10

2.1.3 Shell Corrections 12

2.1.4 The Double-Humped Barrier 14

2.1.5 Statistical Model of Nuclear Reactions 14

2.2 Fission Fragment Angular Distributions 17

2.2.1 The Transition State Model 17

2.2.2 The Standard Saddle-Point Statistical Model 20

2.2.3 Neutron-Induced Fission of ^{235}U 22

2.2.4 Fission Fragment Anisotropy 23

3 Previous Work **24**

4 Experiment **27**

4.1 Gaseous Ionization Chambers 27
4.1.1 The Time Projection Chamber Technique 28
4.2 The fissionTPC 30
4.2.1 Hardware 31
4.2.2 Software 39
4.2.3 Author Contribution to Development 47
4.3 The Los Alamos Neutron Science Center 47
4.3.1 The Linear Accelerator 48
4.3.2 The Neutron Source 49
4.4 Run Configurations 50

5 Data Analysis **51**
5.1 Raw Data Reconstruction 51
5.2 Fission Fragment Identification 52
5.3 Neutron Time of Flight Calibration 53
5.3.1 The Photofission Peak 55
5.3.2 Flightpath Length 56
5.3.3 Neutron Energy 58
5.4 Wrap-Around Correction 59
5.5 Linear Momentum Transfer 62
5.6 Anisotropy Calculation 66
5.6.1 Angular Efficiency Normalization 66
5.6.2 Fitting the Angular Distributions 68
5.7 Uncertainties 71
5.7.1 Statistical Errors 71
5.7.2 Tracking Uncertainty 72
5.7.3 Fission Fragment Identification Uncertainty 74
5.7.4 Neutron Time of Flight Resolution 76

5.7.5 Wrap-Around Uncertainty 76
5.7.6 Momentum Transfer Uncertainty 77
5.7.7 Efficiency Normalization Uncertainty 78
5.7.8 Fit Selection Uncertainty 79
5.7.9 Fit Range Uncertainty 79
5.7.10 Target Contamination 81
5.7.11 Resulting Uncertainty Band 82
5.8 Covariances 83

6 Results and Discussion **87**
6.1 Anisotropy Result 87
6.2 Uncertainties and Correlations 93

7 Conclusions **97**

A Tabulated Anisotropy Result **i**

B Uncertainty Contributions **iv**

C Angular Distributions **vii**

List of Figures

2.1 Deformation energy contours as a function of quadrupole and hexadecapole deformations and the potential energy along the most favorable path to fission. 11
2.2 Shell corrections lead to a double-humped fission barrier with a second minimum right at the barrier maximum of the liquid drop model. 15
2.3 The highly deformed transition state nucleus behaves like a rigid symmetric spinning top and its quantum numbers J, K, and M define the angular distribution of fission fragments. 18

3.1 An overview of available fission fragment anisotropy data for neutron-induced fission of ^{235}U. 25

4.1 An overlay of simulated particle trajectories in the high data rate STAR TPC. 29
4.3 A schematic view of MICROMEGAS with the amplification gap between the micromesh and the anode. 31
4.4 A photograph of the fully assembled fissionTPC on the designated flightpath at LANSCE during the 2014/2015 run cycle. The front face is missing in the picture to showcase the electronics. 32

4.5 An exploded view of the fissionTPC components with the pressure vessel (1), anode planes (2) and the preamplification and EtherDAQ cards (3) of the data acquisition system mounted on the sides. 33
4.6 A schematic drawing of the fissionTPC with particle tracks coming off the target in the center of the cathode plane and the hexagonal structure of the pads on the micromesh anode. 34
4.7 The biasing of the fissionTPC with example potentials. The field cage resistors are actually voltage controlled and the bottom of the field cage is biased to the MICROMEGAS potential. 36
4.8 A close-up view of the pad plane surface. The gold coated hexagonal pads, their offset and the MICROMEGAS pillars are visible. 37
4.9 The latest version of the fissionTPC pad plane with the MICROMEGAS mesh installed. 37
4.10 Individual signals from different channels for a track from a ^{252}Cf source in the fissionTPC. 41
4.11 The Hough transform moves all combinatorics of a straight line hypothesis into a parameter space, where the highest occupancy bin corresponds to the most probable track. 43
4.12 The recursive prediction and filtering steps along a track and the smoothed estimate within the Kalman track fitter. 46
4.13 A schematic depiction of the LANSCE facility with the Lujan Center, WNR and the fissionTPC flightpath 90L, which is indicated with the turquoise coloring. 48

4.14 An aerial photograph of the LANSCE mesa with the linear accelerator building clearly visible to the right and the red circle indicating the area of target-2 and the home of the fissionTPC, flightpath 90L. 49

5.2 Track vertices for all fission fragments as determined by the energy selection. 54

5.3 Track length versus energy for all fission fragments selected for the anisotropy analysis. 54

5.4 The neutron time of flight spectrum for the selected fission fragments. 56

5.5 The total neutron cross section for ^{12}C versus incident neutron energy. 57

5.6 The neutron time of flight spectrum with a carbon filter in place. 57

5.8 The shape of the wrap-around fit describes the background in the time of flight spectrum. 61

5.9 The average kinetic energy in the fission event is determined by estimating the energy of an average light and average heavy fragment. 65

5.10 The thick backing target with actinide deposits on each side and fission fragments leaving the target material. 67

5.11 The angular distribution of fission fragments for incident neutron energies from 130 keV to 160 keV. 68

5.12 The normalized angular distributions are fitted with even order polynomials in $\cos(\theta)$ space. 69

5.13 The goodness of fit parameter, or reduced chi-square χ^2_ν, for the fits using Legendre polynomials of quadratic order over all neutron energies. 71

5.14 The reconstructed angular distribution of alpha particles from spontaneous decay at different drift speeds. 74
5.15 Different anisotropy results are obtained by varying the energy selection cut in steps of 2000 ADC units. 75
5.16 The difference between the simulated timing structure shape and the fit used to correct for wrap-around in the data is given in percent at various incident neutron energies. 77
5.17 The anisotropy result for including different orders in the polynomial fit. 80
5.18 The fit result changes when including only a limited range in the angular distribution. 81
5.19 A comparison between expected ^{235}U and contaminant isotope fission fragments in percent, obtained by multiplying the atomic percentage with the cross section for each isotope and given as percentage of the value obtained for ^{235}U. 82
5.20 The standard deviation σ in each energy bin seems to converge sufficiently with an increasing number of samples between the most extreme track energy selection cut limits. 86

6.1 The fission fragment anisotropy over neutron energy for the neutron-induced fission of ^{235}U, compared to the two most comprehensive data sets available in the literature. 89

C.1 The ^{235}U(n,f) angular distributions for incident neutron energies from 160 keV to 700 keV. viii
C.2 The ^{235}U(n,f) angular distributions for incident neutron energies from 700 keV to 1.64 MeV. ix

C.3 The ^{235}U(n,f) angular distributions for incident neutron energies from 1.64 to 4.39 MeV. x
C.4 The ^{235}U(n,f) angular distributions for incident neutron energies from 4.39 to 11.79 MeV. xi
C.5 The ^{235}U(n,f) angular distributions for incident neutron energies from 11.79 to 51.79 MeV. xii
C.6 The ^{235}U(n,f) angular distributions for incident neutron energies from 51.79 to 268.27 MeV. xiii

Chapter 1

Introduction

The process of nuclear fission is a highly complex many-body quantum mechanics problem. The dynamics of the nucleus on the path to scission are difficult to calculate and after over 75 years of fission research a lot is still to be discovered in order to fully understand the process. The fission fragment angular distributions presented in this thesis will fundamentally contribute to our knowledge of nuclear fission. As can be seen in chapter 3, angular data for neutron-induced fission of ^{235}U is still relatively sparse; especially continuous measurements that extend to higher neutron energies are lacking. The present measurement aims to add significantly to the current body of data by deducing angular distributions for ^{235}U(n,f) over a wide range of neutron energies up to several hundred MeV. The measurement's immediate impact will be two-fold: For one it will directly support the effort to measure precision fission cross sections, a much needed nuclear data quantity for applications. Secondly, the results can aid in the further development of predictive fission models.

1.1 Nuclear Data and Fission Cross Sections

'Nuclear data' is a term that generally encompasses a wide array of observables in nuclear fission and other nuclear reactions. Databases like the EXFOR (Experimental Nuclear Reaction Data) library maintained by the International Atomic Energy Agency [1] collect measurements and make them available to the community. EXFOR contains data from over 21000 nuclear reaction experiments. Nuclear data evaluations are generated by combining all available experimental data sets with input from model calculations and extensive error study. The evaluation reflects the best knowledge of the essential reaction observables and may therefore lead to lower uncertainties than those of individual measurements. The evaluation files are then benchmarked and made available to end users in libraries such as the ENDF/B library [2] with entries in ENDF (Evaluated Nuclear Data File) format. Other available libraries include JEFF (Joint Evaluated Fission and Fusion File [3]) and JENDL (Japanese Evaluated Neutron Data Library [4]).

Many observables, like fission cross sections for the most commonly used actinides, have already been measured and evaluated with very small uncertainties, often in the 2 - 5 % range. Recent advances in technology, however, call for even more precise nuclear data for applications. The nuclear fission community has expressed the need for additional data for advanced nuclear technologies like energy production using generation IV nuclear reactors, nuclear medicine, non-proliferation, or responsible stockpile-stewardship without testing [5]. Data is needed over a wide range of neutron energies; advances in fast reactor technology increase the need for data in neutron energy regimes above thermal energies. Additional well characterized experiments aid the evaluation process and reduce the uncertainties in nuclear data files, which in turn improves the accuracy in modeling and simulations of the mentioned applications. The experiments pre-

sented here will have a strong impact on nuclear data evaluations by providing fission observables over a wide range of neutron energies through using the neutron spectrum available at the Los Alamos Neutron Science Center (LANSCE) Weapons Neutrons Research (WNR) facility as well as employing a completely novel detection technology to the field of nuclear fission. Although the effect of fission fragment emission anisotropy has been observed for some time, data on fission fragment angular distributions available in the literature are very limited. That is most probably due to the fact that the angular information on fission fragments is impossible or difficult to obtain in detectors that have been used to study fission in the past, most commonly ionization chambers. The Neutron Induced Fission Fragment Tracking Experiment (NIFFTE) collaboration has now successfully added completely new capabilities to the field of nuclear fission research. The fission time projection chamber (fissionTPC) is a custom-designed time projection chamber to specifically study the fission process. The instrument makes use of technology that has been known in high energy physics for over 25 years and constitutes a major enhancement over detectors traditionally used in fission research. The fissionTPC provides three-dimensional tracking of all ionizing particles produced in the fission process. The detector has been developed, built and commissioned over the last few years and is now a fully operational physics experiment available to the toolbox of fission research.

While the study of angular distributions is an example of how the fissionTPC can provide insights into the mechanism of fission, the instrument's main purpose is to deliver a precise measurement of the neutron-induced ^{239}Pu fission cross section with small and well-understood uncertainties. The ambitious cross section campaign the NIFFTE collaboration is leading will provide precise nuclear data with low uncertainties as well as directly measure certain systematic uncertainties previous experiments have collectively suffered from. The angular

distribution measurement for neutron-induced fission of ^{235}U presented in this thesis will have an immediate impact on the cross section campaign. While the NIFFTE project eventually strives to measure the fission cross section of ^{239}Pu(n,f) as a ratio to the well-known hydrogen cross section, a precise ratio measurement of ^{239}Pu(n,f)/^{235}U(n,f) is a major milestone for the project and can already impact the existing ^{239}Pu cross section evaluation in the short term. Measurements of cross section ratios are a common practice in the field of nuclear physics: The target of interest is measured with respect to a well-known standard cross section, like ^{235}U(n,f) which is evaluated with uncertainties of about 1 %. If both targets are arranged in suitable geometry, sources of error - like neutron flux uncertainties - can be completely eliminated. The two different actinides are deposited on either side of a thick backing target and the fission cross section is measured by detecting fission fragments on either side of the target and producing a ratio. One can imagine that the detection efficiency for fission is limited; fission fragments will not leave the target at very steep angles parallel to the target surface because of energy straggling in the material. As angular distributions of fission fragments can vary greatly between different target isotopes and across neutron energies, knowledge of the different distributions is required to correct for the detection efficiency in the cross section ratio - the number of fragments lost can be different in the two isotopes. Recent precision measurements of cross section ratios at the JRC-IRMM in Geel [6] as well as by the n_TOF collaboration [7] mention the use of fission fragment angular distribution data for the efficiency correction to improve accuracy of the obtained ratios. The NIFFTE collaboration will correct the ^{239}Pu(n,f)/^{235}U(n,f) cross section ratio using angular distribution data from the current ^{235}U(n,f) experiment, as well as from a coinciding ^{239}Pu(n,f) measurement which is currently being analyzed.

1.2 Predictive Fission Modeling

Nuclear fission is a highly complicated process and previously parameterization of phenomenological models to fit experimental data was the standard. Now there is a paradigm shift towards deeper understanding and development of a complete theory that can predict the dynamics and resulting fission fragment properties. There has been a recent resurgence in theory efforts to further the understanding of the nuclear fission process, which could provide predictive power for systems inaccessible to measurements and support all nuclear applications as well as data evaluations. The experimental results of the angular distribution measurement can have immediate impact on the development of predictive fission models. The theoretical prediction of the fission dynamics is extremely challenging and still poses a puzzle to theorists. It is believed that in induced fission not only the chosen path to fission or fission mode, but also energy and shape configurations at the saddle point of the fission barrier determine the properties of the fission fragments. Little is known about the dynamics of fission, the configurations of the nucleus on the way from its ground state to developing into two separate fragments. The fission product evolution with respect to energy is information that will drive theoretical developments.

Fission fragment angular distributions are observables that are not easily accessible, but can lead towards valuable insights into the fission process. The angular distributions provide information on the state of the transition nucleus at the saddle point of the fission barrier. The nuclear configurations and shapes on the maximum of the fission barrier long before the nucleus splits into two fragments are in principal completely inaccessible to measurement, but the angular distributions deliver hints at those configurations. Angular distributions have famously driven theory development in the past, when Aage Bohr developed his transition state model in 1956 [8]. When nuclear fission was first discovered, it

was assumed that the fission fragments would be emitted isotropically. It was only in the early 1950s that anisotropic emission was first observed in photofission of ^{232}Th [9]. It is now known, thanks to Bohr's transition state theory, that due to the population of only a few discrete energy levels of the transition nucleus at the saddle point fission fragment emission at intermediate energies is anisotropic. One can even imagine a sort of transition state spectroscopy where iterative fitting of experimental angular distributions and theoretical predictions for certain configurations can identify the quantum mechanical state of the transition nucleus, as Loveland and Behkami showed for ^{234}U(n,f) [10, 11].

The theoretical interpretation of the present angular distribution results will be used to validate and improve predictive fission models in the future. One example is Los Alamos National Laboratory's AVXSF (average cross section fission) program, a statistical code to predict fission cross sections using a Hauser-Feshbach formalism [12, 13]. The transition states are calculated using single particle excitations, and angular distributions can provide constraints on the transition state parameters and therefore improve the cross section prediction capability. With a renewed interest in developing fundamental models for the fission process, the angular distributions provided in this thesis will be a timely physics result for current trends in theory.

1.3 Document Structure

This thesis provides angular distributions and angular anisotropy values (emission of fragments in beam direction versus perpendicular to beam) for the neutron-induced fission of ^{235}U over incident neutron energies from 160 keV to 230 MeV. The result will not only drive developments of theoretical models of fission as described above, but also directly aid in the ambitious cross section

campaign the NIFFTE project is leading. The following document contains a brief historic note on the discovery of nuclear fission and more recent developments towards modern theories to describe angular distributions of fission fragments in chapter 2. Chapter 3 presents previous measurements of fission fragment angular distributions. The detection technique using time projection chambers is described in chapter 4 along with the neutron source used in this study - the Weapons Neutron Research facility at the Los Alamos Neutron Science Center. The chapter also details the development of the fissionTPC detector used in this study and gives a brief overview of the author's contribution to the experimental setup. The author's principal focus and responsibility within the NIFFTE project was the measurement and analysis of angular distributions. Chapter 5 details the data analysis technique developed to extract angular distributions of fission fragments and anisotropy values from the fissionTPC data. The anisotropy result for ^{235}U(n,f) is presented and discussed in the context of previous measurements in chapter 6. Chapter 7 provides a brief summary and outlook towards future measurements with the fissionTPC.

Chapter 2

Theory

This chapter gives an overview of some established models of the fission process and the concepts and open questions motivating the current experiment and will put the objectives in a broader perspective. An introduction to fission physics leading up to the theory of fission fragment angular distributions is given.

2.1 An Introduction to Fission Theory

Fission is generally understood to be a process in which a heavy nucleus evolves into two fragments of comparable mass. The phenomenon was first reported by Hahn and Strassmann [14] in 1939. Meitner and Frisch [15] and Bohr and Wheeler [16, 17] presented theoretical explanations shortly thereafter based upon the idea of a charged liquid drop; thus assuming nuclear matter to behave like a liquid. The simplified picture of fission involves the parent nucleus elongating and gradually forming a neck in its center before the neck snaps and the system breaks into two new nuclei. The energy release in fission can be calculated from conservation of energy and is generally about 150 to 200 MeV, most of it manifests as the kinetic energy of the fission fragments. While the

discovery of fission was based on chemical methods, Frisch immediately measured the rather large energy release that he and Meitner had estimated in a first version of today's ionization chamber [18].

2.1.1 The Liquid Drop Model

The binding energy of the drop is expressed by the Bethe-Weizsäcker semi-empirical mass formula

$$E_B(N,Z) = a_V A - a_S A^{2/3} - a_C \frac{Z(Z-1)}{A^{1/3}} - a_A \frac{(N-Z)^2}{A} + \delta(N,Z), \qquad (2.1)$$

where A is the mass number, Z is the atomic or proton number and N is the neutron number of the nucleus. The first term of equation (2.1), the volume term, corresponds to the strong nuclear force between the neighboring nucleons and is therefore positive. The second term, the surface term, is a correction to the volume term and accounts for the smaller number of nearest neighbors for nucleons on the surface. The third term, the Coulomb term, reflects the repulsion between protons in the nucleus. The fourth term, the asymmetry term, describes the isospin dependence of the nuclear force. The quantity $\delta(N,Z)$ is the pairing term, which accounts for the fact that nuclei with an even number of protons or neutrons are stronger bound than those with an odd number. The Bethe-Weizsäcker formula paints a simple but rather realistic picture for the bulk of nuclei and therefore reasonable sets of parameters have been determined for equation (2.1) [19].

In the liquid drop model one describes the nucleus as an incompressible fluid. Thus on the basis of the Bethe-Weizsäcker formula the fission process is governed by the competition between the surface and the Coulomb term of equation (2.1). The deformation of the nucleus can be described by a multipole expansion in the spherical harmonics. If we assume rotational symmetry, Legendre polynomials

are sufficient and the deformation is

$$R(\theta) = \frac{R_0}{\lambda}\left[1 + \sum_n \beta_n P_n(cos\ \theta)\right], \tag{2.2}$$

where R_0 is the radius of an undistorted nucleus, λ is a scaling factor to conserve the volume and the coefficients β_n parameterize the multipolarity of the deformation. If only a small, axially symmetric, pure quadrupole deformation (only $\beta_2 \neq 0$) is considered, equation (2.2) reduces to

$$R(\theta) = R_0\left[1 + \beta_2 P_2(cos\ \theta)\right]. \tag{2.3}$$

The surface term then increases as $2/5\beta_2^2$ and the Coulomb term decreases as $-1/5\beta_2^2$; which yields

$$\Delta E_B = E_B(\beta_2) - E_B(0) \approx \beta_2^2\left(-\frac{2}{5}a_S A^{2/3} + \frac{1}{5}a_C\frac{Z(Z-1)}{A^{1/3}}\right). \tag{2.4}$$

Consequently, the condition for stability of the nucleus is

$$\frac{1}{5}\left(a_C\frac{Z(Z-1)}{A^{1/3}} - 2a_S A^{2/3}\right) < 0. \tag{2.5}$$

Therefore the fissility parameter,

$$x = \frac{a_C}{2a_S}\frac{Z(Z-1)}{A}, \tag{2.6}$$

introduced by Bohr and Wheeler [17] provides a criterion for fission. For $Z(Z-1)/A > 50$ the fissility parameter exceeds 1, which implies that nuclei with $Z(Z-1)/A > 50$ will undergo spontaneous fission according to the liquid drop model.

2.1.2 The Fission Barrier

The fission process is determined by the effective potential surface associated with the deformation of the nucleus. As already mentioned above this potential

surface is formed by the competition between the surface term and the Coulomb term in equation (2.1). When a nucleus stretches and evolves into two fragments the surface increases thus weakening the contribution of the nuclear force to binding. On the other hand the Coulomb repulsion reduces with deformation. With increasing deformation there arises a point of minimal binding which is equivalent to overcoming a barrier in the potential picture. The height and shape of this so-called fission barrier depend on the shape of the nucleus and all the terms in equation (2.1). The liquid drop model results in a fission barrier with a single hump. Experimental observations of the probability of fission lead to an estimate of 6 MeV for its height in actinides. Figure 2.1 shows the

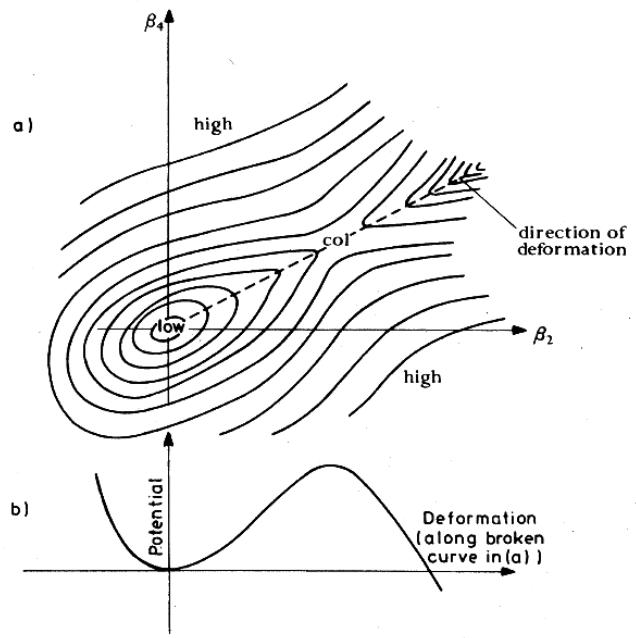

Figure 2.1: Deformation energy contours as a function of quadrupole and hexadecapole deformations (a) and the potential energy along the most favorable path to fission - indicated with the dashed line (b). The potential energy on the path to fission during deformation of the nucleus comprises the fission barrier (from [20]).

schematic depiction of a liquid drop model calculation as given in [20]. While

the spherical shape considered above is stable for a fissility parameter $x < 1$, a nucleus undergoing fission experiences very large distortions, leading to strong deformations. Thus, higher order terms need to be included in equation (2.2) to describe the deformation correctly. The potential energy in figure 2.1 is plotted as a function of the two most important moments of deformation, the quadrupole moment β_2 and the hexadecapole moment β_4. The energetically most favorable path to fission is indicated with a dashed line. The Bethe-Weizsäcker formula predicts spherical ground states of all nuclei and does not include shell structure; consequently it cannot explain several peculiarities of the fission process, like the angular distributions of fission fragments.

2.1.3 Shell Corrections

The nuclear shell potential as introduced originally by Goeppert-Mayer [21] consists of a central spherical potential and a spin-orbit interaction, which describes the mean field interaction of nucleons in a nucleus. The nucleons are assumed to move independently in the mean field created by the other nucleons and the Schrödinger equation yields single-particle energy levels ϵ and wave functions for the nucleons. Nilsson extended the model to deformed nuclei by introducing a deformed potential in which the nucleons move [22, 23]. The total energy of the even-even nucleus in the independent particle model is given by the sum

$$U = \sum_{\nu} 2n_{\nu}\epsilon_{\nu}, \tag{2.7}$$

where $2n_{\nu}$ is the number of particles occupying the energy levels ϵ. In general, the simple shell model gives less accurate results than the semi-empirical liquid drop due to the strong simplification of a mean field.

Strutinsky [24] used the single particle model for his shell correction method (SCM) of fission, but he replaced the single particle energies by a uniform dis-

tribution of states $\widetilde{g}(\epsilon)$. The total energy of a nucleus in the SCM is given by

$$E = E_{LDM} + U - \widetilde{U} = E_{LDM} + \delta U, \tag{2.8}$$

where E_{LDM} is the energy obtained from the liquid drop model, U is the previously introduced single particle energy sum and $\widetilde{U}$ is supposed to be the shell model analogue of the liquid drop energy. $\widetilde{U}$ is

$$\widetilde{U} = 2\int_{-\infty}^{\widetilde{\lambda}} \epsilon\widetilde{g}(\epsilon)d\epsilon, \tag{2.9}$$

where $\widetilde{\lambda}$ is the chemical potential defined by

$$N = 2\int_{-\infty}^{\widetilde{\lambda}} \widetilde{g}(\epsilon)d\epsilon \tag{2.10}$$

with N being the total number of particles. The difference $\widetilde{U} - E_{LDM}$ renormalizes the single-particle energy sum U. The SCM thus combines the correct average energy from the liquid drop model with the effects from the single-particle potential and is therefore often called the macroscopic-microscopic model. The systematic uncertainties from shell corrections disappear due to $U - \widetilde{U} = \delta U$, while fluctuations in the total energy due to local shell structure are accounted for. In addition to the shell corrections, a pairing factor δP has to be introduced, which corrects for different pairing energies of the true and averaged single-particle state densities. Equation (2.8) now reads

$$E = E_{LDM} + \delta U + \delta P. \tag{2.11}$$

The shell correction δU is positive (negative) for high (low) level densities as a function of deformation and nucleon number. When the nucleon number corresponds to a gap in the single-particle energy sequence, the nucleons are bound more strongly, which corresponds to the phenomenon of 'magic numbers'; these gaps are not only found in spherical but also in deformed shapes, but not necessarily for the same number of orbitals.

2.1.4 The Double-Humped Barrier

The shape of the fission barrier according to the SCM for the actinide region is double-humped; the first minimum is located at a deformation ϵ, which explains non-spherical ground states. Figure 2.2 shows a schematic drawing of the fission barrier with respect to the deformation of the nucleus. The barrier shapes for both the liquid drop model and the refined SCM model that includes shell effects are shown. The double-humped barrier (labeled A and B) corresponds to the lowest possible total energy of the nucleus with respect to its deformation which in turn corresponds to the occupation of certain Nilsson orbitals. The states in the minima of the barrier are classified class I and class II states depending on which minimum they are confined to. Class I states are confined to the first minimum and correspond to excitations of the nucleus in its ground-state deformation. Class II states are confined to the second minimum and correspond to excitations in a more deformed configuration. Class II states exhibit larger fission widths than class I states mainly because of tunneling through the outer barrier. Coupling of the two classes of discrete states explain resonances in fission cross sections. The nucleus progresses from the initially excited state to the highly deformed transition state along the path to fission. Once the nucleus passes the maximum of the outer barrier or saddle point fission is inevitable. On top of the two maxima single-particle excitations are schematically drawn in figure 2.2.

2.1.5 Statistical Model of Nuclear Reactions

In nuclear reaction theory one can distinguish between different types of reactions involving a target nucleus and a projectile based on the timescale they occur on. Direct reactions take place in the time it takes a projectile to travel

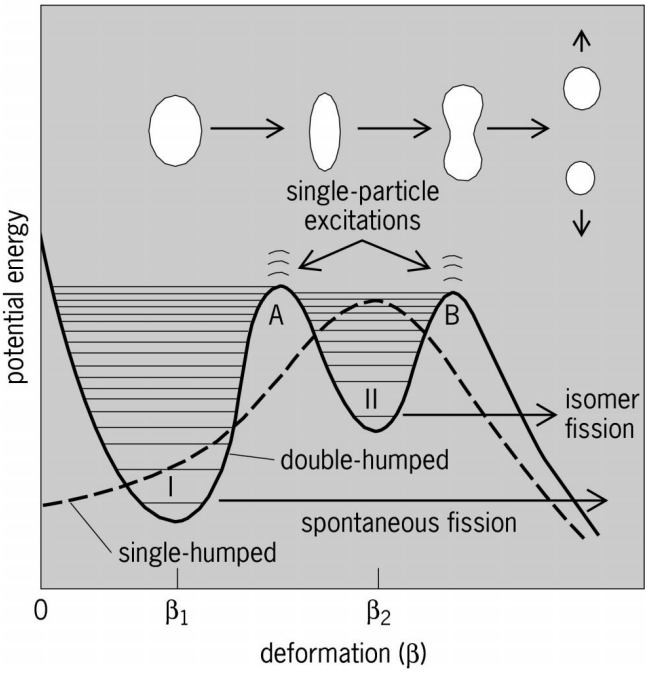

Figure 2.2: Shell corrections lead to a double-humped fission barrier with a second minimum right at the barrier maximum of the liquid drop model (from [25] after [26]).

through a target, while so-called compound nuclear reactions produce an equilibrium state in the target nucleus which fully absorbs the projectile that takes many orders of magnitude longer. Reactions that occur on an intermediate timescale, before full equilibrium is achieved, are called pre-equilibrium reactions. Compound nuclear reactions are well described by the statistical model, which splits the reaction process into two steps: First, the formation of the compound nucleus and second, the decay in the exit channel. In addition, Bohr's independence hypothesis [27] applies, which states that there is no correlation between the decay or fission of a nucleus and its formation. Hence, despite the conservation of total quantum numbers, the compound nucleus 'forgets' the way it was formed on its way to equilibrium. The statistical model furthermore assumes that the compound nucleus possesses high enough excitation energy that many states can be excited. The Hauser-Feshbach formalism [28] of the statistical model provides the framework for calculations of cross sections based on the independence hypothesis.

In the statistical model incoming and outgoing channels are characterized by energy, momentum, angular momentum and parity. Conservation laws are obeyed in the formation of the compound nucleus and the outgoing channels: Total angular momentum, energy, momentum, and parity of the system are conserved. For a compound reaction

$$a + A \rightarrow (CN^*) \rightarrow b + B \tag{2.12}$$

the incoming projectile a and the target nucleus A merge to form an excited compound nucleus CN^*. After equilibration the decay into the ejectile b and the residual nucleus B is considered. In the case of angular momentum the target spin $\vec{I}_A$ couples with the projectile spin $\vec{s}_a$ to form the channel spin $\vec{S}$, which then couples with the orbital angular momentum $\vec{\ell}_a$ to form the compound nucleus total angular momentum $\vec{J}_{CN}$. The compound nucleus angular momentum $\vec{J}_{CN}$

has to be the same as the coupled total angular momentum of residual nucleus spin $\vec{I}_B$ plus spin $\vec{s}_b$ and orbital angular momentum $\vec{\ell}_b$ of the ejectile. The conservation laws for energy E, momentum p and parity π can be written in the same fashion, see for example [29]:

$$\vec{I}_A + \vec{s}_a + \vec{\ell}_a = \vec{J}_{CN} = \vec{I}_B + \vec{s}_b + \vec{\ell}_b \tag{2.13}$$

$$E_a + E_A = E_{CN} = E_B + E_b \tag{2.14}$$

$$\vec{p}_a + \vec{p}_A = \vec{p}_{CN} = \vec{p}_B + \vec{p}_b \tag{2.15}$$

$$(-1)^{\ell_a}\pi_a\pi_A = \pi_{CN} = (-1)^{\ell_b}\pi_b\pi_B \tag{2.16}$$

2.2 Fission Fragment Angular Distributions

Vandenbosch [30] gives an overview of the theory required to describe angular distributions in fission which the following section is heavily based on. Fission fragment angular distributions can provide information on the state of the nucleus at the saddle point on top of the second maximum of the fission barrier. This includes information on the shape of the fission barrier and the density of excited states on top of the second maximum or saddle point, where the nucleus is highly deformed.

2.2.1 The Transition State Model

Bohr [8] first suggested that for excitation energies near the barrier the nucleus is thermodynamically cold as most energy is stored in deformation energy. He introduced the name transition nucleus for the deformed nucleus at the top of the barrier, which exhibits a discrete spectrum of excitations similar to the one found at the ground state deformation. Bohr's concept of near-barrier fission through discrete low-lying transition states provides the framework in which the

angular distributions depend on the quantum numbers of the discrete transition states involved. The transition state model immediately provided a qualitative understanding of anisotropic emission of fission fragments for photofission and other low energy fission reactions [31].

The deformed nucleus is assumed to behave like a rigid body with two equal moments of inertia and one that differs, it is a symmetric spinning top. The transition state can be described by the quantum numbers J, K and M associated with wave functions of a rigid rotor. As schematically depicted in figure 2.3, $\vec{J}$ is the total angular momentum of the rotating nucleus, $\vec{M}$ is the projection of $\vec{J}$ on the space-fixed axis (usually the incident beam direction), vector $\vec{K}$ is the projection of $\vec{J}$ on the symmetry axis of the top and $\vec{R}$ is the projection of $\vec{J}$ on any axis perpendicular to $\vec{K}$. The quantum mechanics for the spinning

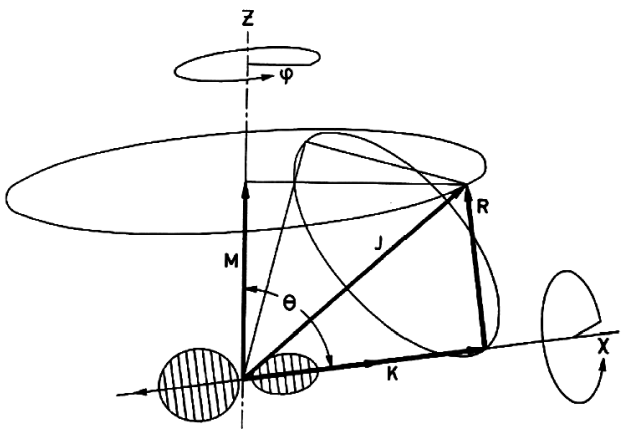

Figure 2.3: The highly deformed transition state nucleus behaves like a rigid symmetric spinning top and its quantum numbers J, K, and M define the angular distribution of fission fragments (from [32]).

top were solved long before the discovery of fission [33, 34]. The angular part

of the corresponding Schrödinger equation reads

$$\frac{\hbar^2}{2J_\perp}\left[\frac{1}{\sin(\theta)}\frac{\partial}{\partial\theta}\left(\sin(\theta)\frac{\partial\Psi}{\partial\theta}\right)+\frac{\left(\cos(\theta)\frac{\partial}{\partial\chi}-\frac{\partial}{\partial\varphi}\right)^2\Psi}{\sin^2(\theta)}\right]+\frac{\hbar^2}{2J_\parallel}\frac{\partial^2\Psi}{\partial\chi^2}+E\Psi=0, \tag{2.17}$$

where θ is the angle between the nuclear symmetry axis and the space-fixed axis, φ is the azimuthal angle around the space-fixed axis, χ is the angle around the symmetry axis, and $J_\parallel$ and $J_\perp$ are the moments of inertia parallel and perpendicular to the symmetry axis, respectively. The solution to equation (2.17) can be cast in the form

$$\Psi=\sqrt{\frac{2J+1}{8\pi^2}}e^{iM\chi}e^{iM\varphi}\,\mathrm{d}^J_{M,K}(\theta), \tag{2.18}$$

where the $\mathrm{d}^J_{M,K}(\theta)$ function is the rotation matrix as given by Wigner [35],

$$\begin{aligned}\mathrm{d}^J_{M,K}(\theta)&=\sqrt{(J+n)!(J-n)!(J+K)!(J-K)!}\\ \times\sum_n&\frac{(-1)^n\left[\sin\left(\frac{\theta}{2}\right)\right]^{K-M+2n}\left[\cos\left(\frac{\theta}{2}\right)\right]^{2J-K+M-2n}}{(J-K-n)!)(J+M-n)!(K-M+n)!n!}.\end{aligned} \tag{2.19}$$

The corresponding energy levels of the spinning top are then given by

$$E=\frac{\hbar^2\left[J(J+1)-K^2\right]}{2J_\perp}+\frac{\hbar^2K^2}{2J_\parallel}. \tag{2.20}$$

The theory of fragment angular distributions is based on the conservation of total angular momentum. Within the framework of the symmetric spinning top, the total angular momentum J and its projection M along a space-fixed axis are conserved through the entire fission process. The angular distributions can then be deduced from the quantum numbers of the transition states with two important assumptions: First, the fission process proceeds along the symmetry axis of the transition nucleus to scission and the fission fragments are subsequently emitted along said axis. And second, once the nucleus arrives at the

saddle point or second maximum, the projection of J onto the nuclear symmetry axis K is a good quantum number and remains conserved through the scission point. Note that K can, however, change due to vibrations and shape changes up until the nucleus evolves to the saddle point. The angular distribution of fission fragments therefore depends on J, M, and the K value at the saddle point of the fission barrier. The probability of a fission fragment being emitted at an angle θ from a transition state J, M, K is then given by [36]

$$P^J_{M,K}(\theta) = \left[\frac{(2J+1)}{4\pi R^2}\right] \mid \mathrm{d}^J_{M,K}(\theta)|^2 \, 2\pi R^2 \, \sin(\theta) \, d\theta. \tag{2.21}$$

Note that the probability does not depend on the azimuthal angle around the space-fixed axis φ, the angle around the symmetry axis χ or the moments of inertia. The distribution only depends on the angle θ between the space-fixed axis and the symmetry axis. Dividing equation (2.21) by $\sin(\theta)d\theta$ leads to the angular distribution

$$W^J_{M,K}(\theta) = \left[\frac{(2J+1)}{2}\right] \mid \mathrm{d}^J_{M,K}(\theta)|^2. \tag{2.22}$$

Angular distributions for low excitation energies above the barrier, where the discrete transition state model applies, are obtained directly from equation (2.22). For higher excitation energies an extension of the theory to a statistical regime is necessary.

2.2.2 The Standard Saddle-Point Statistical Model

Halpern and Strutinsky introduced a statistical treatment that generalizes the energy dependence of fragment angular distributions to moderate and high excitation energies above the fission barrier. This standard saddle-point statistical model (SSPM) [37] describes the K distribution of states at the saddle point with a Gaussian distribution related to the thermodynamic temperature of the

excited nucleus. The angular distribution generally depends on the angular momentum brought in by a projectile and the fraction of that momentum that is converted into orbital angular momentum between the fragments, which is characterized by the quantum number K. The level density in the transition nucleus is given by

$$\rho(J,K) \propto e^{\left(E-E_{rot}^{J,K}\right)/k_BT}, \tag{2.23}$$

where $E_{rot}^{J,K}$ are the energies defined in equation (2.20) and T is the thermodynamical temperature of the nucleus. With equation (2.20) the level density becomes

$$\rho(J,K) \propto e^{(E/k_BT)-\left(\hbar^2J^2/2J_\perp k_BT\right)-\left(\hbar^2K^2/2k_BT\right)\left[\left(1/J_\parallel\right)-(1/J_\perp)\right]}. \tag{2.24}$$

If E, T and J are fixed, the distribution in K becomes

$$\rho(K) \propto e^{-\left(\hbar^2K^2/2k_BT\right)\left[\left(1/J_\parallel\right)-(1/J_\perp)\right]} \tag{2.25}$$

which is equivalent to a Gaussian K distribution

$$\rho(K) \begin{cases} \propto e^{-\left(K^2/2K_0^2\right)} & K \leq J \\ = 0 & K > J, \end{cases} \tag{2.26}$$

where

$$K_0^2 = \frac{k_BTJ_{eff}c^2}{\hbar^2c^2} \tag{2.27}$$

and $\left(1/J_\parallel\right)-(1/J_\perp) = 1/J_{eff}$. The resulting expression for the fragment angular distributions in the SSPM is given by

$$W(\theta) \propto \sum_{J=0}^{\infty}\sum_{M=-(I_A+s_a)}^{I_A+s_a}\left[\sum_{\ell=0}^{\infty}\sum_{S=|I_A-s_a|}^{I_A+s_a}\sum_{\mu=-I_A}^{I_A}\frac{(2l+1)T_\ell|C_{M,0,M}^{S,\ell,J}|^2|C_{\mu,M-\mu,M}^{I_A,s_a,S}|^2}{\sum_{\ell=0}^{\infty}(2l+1)T_\ell}\right] \times \sum_{K=-J}^{J}\frac{(2J+1)|\,\mathrm{d}_{M,K}^J(\theta)|^2e^{-K^2/2K_0^2}}{\sum_{k=-J}^{J}e^{-K^2/2K_0^2}}, \tag{2.28}$$

where $\vec{I}_A$, $\vec{s}_a$ and $\vec{S} = \vec{I}_A + \vec{s}_a$ are the target spin, projectile spin and channel spin, respectively. The total angular momentum is the channel spin plus the orbital angular momentum $\vec{J} = \vec{S}+\vec{\ell}$, the projection of $\vec{I}_A$ on the space-fixed axis is μ and the projection of $\vec{S}$ and $\vec{J}$ on the space-fixed axis is M. The $\mathrm{d}^J_{M,K}(\theta)$ functions are defined in equation (2.19), and $C^{S,\ell,J}_{M,0,M}$ and $C^{I_A,s_a,S}_{\mu,M-\mu,M}$ are Clebsch-Gordan coefficients. The angular distribution (2.28) also contains information on the compound nucleus formation via the transmission coefficients T_ℓ, which are defined as

$$T_\ell = 1 - |S_\ell|^2 \,, \tag{2.29}$$

where S_ℓ is the scattering matrix element for elastic neutron-nucleus scattering in the entrance channel. The transmission coefficient is best obtained from optical model calculations. The latter is a simple yet efficient method for the description of elastic scattering using an energy-dependent and complex single-particle potential [38].

2.2.3 Neutron-Induced Fission of ^{235}U

In the case of neutron-induced fission of ^{235}U the target spin I_0^π is $7/2^-$ and the channel spin is $S = 3$ or $S = 4$. J is more de-oriented than in the case of even-even nuclei where the target spin is zero, and the angular distribution is flatter. At higher incident energies the angular distribution is expected to be forward-backward peaked when K is much smaller than J. At the onset of multi-chance fission (the emission of a neutron before fission) the excitation energy decreases which mainly affects K_0 which in turn increases the forward-backward peaking.

2.2.4 Fission Fragment Anisotropy

The anisotropy parameter A is defined as the ratio of fragment emission probabilities in beam direction $W[0°]$ and perpendicular to the beam $W[90°]$

$$A = \frac{W[0°]}{W[90°]} = \frac{W[\cos(\theta) = 1]}{W[\cos(\theta) = 0]}, \tag{2.30}$$

where $W[\cos(\theta)]$ denotes the angular distribution of fission fragments. If the distribution W is normalized to 1 perpendicular to the beam at 90°, the anisotropy A is just the emission probability in beam direction:

$$A = \frac{W[\cos(\theta) = 1]}{W[\cos(\theta) = 0] = 1} = W[\cos(\theta) = 1]. \tag{2.31}$$

Although the anisotropy parameter itself does not provide complete information on the shape of the angular distribution, it is a good indicator especially in the case of neutron-induced fission of ^{235}U where anisotropic emission happens mainly in the forward-backward direction. The anisotropy parameter also allows easy comparison of data sets and isotopes over a range of incident energies.

Chapter 3

Previous Work

This chapter gives a brief overview of previous anisotropy measurements and describes some of the techniques commonly used in those studies. The first observation of anisotropy in fission fragment angular distributions was made by Winhold in 1952 [9]. Winhold saw that fission fragments from ^{232}Th photofission were preferentially emitted perpendicular to the beam direction - Henkel and Brolley [39] observed similar results for neutron-induced fission of ^{232}Th and ^{238}U. Generally, the anisotropy effect is more pronounced in even-even targets because of a lower level density at the fission barrier due to pairing (see chapter 2.2). The anisotropy parameter values in these cases are large and the measurement requires less resolution, which explains why more data is available for these isotopes, see for example [40, 41, 42, 43].

Simmons and Henkel [44] led a large measurement campaign at Los Alamos National Laboratory in the 1960s that provided data for a series of isotopes, including ^{235}U over neutron energies from 0.5 MeV to 9 MeV and from 14.8 to 23 MeV. Figure 3.1 shows an overview of all measurements of ^{235}U(n,f) found in the EXFOR library. Simmons' data set is the most comprehensive to date for neutron-induced fission of ^{235}U. Meadows [45, 46] also provides an extensive

measurement, which agrees well with the Simmons data. Both sets seem self-consistent and follow a general trend with a steady rise in anisotropy at low neutron energies, an eventual plateau from 2 to 6 MeV and a steep incline at the threshold for second chance fission. The experimental methods used in

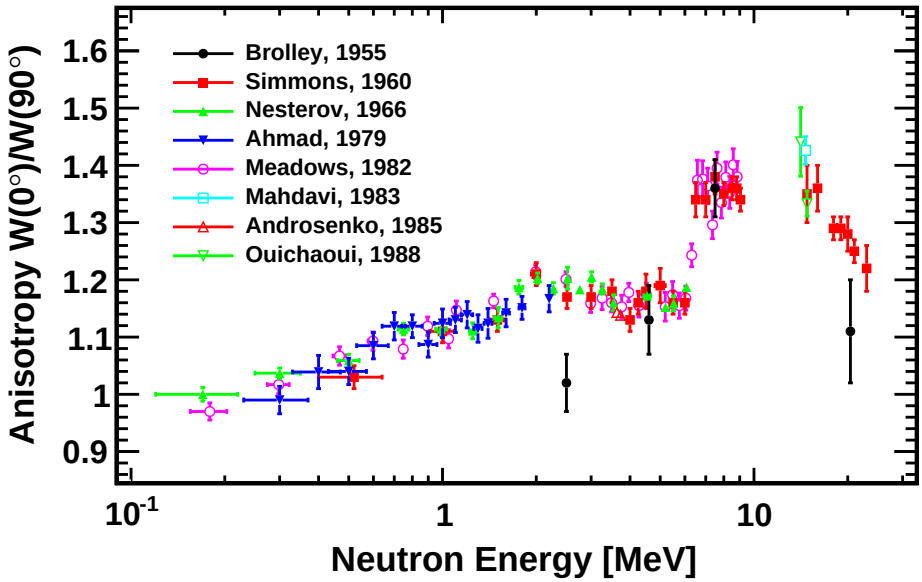

Figure 3.1: An overview of fission fragment anisotropy data for neutron-induced fission of ^{235}U available in the EXFOR [1] database.

the available data are very similar. Most measurements were carried out with ionization chambers (see chapter 4.1 for an introduction). Simmons used an ionization chamber with five proportional counters covering polar angles from 0 to 90 degrees. Meadows used a double Frisch-gridded chamber, covering the complete solid angle. One common characteristic of the measurements displayed in figure 3.1 is the use of mono-energetic neutron sources, where measurements over a wide range of neutron energies are more difficult than in a white neutron spectrum like the one available at LANSCE. Presently, there are a few new

efforts underway to measure angular distributions at continuous neutron sources up to high energies. CERN's n_TOF collaboration is using a PPAC (parallel plate avalanche counter) assembly to measure fission cross sections and angular distributions at a range of neutron energies up to several hundred MeV. Tarrio published results on the anisotropy of ^{232}Th fission [43, 47], while ^{235}U(n,f) data can be found in a thesis by Leong [48]. The preliminary ^{235}U(n,f) data exhibits large statistical error bars, but a publication of final results is anticipated in the next few months. Vorobyev [49] recently measured the anisotropy of fission fragments for multiple isotopes including ^{235}U(n,f) up to neutron energies of 200 MeV at the GNEIS facility [50]. Both Vorobyev's and Leong's data sets add much needed data points at higher neutron energies, but exhibit large error bars. They do, however, show a trend of the anisotropy declining steadily from its maximum value at 14 MeV to about 1 and even below at incident energies beyond 100 MeV.

Chapter 4

Experiment

In this chapter an introduction to the field of time projection chambers is given together with a description of the fissionTPC experiment. The detector itself and the neutron source, the linear accelerator at LANSCE, are presented in sections 4.2 and 4.3, respectively. Section 4.2.2 introduces the basic principles of particle tracking and the associated software elements allowing the analysis of angular distributions.

4.1 Gaseous Ionization Chambers

Ionization chambers are radiation detectors in which an electrical signal is generated by passing particles ionizing a fill gas [51]. The term encompasses ion chambers, where electron-ion pairs are detected, proportional counters, where a signal is amplified but proportional to the ionization (like in a TPC), and Geiger tubes, where the signal is amplified to the point where it is not proportional to the original charge created. The ionization chamber consists of a gas filled chamber with two electrodes. Its operating principle relies on the generation of ion-electron pairs in the fill gas by the interaction with ionizing particles

passing through the detector. The energy needed to create an ion-electron pair ranges from 25 to 35 eV in different gases, slightly higher than the ionization energy of the gas. Thus the energy loss of the ionizing particle in the gas is proportional to the number of ion-electron pairs created. An electric field in the ionization chamber accelerates the free electrons towards an anode and the ions towards a cathode although at a much longer time scale. The moving charge generates an electrical signal in the detector, which primarily stems from the moving electrons while the slow moving ions barely contribute.

A predecessor of the fissionTPC - the Frisch-gridded ionization chamber - has been used extensively in the past to study nuclear fission [52, 53, 54, 55]. Like in a TPC, the fission products leaving the target deposit most of their kinetic energy through ionization of the gas in the ionization chamber. The created electrons drift towards the anode plane because of an applied electric field while the much slower ions drift towards the cathode, the anode is shielded from induced charge by a Frisch-grid. The measured anode signal is proportional to the number of ion-electron pairs created and therefore to the particle energy. The use of the Frisch-grid signal gives some tracking information as the shape of the signal contains angle information of the track.

4.1.1 The Time Projection Chamber Technique

The TPC is an instrument that has frequently and successfully been used in high energy physics over the last 25 years (see [56, 57, 58]). A TPC provides a complete three-dimensional digital picture of the ionization in a gas volume. It allows for the complete reconstruction of ionizing particle trajectories and their specific ionization along the entire track as they range out in the fill gas. TPC technology has been used in the past for precision and high data rate experiments - a famous example being the STAR detector at Brookhaven [59], which studies

heavy ion collisions. Figure 4.1 is a rendering of the STAR TPC, including a high number of tracks with the one helium particle of interest highlighted. Recent improvements in data acquisition electronics and computation enabled the miniaturization of TPCs and their use for high resolution and zero-dead-time applications, like nuclear fission.

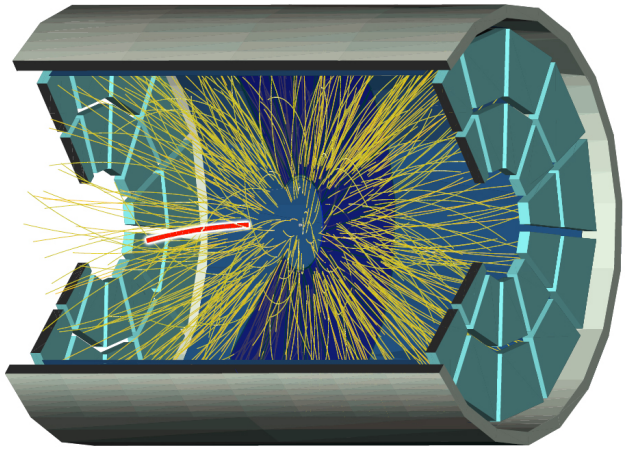

Figure 4.1: An overlay of simulated particle trajectories in the high data rate STAR TPC (from [60]).

The TPC detector is in some aspects similar to conventional fission ionization chambers: it consists of a pressurized chamber with a central cathode and two parallel anode detector planes on each end of the chamber. Each anode pad plane has a number of channels arranged on the pad for radial resolution. Ionizing particles emitted from an event ionize the fill gas. An applied electric field between the target and the readout anode pad planes accelerates the ionization electrons towards the pad planes and minimizes their recombination with positive ions. The measured electron drift time (when the drift speed in the gas is known) is used to calculate the z-coordinate of the ionization, while the highly segmented anode plane provides the radial angle information for reconstructing the particle trajectories (see figure 4.2). The ionization electrons are multiplied

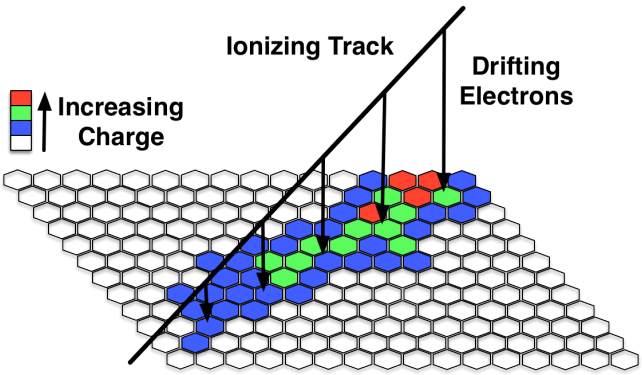

Figure 4.2: The radial information for the track reconstruction is provided through a highly segmented anode plane that collects ionization electrons created along charged particle trajectories.

and accelerated towards the anode using an amplification system. Wire amplification has been the most common method used in particle physics to produce this so-called gas gain in the past. Recent developments have focused on better spacial resolution and less ion feedback into the TPC by the electron avalanche; the micromesh gaseous (MICROMEGAS) technology employs a fine conductive electroformed mesh suspended over the pad plane [61, 62]. Figure 4.3 shows the schematics for the MICROMEGAS avalanche system. The electrons are amplified by the high field between the micromesh and the pad plane.

4.2 The fissionTPC

The NIFFTE collaboration has designed and built a custom TPC specifically to measure characteristics of fission events. A detailed description of design specifications and all sub-systems of the detector and first performance results were published recently [63]; the following section follows the outline of that publication. Figure 4.4 shows a photograph of the fissionTPC fully assembled on its designated flightpath at LANSCE during the 2014/2015 run cycle.

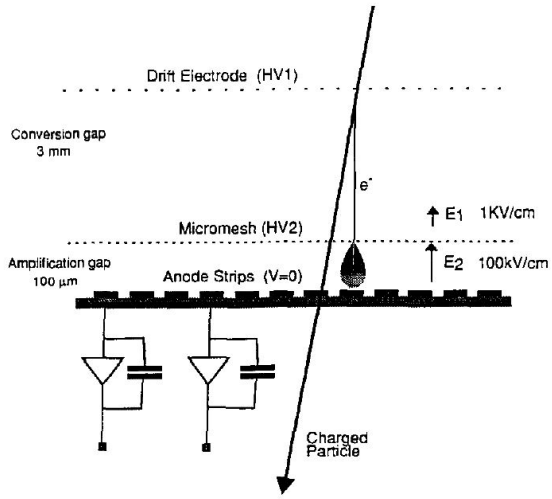

Figure 4.3: A schematic view of MICROMEGAS with the amplification gap between the micromesh and the anode (from [62]).

4.2.1 Hardware

The major hardware components of the experiment include the centerpiece - the pressure vessel with the electric field cage and precise gas handling, the pad planes and the gas amplification; a complex data acquisition system, and the radioactive targets. Figure 4.5 shows an exploded view of the fissionTPC components.

The Pressure Vessel and the Fill Gas

The fissionTPC contains a pressurized cylindrical chamber of about 11 cm length with a 7.5 cm radius. The vessel houses a central cathode and two parallel anode detector planes on each end of the cylinder. An axial opening in the cathode makes room for the radioactive target. The vessel is made of aluminum and designed to hold a pressure of up to 20 bar. The normal operating pressure is chosen to stop all charged particles of interest within the active volume dependent on the fill gas. Figure 4.6 shows a schematic view into the inner workings of

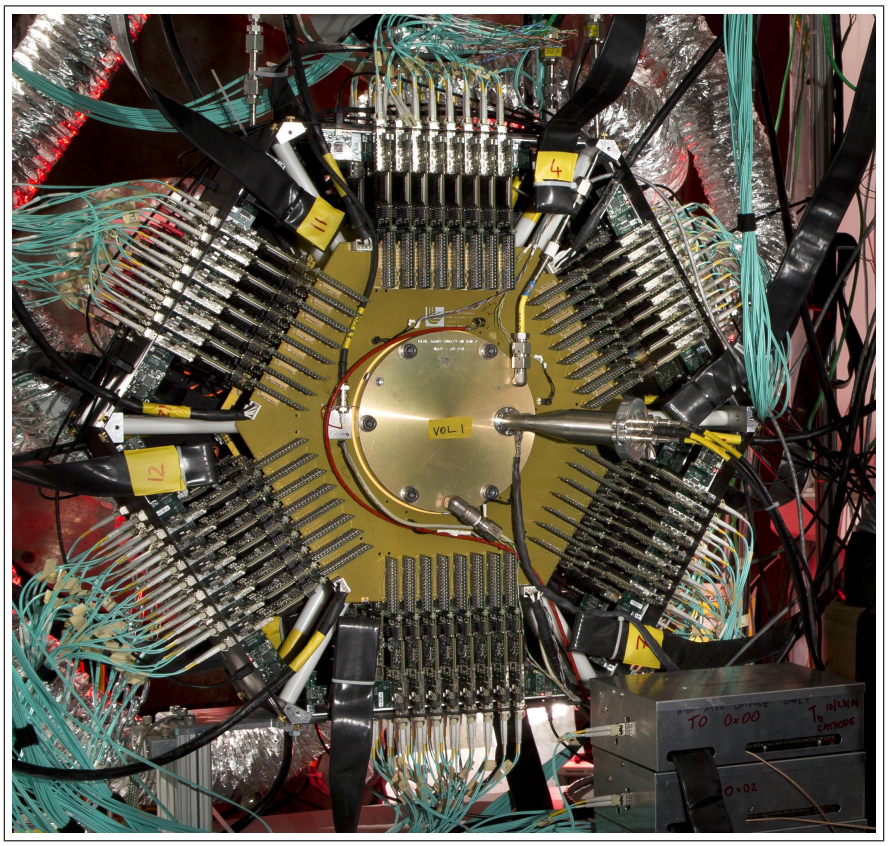

Figure 4.4: A photograph of the fully assembled fissionTPC on the designated flightpath at LANSCE during the 2014/2015 run cycle. The front face is missing in the picture to showcase the electronics.

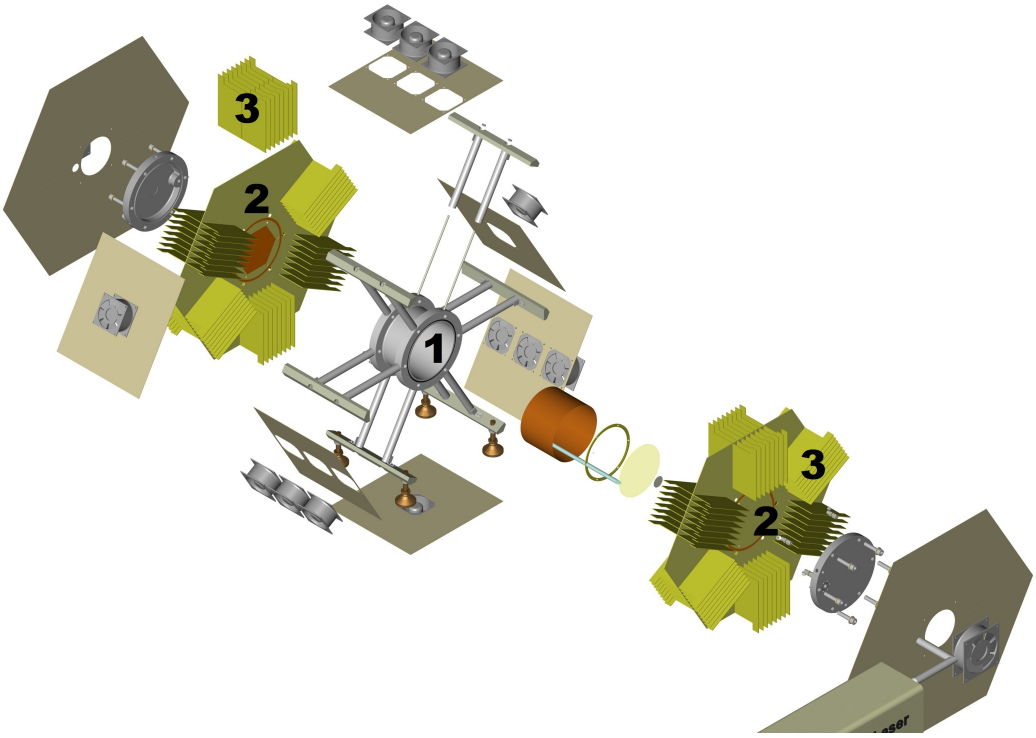

Figure 4.5: An exploded view of the fissionTPC components with the pressure vessel (1), anode planes (2) and the preamplification and EtherDAQ cards (3) of the data acquisition system mounted on the sides.

the assembled fissionTPC - the vessel - with tracks coming off the target plane. Ionizing particles and fission products leave the target plane and ionize the fill gas, which is operated at atmospheric pressure of approximately 550 Torr. For the current configuration with 95 % Argon and 5 % Isobutane (C_4H_{10}) alpha particles and fission products are easily stopped within the chamber volume at atmospheric pressure. The gas density has to be kept constant within 0.1 % and the gas purity has to be assured in order to achieve the anticipated precision measurement of fission parameters and cross sections. The current gas system design allows a mixture of up to three gases. The mass flow rates are controlled by an automated mass flow control system and High-Efficiency Particulate Air (HEPA) filters are used to keep the gas clean of contaminants.

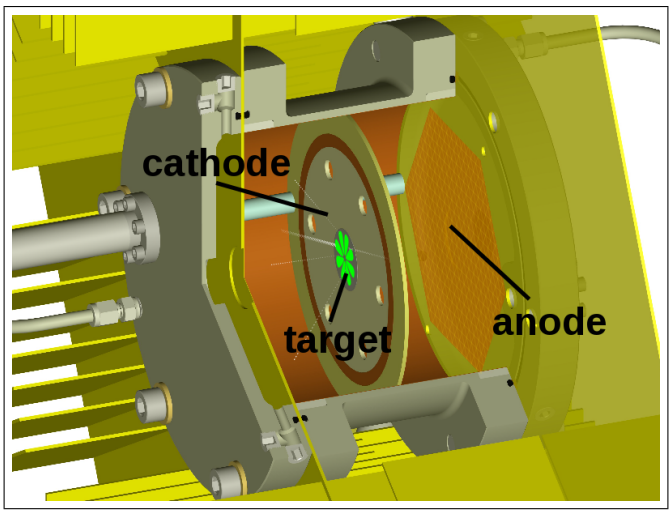

Figure 4.6: A schematic drawing of the fissionTPC with particle tracks coming off the target in the center of the cathode plane and the hexagonal structure of the pads on the micromesh anode.

The Electric Field

An applied electric field accelerates the ionization electrons towards the anode plane in each respective half of the fissionTPC. It is the purpose of the field cage to provide a uniform electric field throughout the entire volume of the fissionTPC, which is crucial for its proper operation. The field cage is comprised of rings of copper wire inside the vessel, with step-down resistors that reduce the voltage along the length of the vessel. The cage requires high voltage, which is delivered through the high voltage feed-through - a sealed, small opening in the fissionTPC aluminum bulkhead that holds three 30 kV cables and withstands 5 bar operation pressure. The cathode and target are nominally kept at -3000 V, while the MICROMEGAS is kept at -200 V to -300 V and the anode pad is grounded. Figure 4.7 shows the biasing of the fissionTPC electric field with example voltages. During the 2014/2015 run cycle, the cathode was kept at -3000 V, while the MICROMEGAS was kept at -200 V. In the 5.4 cm drift distance in one half of the fissionTPC the electric field was then 520 V/cm, while the field in the avalanche area between the MICROMEGAS and the anode was approximately 2.7×10^4 V/cm over the 75 μm amplification gap.

The Pad Planes and Gas Amplification

Each anode plane consists of 2976 hexagonal detector channels - gold coated copper pads - arranged into sextants on a printed circuit board. The pad plane is the most crucial part of the fissionTPC and also holds the MICROMEGAS gas amplification mesh layer (see section 4.1.1). The only 3 μm thick and 1000 lines per inch dense electroform mesh is glued to the anode plane with pillars that hold the mesh at a distance of about 75 μm from the pad (see figure 4.8). Figure 4.9 shows a photograph of the current pad plane with the micromesh glued to it.

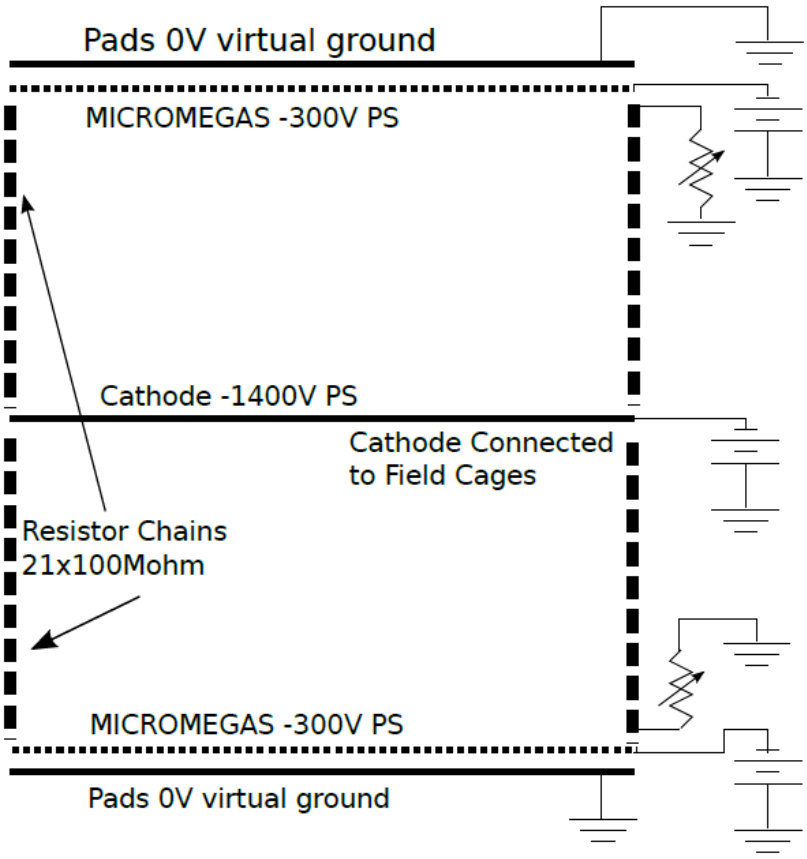

Figure 4.7: The biasing of the fissionTPC with example potentials. The field cage resistors are actually voltage controlled and the bottom of the field cage is biased to the MICROMEGAS potential.

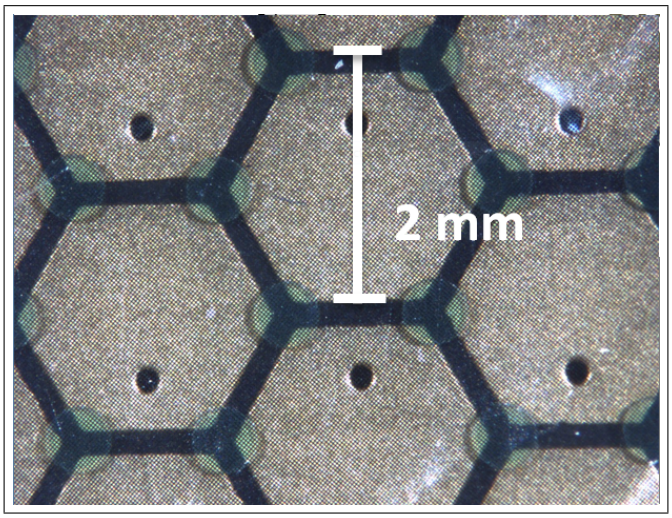

Figure 4.8: A close-up view of the pad plane surface. The gold coated hexagonal pads, their offset and the MICROMEGAS pillars are visible.

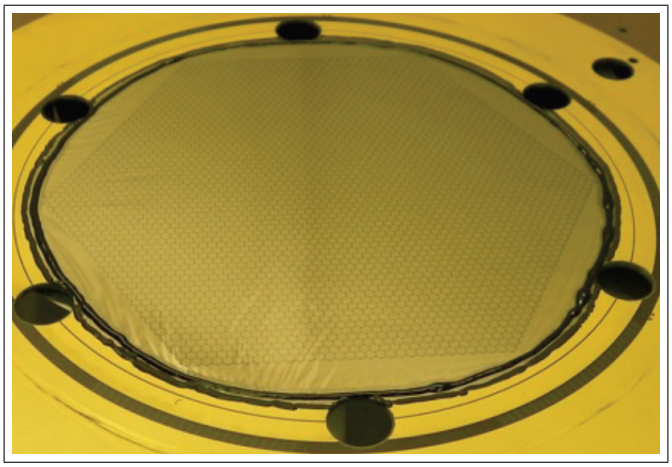

Figure 4.9: The latest version of the fissionTPC pad plane with the MICROMEGAS mesh installed.

The Data Acquisition System

The fully instrumented fissionTPC has almost 6000 hexagonal pads on the two anode planes, each of which is instrumented with a preamplifier, an analog-to-digital converter (ADC) and a digital readout. The electronic boards are custom made at Lawrence Livermore National Laboratory (LLNL); a more detailed description can be found in [64]. Each front-end electronics board contains electronics for 32 channels and outputs raw Ethernet data packages. Housed on the board are 32 preamplifiers, four ADC chips, one field programmable gate array (FPGA), memory and an Ethernet jack. An edge card connection brings in the pad signals, a small ribbon cable brings in power, clock and auxiliary signals, and the data is output on the Ethernet connection. The 200 cards in total are then wired to standard Ethernet switches to build a network that connects the cards to one computer that serves the role of data collection. The data acquisition is located on the experiment to minimize noise from long cables and to reduce a data rate of up to multiple TB/s in the chamber to 70 MB/s output from the EtherDAQ cards. The high-speed cathode readout (HiSCaR) subsystem digitizes the cathode signal with a timing precision of up to one nanosecond to preserve the timing and energy measurement of incoming neutrons. A slow control system measures pressures and a range of temperatures in and around the experiment, including individual card temperatures. It can also send out signals to turn on or off the low voltages that control the data acquisition system; this is helpful for online monitoring and control of the experiment.

The Actinide Target

The fissionTPC targets are manufactured by a team of specialists at Oregon State University [65, 66]. A well-prepared set of targets is very important for high quality measurements. The goal is to avoid uncertainties in the target

mass, non-uniformities, surface defects and contaminants, as well as to eliminate impure target materials. The methods used for target fabrication include molecular plating and vacuum volatilization. So far, thick aluminum backing targets and micrometer thin targets on a thin carbon backing have been used in test runs. The thin backing targets enable the measurement of both fission products in the two halves of the fissionTPC and minimize scattering in the target. The current data set was obtained with a thick (138 mg/cm^2 $\approx$ 0.5 mm) 2024 aluminum alloy backing 40 mm in diameter which had approximately 50 μg/cm^2 of ^{239}Pu deposited on one side and ^{235}U ($\approx$ 26 nm thick) on the back side over an active target diameter of 20 mm each.

4.2.2 Software

A very involved software package specific to the fissionTPC experiment has been designed over the first years of the project and is still continuously being expanded and improved. In addition to online control and monitoring systems of the experiment, an offline software package including data reconstruction has been developed. The online software is built on C++ code and includes a data receiver, that is a custom code to interface with the fissionTPC electronics and delivers the raw Ethernet data packages to the event builder. The event builder collects the data from all of the data receivers and packages it into events that are sent to the storage system. Additional features added by the event builder are time stamps, temperatures, pressures and voltages from the experiment, database summary statistics, and data corruption detection.

The offline software is mainly built on C++ code arranged in modules using XML configuration files. The package includes a complete simulation of the fission process in the target, the transport of particles through the fissionTPC, and the detector response. Big parts of simulation and analysis are based on

the GEANT4 [67] and ROOT [68] software packages. The following sections focus on data reconstruction - a part of the offline software. The concept of the reconstruction chain from raw data to three-dimensional particle tracks with ionization loss information is illustrated using tracking algorithms available in the fissionTPC software but also most common in high energy physics TPC applications.

From Signals to Tracks

The track reconstruction software transforms digitized electronic signals from the individual channels on the segmented detector anode plane into a reconstructed particle track with energy loss information. The two-dimensional (x,y) coordinates of the ionizing particle track in the detector volume come from the position of each pad receiving ionization electrons on the segmented anode plane; in a first hypothesis the charge is believed to occur in the center of the pad. The z-coordinate is based upon the arrival time of the signal and is correlated to the drift speed of the ionization electrons within the fissionTPC. Without an absolute time signal from the cathode, the z-coordinates of the signals are only known relative to the other signals in an event. The absolute z-position of tracks in the fissionTPC can be determined using a cathode signal or demanding a track start at the cathode plane. The height of the signal is correlated to the number of ionization electrons deposited on the pad plane and therefore to the energy of the ionizing particle that generated the track in the active volume of the fissionTPC. The reconstruction software relies on the individual signal shapes, the signals' channel locations on the pad plane, their time-stamp, and the shape and size of their rise. Figure 4.10 shows an example depicting signals arriving at different pads from an ionizing track. The challenge for a tracking package is to create three-dimensional coordinates with additional charge infor-

mation from ADC signals on the two-dimensional pad and their time-stamp. After assuming that the charge hit the center of the pad, the estimate has to be refined by making use of the information from neighboring pads, which might shift the track away from the center of a pad. The absence of a magnetic field greatly simplifies the track extraction because it implies only straight tracks.

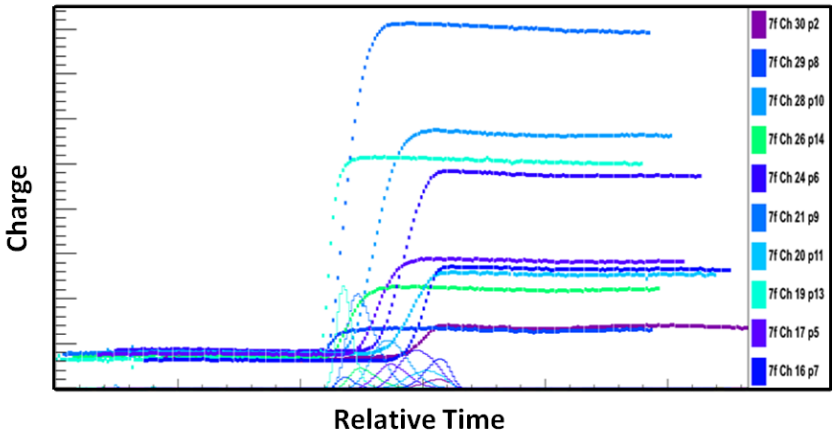

Figure 4.10: Individual signals from different channels for a track from a ^{252}Cf source in the fissionTPC.

The developed analysis software currently uses different track finding and fitting algorithms inspired by high energy physics applications, see [69] for a good review. Simple tracks are found using a conventional track finder based on charge thresholds that cannot separate multiple tracks in one event and a conventional fitter that minimizes the distance of charge to the track. If events are more complicated, like in the case of multiple tracks appearing in the volume at the same time, the NIFFTE software package offers more advanced track finding and suitable fitting routines. The most advanced are a track finder based on the Hough transform and a fitter using a Kalman filter. The methods used in these two tracking algorithms illustrate the challenges posed to any tracking package capable of the high precision data reconstruction for

this work and will be briefly discussed in the following sections. For the angular anisotropy analysis, only simple conventional track finder and fitter modules were used due to a normalization step in the angular analysis that removes the need for high-precision tracking.

The Hough Track Finder

The first step in this type of reconstruction chain is the production of digits from ADC signals. Digit objects contain information about the channel, time-stamp, rise time and size of the original signal. This knowledge is extracted from the original pulse shape either by fitting the signal or by taking the derivative of the signal. Using the signal distribution on the anode together with the time information of the pulse allows a constriction of the track in three dimensions. The information is used to visualize data objects distributed within the fissionTPC volume, which is partitioned into hexagonal prism voxels by the geometry of the pad plane. The next step in the reconstruction is identifying which digits in this collection of objects are part of a track estimate.

A commonly used technique, the Hough transform [70, 71, 72], calculates a track probability density by using all possible combinatorics of the available points in angle space. Line detection is based on the so-called point-line duality. A line through a point point $P(x, y)$ is defined as

$$y = kx + d. \tag{4.1}$$

The point P in x, y space now defines a line in parameter space k, d. Each point on the line in the slope and intercept space k, d then defines a line through point P in x, y space. The method can therefore be thought of as a transformation between the coordinate space x, y and the parameter space k, d. Since equation (4.1) has a singularity for the vertical line, Duda [71] introduced an alternative

parametrization

$$\rho = x\cos(\theta) + y\sin(\theta), \tag{4.2}$$

where ρ is the line's shortest distance from the origin and θ is the inclination of the normal. Image points $P(x, y)$ now define sine/ cosine curves in parameter space ρ, θ. The points with the highest occupancy in the parameter space define lines in x, y space that correspond to the most probable tracks through the list of input points, as can be seen in 4.11 for the simplified case of the slope and intercept space k, d. The Hough radius then determines the number of digits around the most probable track hypothesis that shall be included in the track. The line with the highest probability through all included digits is the seed for a track fit; the process then continues for all probabilities above threshold. One can summarize the Hough transform as a pattern recognition algorithm that filters out noise based on the selection of digits close to a track hypothesis rather than simple charge thresholds.

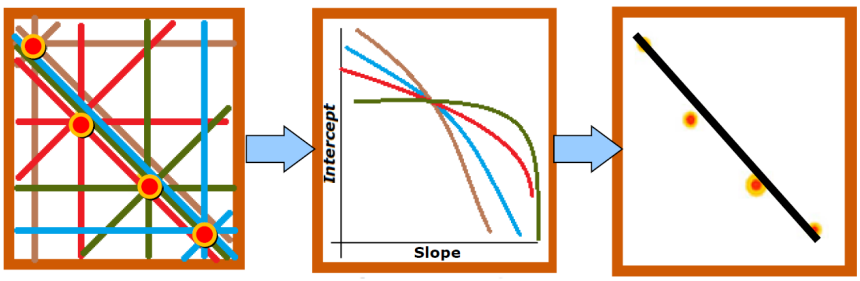

Figure 4.11: The Hough transform moves all combinatorics of a straight line hypothesis into a parameter space, where the highest occupancy bin corresponds to the most probable track.

The Kalman Filter

Once the Hough algorithm has identified all the points that are associated with a track, they are passed to a recursive track state estimator. The Kalman filter

connects the points and updates a smooth fit with associated error matrices for the most probable hypothesis [73, 74, 75]. The filter used in the NIFFTE tracking software assumes that the track trajectory is a straight line as there is no magnetic field and multiple scattering is assumed to be negligible. The Kalman filter determines the best fit for a set of points, adding one track point after another. In each step, the state vector is predicted using the currently available information, then the propagation and error matrices are calculated. With each step the uncertainties become more refined as information is added. At the end of the track, the filter is engaged once more to predict and filter the track in the opposite direction, which smoothes the track and provides the best estimates of track parameters.

The mathematical concept of the filter is outlined briefly here, for a detailed derivation see [74] or [75]. The problem addressed by Kalman filters is the estimate of a state x of a process

$$x_k = Ax_{k-1} + Bu_{k-1} + w_{k-1} \tag{4.3}$$

with a measurement

$$z_k = Hx_k + v_k. \tag{4.4}$$

The random variables w_k and v_k are the process (physics) and measurement noise, respectively, and are assumed to be independent of each other, white and with probability distributions

$$p(w) \sim N(0, Q), \tag{4.5}$$

and

$$p(v) \sim N(0, Q), \tag{4.6}$$

where Q and R are the process noise and measurement noise covariance respectively. The matrix A in equation (4.3) correlates the state at time $k-1$ to the

state at the current time k in the absence of both a driving function through the matrix B and process noise w. The process noise, in the physics case multiple scattering, is assumed to be negligible in the current realization of the fitter within the NIFFTE framework. The matrix H in equation (4.4) correlates the state and the measurement z_k. Now $\hat{x}_k^-$ is defined as the a priori state estimate at step k and $\hat{x}_k$ is the a posteriori state estimate at step k taking into account measurement z_k. The associated estimate errors are

$$e_k^- = x_k - \hat{x}_k^- \tag{4.7}$$

and

$$e_k = x_k - \hat{x}_k. \tag{4.8}$$

The corresponding error covariances are

$$P_k^- = E[e_k^- e_k^{-T}] \tag{4.9}$$

and

$$P_k = E[e_k e_k^T]. \tag{4.10}$$

The a posteriori state estimator $\hat{x}_k$ is computed with the a priori estimate $\hat{x}_k^-$ and a weighted difference between measurement z_k and prediction $H\hat{x}_k^-$

$$\hat{x}_k = \hat{x}_k^- + K(z_k - H\hat{x}_k^-), \tag{4.11}$$

where the difference $z_k - H\hat{x}_k^-$ between measurement and prediction is called the residual. The matrix K is the Kalman gain, the actual filter, that minimizes the a posteriori error covariance (4.10). While a detailed derivation exceeds the purpose of this thesis, one possible solution to this minimization problem takes the form

$$K = P_k^- H^T (H P_k^- H^T + R)^{-1} = \frac{P_k^- H^T}{H P_k^- H^T + R}, \tag{4.12}$$

where R is the measurement error covariance. When R approaches zero, the gain K weighs the residual more, while when the a priori estimate covariance P_k^- goes to zero, the residual is weighed more.

Figure 4.12 shows a schematic depiction of the recursive Kalman filter process at the track points $k-1$ to $k+1$ with step-wise prediction and filtering along the track; the cones around the path estimates represent the uncertainties at that step. Despite the initially large uncertainty, each step in the Kalman Filter improves knowledge of the trajectory. As each subsequent step is added, the track reconstruction rapidly converges. The plot also includes the final track estimate after the smoothing in opposite direction as well as the true particle track.

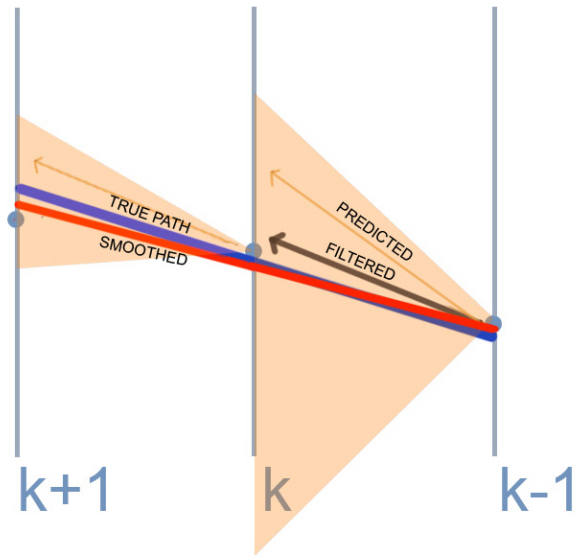

Figure 4.12: The recursive prediction and filtering steps along a track and the smoothed estimate within the Kalman track fitter.

4.2.3 Author Contribution to Development

While the development of the fissionTPC used in the anisotropy measurement was a truly collaborative effort within NIFFTE, the author contributed significantly to the detector work. The author carried out gas optimization studies to select the current fill gas and completed the extension of the gas system to mix flammable gases. The author aided in the development of the current target loading procedure in the glovebox at LANSCE. It was further the author's responsibility to maintain and troubleshoot the fissionTPC experiment during the operation in-beam at LANSCE. The author contributed to the software framework as well, developing the technique to improve data handling by storing it in convenient ROOT trees, working on neutron time of flight signal processing algorithms, and mentoring two undergraduate students who wrote tracking and simulation software for the project.

4.3 The Los Alamos Neutron Science Center

Work on different parts of the fissionTPC is done in various collaboration institutes; the main experimental facility, however, is the Weapons Neutron Research (WNR) facility at the Los Alamos Neutron Science Center (LANSCE) [76]. The LANSCE facility houses an 800 MeV linear proton accelerator, which produces neutrons at two different spallation targets [77]. Target-4 delivers neutrons at intermediate and fast neutron energies to WNR, while Target-2 is moderated and produces thermal neutrons for the Lujan Center. The proton beam itself is also used for nuclear physics research and an ultra-cold neutron source is available as well. All fissionTPC experiments that require a neutron beam are carried out at the target-4 90 degrees left (90L) flightpath at WNR, which is primarily dedicated to the fissionTPC experiments during the whole beam cycle.

Figure 4.13 depicts the linear accelerator, the proton storage ring that delivers proton packets to target-2 for the Lujan Center, and target-4 and its associated flightpaths. Figure 4.14 shows an aerial photograph of the whole LANSCE facility, where the accelerator tunnel can be seen on the right and the red circle indicates the location of target-4 and the 90L flightpath.

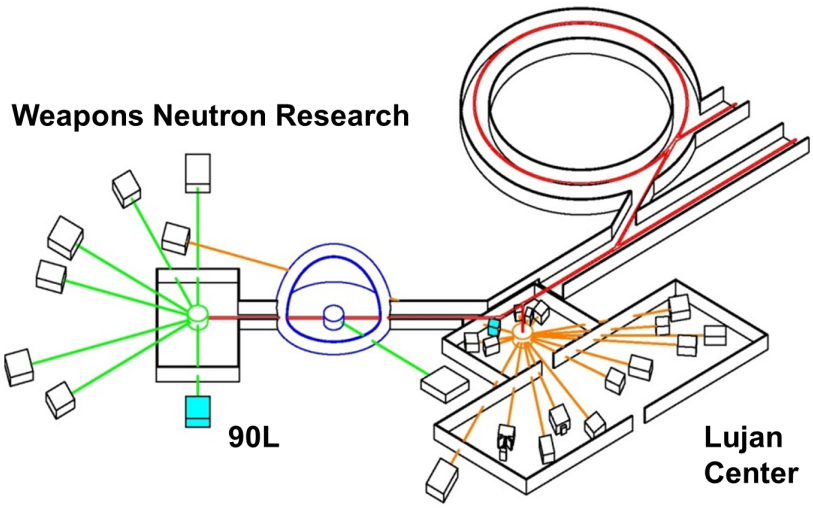

Figure 4.13: A schematic depiction of the LANSCE facility with the Lujan Center, WNR and the fissionTPC flightpath 90L, which is indicated with the turquoise coloring.

4.3.1 The Linear Accelerator

The LANSCE linear accelerator, or linac, produces beams of protons which are accelerated using electric fields from radio frequency voltages in drift tubes [78]. The linac is half a mile long and consists of three stages. Protons are produced in a negative hydrogen ion source and pass through the low-energy beam transport system where they are steered, focused and packed into pulses. The beam of protons with an energy of about 750 keV then moves on to the second stage, the drift-tube linac, where the radio frequency drive accelerates the ions to 100 MeV.

Figure 4.14: An aerial photograph of the LANSCE mesa with the linear accelerator building clearly visible to the right and the red circle indicating the area of target-2 and the home of the fissionTPC, flightpath 90L.

The third and longest stage of the accelerator is the side-coupled-cavity linac which is 731 m long, where the protons continue to be accelerated to their final energy of 800 MeV and velocity of 84 % of the speed of light in packet sizes of 250 ps.

4.3.2 The Neutron Source

Target-4 is a very intense high-energy white neutron source and produces neutrons at energies ranging from 0.1 MeV to greater than 600 MeV. Neutrons are produced in a bare unmoderated tungsten cylinder, which is bombarded with the 800 MeV proton pulses from the linac and produces neutrons in spallation reactions. Target-4 currently operates either at 40 or 100 Hz, the frequency at which macropulses are delivered. Each macropulse then contains a number of micropulses, usually spaced by 1.8 μs or 3.6 μs during special operation to determine neutron background (see section 5.4). Target-4 serves six flightpaths;

flightpath 90L is approximately 7 to 15 m long and is primarily dedicated to the fissionTPC experiment. Because of the pulsed nature of the proton and subsequently neutron beam, time of flight measurements of the neutrons are possible. The neutron time of flight determines the neutron energy when flight distance is known, which means that neutron energy dependent measurements are possible on an event by event basis. The distance from the spallation target to the fission detector is determined by placing a carbon filter with a well-known feature in its neutron absorption cross section into the neutron beam. Computational details for the neutron energy determination are described in section 5.3.

4.4 Run Configurations

During the 2014/2015 run cycle, which saw neutron beam on target between 10/23/2014 and 02/08/2015, more than 65 TB of data were collected with a thick backing aluminum target with actinide deposits of 50 μg/cm^2 ^{235}U on one side and ^{239}Pu on the other side. The 95 % Ar/ 5 % Isobutane fill gas was kept at 550 Torr and high voltages were -3000 V on the cathode and -200 V on the MICROMEGAS. Four different data sets were taken: First, autoradiograph data before beam started, where the ^{235}U target was autoradiographed using the material's spontaneous alpha decay. Second, regular physics data with 1.8 μs beam spacing. Third, data to determine the neutron background, like wrap-around (see section 5.4), with 3.6 μs beam spacing. And fourth, data with a carbon filter in beam to determine the flightpath length from the spallation target to the detector cathode (see section 5.3).

Chapter 5

Data Analysis

This chapter gives a step-by-step description of the data analysis process to obtain angular distributions and anisotropy values. Section 5.7 is dedicated to a study of the uncertainties associated with the analysis.

5.1 Raw Data Reconstruction

The first step in the data analysis is the digital reconstruction of the raw signals from the fissionTPC, transforming timed signals into three-dimensional particle tracks. The principals of reconstruction and tracking are described in section 4.2.2. The current data set relies on standard NIFFTE reconstruction methods and uses simplified versions of track finding and fitting introduced in section 4.2.2. One challenge for the three-dimensional reconstruction in the fissionTPC is that the reconstruction package is based on an assumption of the electron drift speed in the gas. Different drift speeds will yield different results for the z-position of signals in the fissionTPC as they are inferred from the time information. The resulting uncertainties related to drift speed and the bias associated with tracking are treated in sections 5.7.2 and 5.7.9.

5.2 Fission Fragment Identification

The sensitivity of the fissionTPC covers a wide range of events and particles. The fissionTPC detects protons from (n,p)-reactions and elastic scattering in the fill gas, spallation alpha particles, as well as spontaneous alpha decay and fission fragments from the target. Utilizing the three-dimensional track reconstruction capability of fissionTPC signals one can distinguish fission fragments from other particles with relative ease. The instrument allows to point to the origin of a particle track, determine its polar angle, track length and energy deposited along the track. While all these features are currently being developed into a more advanced particle identification algorithm, it was deemed sufficient for the current analysis to simply impose an energy selection cut on the detected particle tracks to identify fission.

Figure 5.1 shows a plot of the track length versus uncalibrated energy for a representative sample of the data set, with the current selection cut indicated. In this figure different particle types occupy different regions, making it useful for particle selection. At energies beyond the selection cut the data clearly indicate the double hump of fission fragments; while data points below the cut originate primarily from alpha particles. The uncertainty in particle identification associated with the choice of selection cut on the data will be discussed in section 5.7.3. In this context one should note the apparent tail of heavily degraded fission fragments to the bottom left of figure 5.1. Including these degraded fragments in a further analysis with more advanced particle identification will likely lead to better statistics in the lower (parallel to target) end of the angular distributions. In addition to a simple energy threshold, all fission fragments included in the anisotropy analysis were selected to clearly originate within the target area. As mentioned in section 4.2.1, the isotope deposit on the target backing has a 1 cm radius. Only tracks which originated in a radius

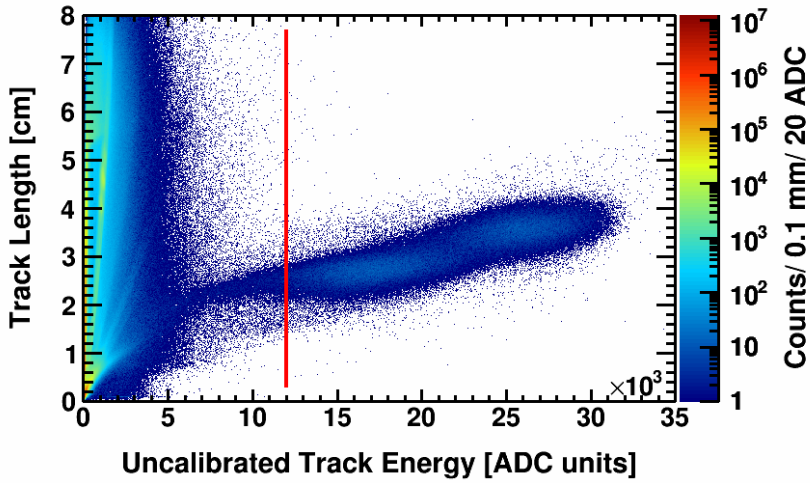

Figure 5.1: Track length versus uncalibrated energy for a representative sample of the current data set. The selection cut at 12000 ADC units is indicated in red.

≤0.8 cm were considered. Figure 5.2 shows the vertices of all fission fragments selected by the energy cut and the circle indicates the 1 cm radius of the active deposit. In addition to the two tracking selection cuts, tracks also were required to be associated with a neutron time of flight greater than zero, which additionally removes less than 0.1 percent of events, where the time of flight algorithms fail. Figure 5.3 shows the finally selected data associated with fission fragments in a length versus uncalibrated energy plot.

5.3 Neutron Time of Flight Calibration

The incident neutron energy is determined using the time of flight (TOF) technique based on the information from the pulsed nature of the proton and subsequent spallation neutron beam, as described in section 4.3. Each proton micropulse produces a range of neutron energies, where the specific energy causing the fission event can be determined based upon the neutron flight time between

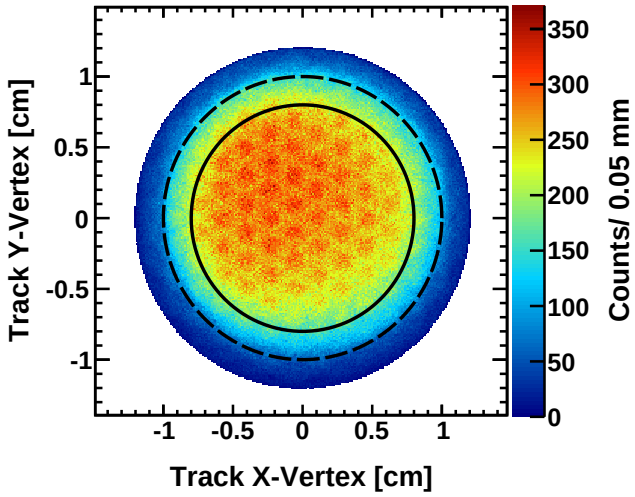

Figure 5.2: Track vertices for all fission fragments as determined by the energy selection. The size of the active deposit and the selection cut are indicated by the dashed and solid circle, respectively.

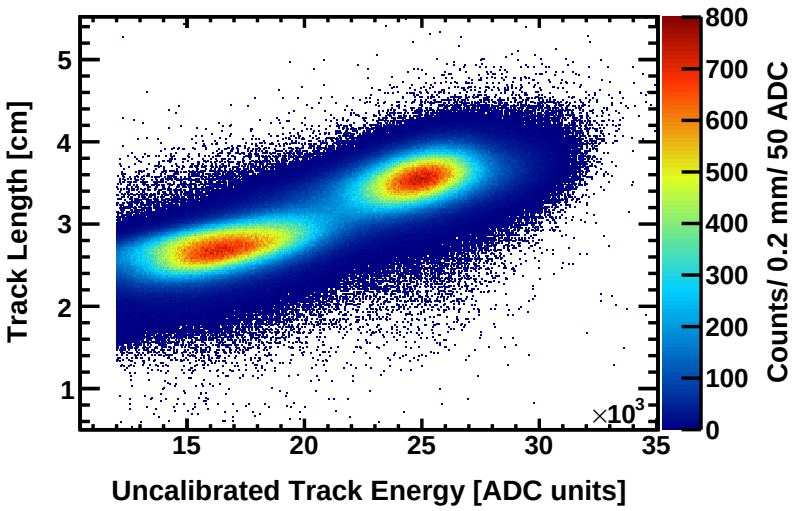

Figure 5.3: Track length versus energy for all fission fragments selected for the anisotropy analysis. The double humped distribution is characteristic for fission.

the spallation target and the fissionTPC in the experimental area. From the proton pulse timing the time of impact on the spallation target is known, which serves as the start signal t_0; the time stamp of a fission event on the fissionTPC actinide target cathode is the second signal t_1 needed for the TOF calculation. With the distance between the tungsten spallation target and the fission target in the fissionTPC, the neutron speed and therefore energy can be determined. The relativistic kinetic energy of a particle is given by

$$E_{kin} = m_n c^2 \left(\frac{1}{\sqrt{1-\beta^2}} - 1 \right), \tag{5.1}$$

where $\beta = \frac{v}{c} = \frac{L}{ct}$ with velocity v, speed of light c, time of flight t and flightpath length L. For a neutron with mass $m_n = 939.6$ MeV/c^2, time in ns and length in m, equation (5.1) can be written as

$$E_{kin,n}[MeV] = 939.6 \left(\frac{1}{\sqrt{1 - 11.1 \frac{L^2}{\Delta t^2}}} - 1 \right), \tag{5.2}$$

where

$$\Delta t = t_1 - t_0. \tag{5.3}$$

5.3.1 The Photofission Peak

One important feature of the TOF spectrum is the photofission peak at short times of flight, shown in the inset in figure 5.4. The photofission peak signifies the first fission events detected in the fissionTPC after the start of an accelerator micropulse. The fission events in that characteristic peak are induced by gamma-rays produced in the spallation process on the tungsten target. As the impinging proton beam is a narrow packet of only 250 ps and the gamma radiation moves at speed of light, the gamma time of flight is very well defined, which means one can deduce the neutron energy resolution from the width of the photofission

peak, see section 5.7.4. For this purpose the peak is fitted with a Gaussian and mean, standard deviation σ and FWHM are determined from the fit.

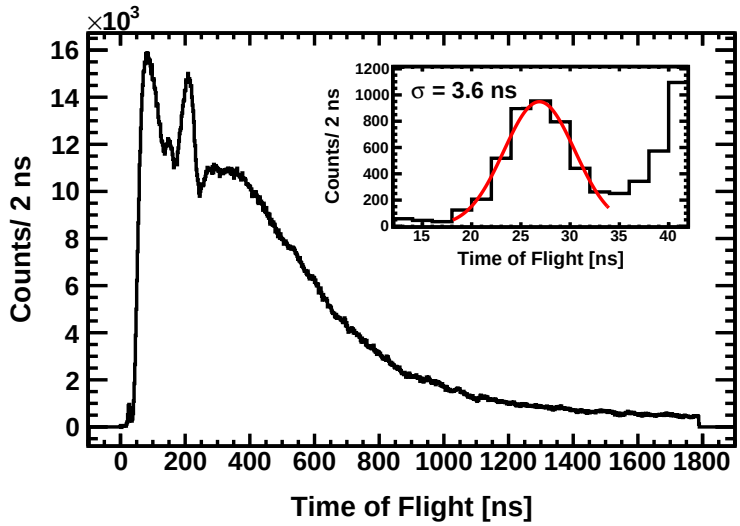

Figure 5.4: The neutron time of flight spectrum for the selected fission fragments. The inset shows the fitted photofission peak with a standard deviation $\sigma = 3.6$ ns.

5.3.2 Flightpath Length

The determination of the neutron energy requires the accurate knowledge of the distance between the spallation target and the actinide target in the fissionTPC (see equation (5.2)). For this absolute time of flight spectrum calibration a carbon filter is introduced in the neutron beam between the spallation target and the fissionTPC. Carbon has a well known resonance in its neutron absorption cross section at 2078.0±0.3 keV, see figure 5.5 . The neutron time of flight spectrum in the fissionTPC therefore presents with a small notch at a certain time due to the carbon filter in the beam, see figure 5.6. It is identified by using the larger resonance feature also labeled in figure 5.6 for orientation. One can treat the calculation involving the 2.078 MeV neutron non-relativistically, as its

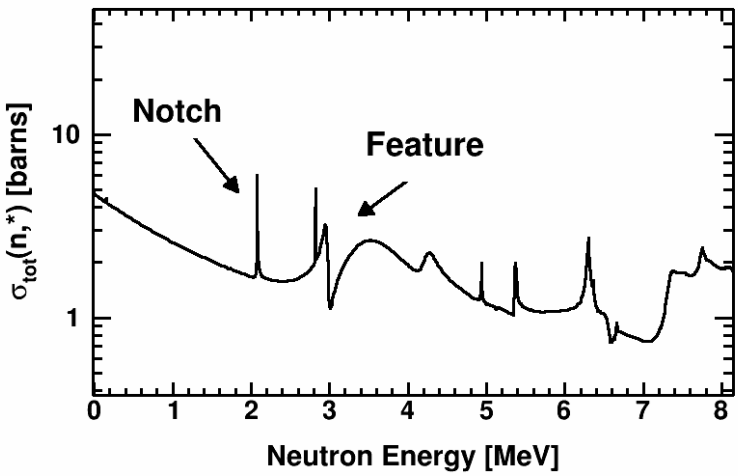

Figure 5.5: The total cross section for ^{12}C versus incident neutron energy. The two resonance features seen in the subsequent TOF spectrum are indicated.

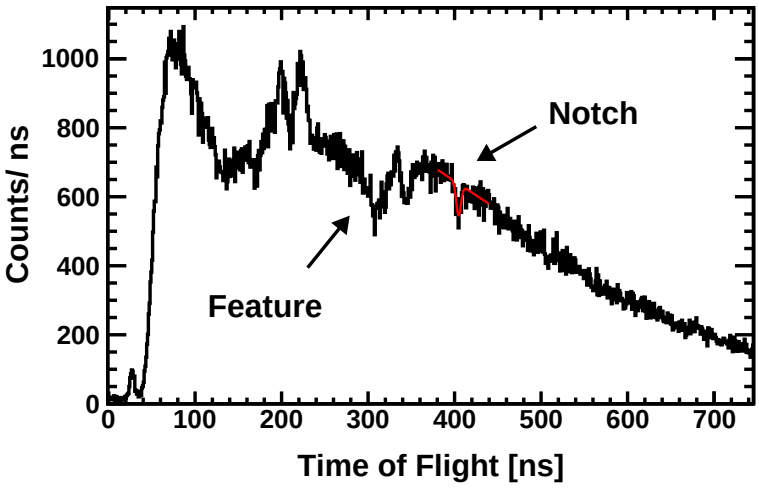

Figure 5.6: The neutron time of flight spectrum with a carbon filter in place. The notch and the larger feature as seen in figure 5.5 are indicated.

velocity

$$v = \sqrt{\frac{2E_{kin,n}[\mathrm{MeV}]}{m_n[\mathrm{MeV/c^2}]}} = 0.06c \tag{5.4}$$

is well below the speed of light c. The 2.078 MeV neutron travels the distance between spallation and fissionTPC target ΔL in the time it takes the gammas to arrive at the fissionTPC Δt_γ plus the time difference between photofission peak and carbon feature $\Delta t_{c\to\gamma}$. The neutron's classical kinetic energy is

$$E_{kin,n} = \frac{m_n v^2}{2} = \frac{1}{2} m_n \frac{(\Delta L)^2}{(\Delta t)^2}, \tag{5.5}$$

where

$$\Delta t = \Delta t_{c\to\gamma} + \Delta t_\gamma \tag{5.6}$$

and

$$\Delta t_\gamma = \frac{\Delta L}{c}. \tag{5.7}$$

The time $\Delta t_{c\to\gamma}$ is determined from the TOF spectrum with the carbon feature as seen in figure 5.6. It follows that

$$E_{kin,n} = \frac{1}{2} m_n \frac{(\Delta L)^2}{(\Delta t_{c\to\gamma} + \frac{\Delta L}{c})^2}, \tag{5.8}$$

which can be solved for ΔL:

$$\Delta L = \frac{\Delta t_{c\to\gamma} c}{\sqrt{\frac{m_n c^2}{2E_{kin,n}}} - 1}. \tag{5.9}$$

For the 2014/2015 run cycle the path length was 8.028 m. Before calculating the neutron energy spectrum the TOF spectrum is shifted so that the photofission peak mean sits at the correct time, as given by equation (5.7).

5.3.3 Neutron Energy

Figure 5.4 shows the resulting TOF spectrum for the fission events selected using the particle identification criteria defined in the previous section. The photofission peak width is $\sigma = 3.6$ ns or FWHM = 8.5 ns (see figure 5.4). One should

note that the photofission peak resolution will be improved in future fissionTPC data analyses, as the timing extraction algorithm is still being developed. The time of flight resolution is the driving factor in the neutron energy uncertainty and therefore binning of the final anisotropy result, where the bin size is equal to or greater than the uncertainty on the neutron energy. Section 5.7.4 explicitly treats the determination of the neutron energy uncertainty derived from the timing resolution and details the used neutron energy binning. Figure 5.7 shows the resulting neutron energy spectrum.

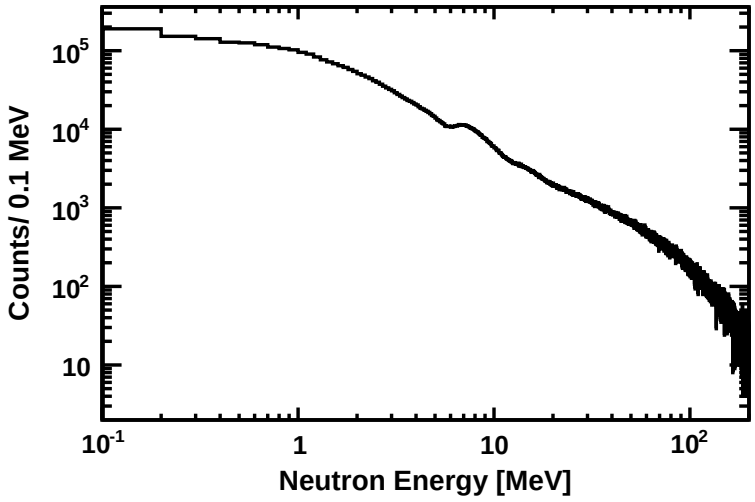

Figure 5.7: The neutron energy spectrum of all selected ^{235}U fission events as calculated from the calibrated neutron time of flight.

5.4 Wrap-Around Correction

After selecting fission fragments and determining their neutron energy, a few corrections need to be applied to the data before the angular distributions can be extracted. A very important correction is related to the structure inherent

to the pulsed neutron beam, as described in section 4.3. The spacing between micropulses is 1.8 μs or 1800 ns, which is the length of a single TOF spectrum as seen in figure 5.4. Slower neutrons with a time of flight greater than 1800 ns will still be on their way to the fissionTPC when a new pulse starts. This effect is called wrap-around or frame overlap. A number of overlapping tails from previous pulses lie underneath every TOF spectrum and need to be subtracted out of the final TOF. One should note that every background neutron due to pulse-wrap is slower than 1800 ns, which translates to all wrap-around neutrons having an energy less than 104 keV in the fissionTPC experiment, according to equation (5.1). As will be described in greater detail in section 5.6.1, an important assumption in the current analysis is that neutrons below the normalization energy of 160 keV lead to isotropic angular distributions and anisotropy of 1. That means that the percentage of wrap-around neutrons introduces a percentage of 'flatness' into the angular distribution and reduces the anisotropy.

The number of wrap-around neutrons is estimated by fitting the tail ends of all macropulses, where no new micropulses are starting, at neutron flight times beyond 1800 ns. The fit function used is a combination of decaying exponentials, accounting for more than only the last micropulse contributing, its principle shape is the following:

$$Fit_{wrap} = C_0 \left[\sum_{micropulses} C_1 + C_2 \mathrm{e}^{-C_3 x_0} + C_4 \mathrm{e}^{-C_5 x_0} \right]. \tag{5.10}$$

The parameters C_1 through C_5 are determined through the shape of the macropulse tails. The fit equation, however, also contains a scaling parameter C_0, which is only invoked if the background below the photofission peak is not sufficiently accounted for. The wrap-around function determined from the fit using C_1 through C_5 is plotted on the TOF spectrum for all events and then scaled with C_0 to fit the background below the photofission peak, as can be seen in figure

5.8. That means that this correction also includes other background, like neutrons that scatter off equipment in the experiment room (room return) and will subsequently have a low energy. The final fit function including scaling is then

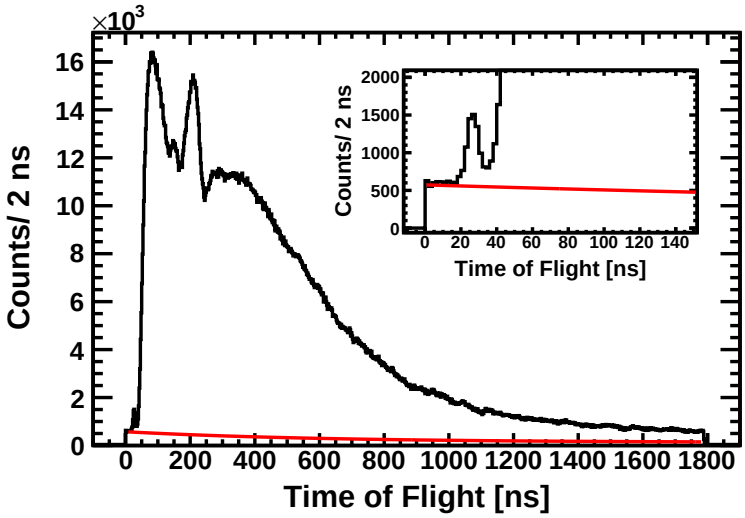

Figure 5.8: The shape of the wrap-around fit describes the background in the time of flight spectrum and is scaled to fit the counts below the photofission peak.

used to determine the number of wrap-around neutrons versus the number of actual counts in each TOF bin.

The percentage of wrap-around neutrons in each neutron energy bin is then used to correct the anisotropy result. If the angular distribution is normalized to 1, the anisotropy A is just the value of the distribution W at $\cos\theta = 1$, as defined in equation (2.31) in section 2.2. The measured anisotropy value A_{meas} in that particular neutron energy bin is then the sum of the real angular distribution A_{real} plus a flat contribution $A_{wrap} = 1$ from wrap-around neutrons (it is assumed that the low energy neutrons produce a flat angular distribution):

$$A_{meas} = (1 - p_{wrap})A_{real} + p_{wrap}A_{wrap}, \tag{5.11}$$

where p_{wrap} is the percentage of wrap-around neutrons in that energy bin. The

corrected anisotropy value is then

$$A_{real} = \frac{A_{meas} - p_{wrap}}{1 - p_{wrap}}. \tag{5.12}$$

While the described analytical method of correcting for wrap-around works well for the anisotropy value, the individual angular distributions as reported in appendix C should in principle be corrected by subtracting a flat distribution and re-fitting. As the correction is in the sub-percent level in most cases, this procedure has been omitted. The anisotropy values that can be extracted from the distributions in appendix C differ therefore slightly from the reported anisotropy result in section 6.1 and appendix A.

5.5 Linear Momentum Transfer

Although the mass of the incident neutron is much smaller than the mass of the actinide, it can transfer some momentum to the target nucleus and subsequently to the fission fragments. Forward fragments will receive a boost in energy and therefore an enhancement at forward angles will be observed, while the opposite is true for backwards fragments. The effect needs to be corrected for. The change in kinetic energy of fission fragments and their angles can be calculated from conservation of momentum and energy in the center-of-mass (CM) system of incident neutron and actinide target atom. The kinematics for this part of the fission process are classical and non-relativistic. The incident neutron is also treated non-relativistically for simplicity. A more detailed derivation can be found in [79].

The velocity of the CM system relative to the laboratory environment is defined as $\vec{V}^{CM}$ and the x-direction shall coincide with the incident neutron beam direction. The target nucleus velocity in the lab system can be expressed

as

$$\vec{V}_A^L = \vec{V}_A^{CM} + \vec{V}^{CM} = 0, \tag{5.13}$$

which is zero in the laboratory system, therefore

$$\vec{V}_A^{CM} = -\vec{V}^{CM}. \tag{5.14}$$

Conservation of momentum in the CM system implies

$$m_A \vec{V}_A^{CM} + m_n \vec{V}_n^{CM} = 0. \tag{5.15}$$

The velocity of the neutron in the lab system can be expressed as

$$\vec{V}_n^L = \vec{V}_n^{CM} + \vec{V}^{CM} = \frac{m_A}{m_n}\vec{V}^{CM} + \vec{V}^{CM} = \frac{m_A + m_n}{m_n}\vec{V}^{CM}. \tag{5.16}$$

There are no external forces acting on the neutron-target system, so that the velocity of the CM system

$$\vec{V}^{CM} = \frac{m_n}{m_A + m_n}\vec{V}_n^L \tag{5.17}$$

is constant. The velocity of the respective fission fragments in the lab system is

$$\vec{V}_{1,2}^L = \vec{V}^{CM} + \vec{V}_{1,2}^{CM} = \frac{m_n}{m_A + m_n}\vec{V}_n^L + \vec{V}_{1,2}^{CM}, \tag{5.18}$$

where $m_A + m_n = m_{CN}$ is the mass of the compound nucleus before fission. Defining the angle $\theta_{1,2}$ as the polar angle between the respective fission fragment and the beam axis, the x-axis as the beam direction and the y-axis perpendicular to it, the projection of equation (5.18) onto the x-axis gives

$$\mp V_{1,2}^{CM} \cos\theta_{1,2}^{CM} = \mp V_{1,2}^L \cos\theta_{1,2}^L - \frac{m_n}{m_{CN}} V_n^L, \tag{5.19}$$

and onto the y-axis

$$\mp V_{1,2}^{CM} \sin\theta_{1,2}^{CM} = \mp V_{1,2}^L \sin\theta_{1,2}^L. \tag{5.20}$$

For the speed of the respective fragments in the CM system, these equations are squared and summed to get

$$(V_{1,2}^{CM})^2 = (V_{1,2}^L)^2 + (\frac{m_n}{m_{CN}} V_n^L)^2 \pm 2\cos\theta_{1,2}^L \frac{m_n}{m_{CN}} V_n^L V_{1,2}^L. \tag{5.21}$$

The kinetic energy of the fragments in the CM system is obtained by using $E_i = \frac{mv^2}{2}$ and multiplying the speed $(V_{1,2}^{CM})^2$ from equation (5.21) with $m_i/2$:

$$E_{1,2}^{CM} = E_{1,2}^L \pm 2\frac{\sqrt{E_{1,2}^L m_{1,2} E_n^L m_n}}{m_{CN}} \cos\theta_{1,2}^L + \frac{m_n m_{1,2}}{m_{CN}^2} E_n^L, \tag{5.22}$$

where the (+)-sign now stands for the backwards upstream direction and the (-)-sign for the forward (beam) direction fragment. Similarly to the kinetic energy the fragment angles also have to be corrected. The angle in the CM frame is

$$\cos(\theta)_{1,2}^{CM} = \sqrt{1 - \frac{E_{1,2}^L}{E_{1,2}^{CM}}(1 - \cos^2(\theta)_{1,2}^L)}. \tag{5.23}$$

Since the fragment masses are not measured in this analysis, an approximation is made, where neutron emission is ignored. The sum of the fission fragment masses is then the compound nucleus mass

$$m_1 + m_2 = m_{CN}. \tag{5.24}$$

From momentum conservation

$$m_1 \vec{V_1} = -m_2 \vec{V_2} \tag{5.25}$$

and using $E_i = \frac{mv^2}{2}$ again, it follows that

$$m_1 E_1 = m_2 E_2 \tag{5.26}$$

and subsequently

$$m_1 = \frac{m_{CN} E_2}{E_1 + E_2}, \tag{5.27}$$

which means that the fragment masses can be estimated based on the fragments' energies. Since with the thick backing only one fragment per fission event is measured, the double hump shaped energy distribution of all fission fragments is fitted with two Gaussian functions to determine the energies of an average light and an average heavy fragment, as seen in figure 5.9. The sum of the two average fragments is used instead of event-per-event energies in equation (5.27). Also equation (5.24) has to be used once more to estimate the mass, as equation (5.27) is based on the energy measurement of the second fragment. The correction to the final anisotropy result is small and only becomes measurable above incident neutron energies of about 20 MeV.

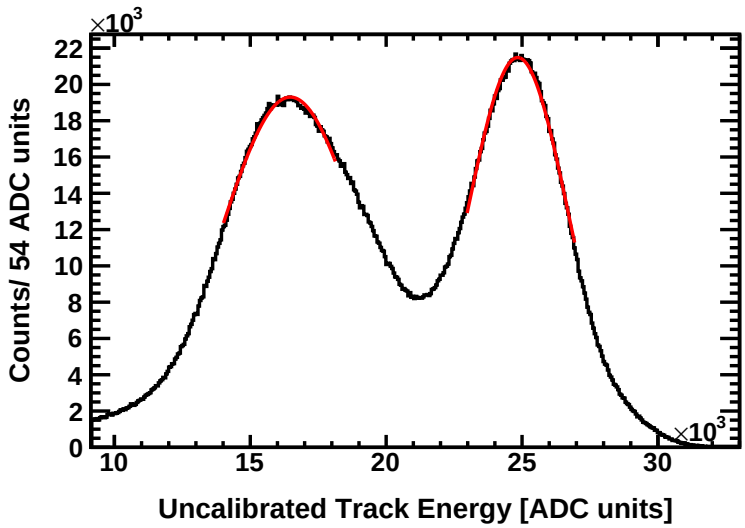

Figure 5.9: The average kinetic energy in the fission event is determined by estimating the energy of an average light and average heavy fragment, as indicated by the Gaussian fits to the double humped energy distribution.

5.6 Anisotropy Calculation

The following section describes the efficiency normalization and fitting of the measured distributions to arrive at physical angular distributions from which anisotropy values can be extracted. The angular distributions W are given as a function of $\cos(\theta)$ from 0 to 1, where $\cos(\theta) = 0$ are angles perpendicular to the neutron beam direction. The angular distributions at each neutron energy are divided into 20 bins of $\cos(\theta)$ to provide good shape information while maintaining statistics.

5.6.1 Angular Efficiency Normalization

The normalization of the angular distributions relies on one basic assumption; the angular distribution of fragments induced by neutrons is isotropic in the lowest available energy bin from 130 keV to 160 keV. This assumption is not inherently correct and the associated uncertainty will be discussed in more detail in section 5.7.7. With this isotropy assumption at incident neutron energies between 130 keV and 160 keV the observed fragment distribution in that energy bin reflects the measured efficiency of the detector. The angular dependent efficiency is a consequence of the target/cathode geometry in the fissionTPC.

Figure 5.10 shows a schematic depiction of the thick backing target with the actinide deposits on each side. If fission fragments are emitted at an angle parallel to the target they will fail to escape the material, meaning that the efficiency for detecting fragments drops off steeply at $\cos(\theta) = 0$ (parallel to the target surface), as can be seen in figure 5.11. Figure 5.11 depicts the angular distribution of fission fragments in the lowest incident neutron energy bin. The distribution is binned into 20 angular bins, the x-error shown corresponds to the bin width, while the y-error reflects counting statistics; this convention is

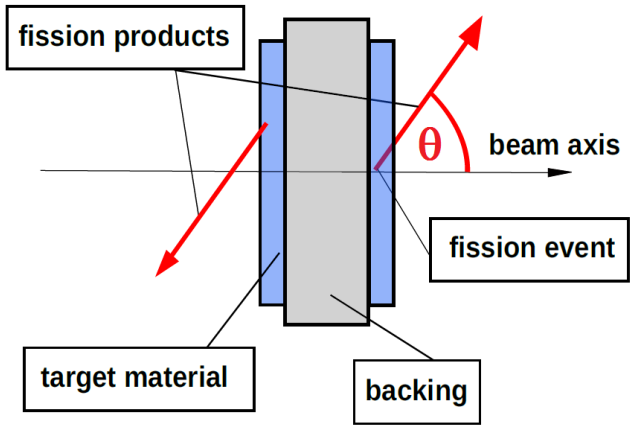

Figure 5.10: The thick backing target with actinide deposits on each side and fission fragments leaving the target material. The geometry determines the efficiency for detecting fission fragments in the fissionTPC.

used for all following depictions of angular distributions. One should note that the efficiency close to $\cos(\theta) = 0$ is very small, but $\cos(\theta) = 0$ is one of the two points in the definition of the anisotropy as given in section 2.2, meaning that a measurement in a configuration where the incident beam is not perpendicular to the target could be more advantageous for this analysis. The issue is, however, remedied by fitting the whole distribution as described in the following section. With the assumption that the obtained efficiency is neutron-energy independent the angular distributions in all energy bins are divided bin-by-bin through the efficiency curve in figure 5.11 and normalized to $W[\cos(\theta) = 0] = 1$ as described previously in equation (2.31) in section 2.2. The procedure yields the normalized, physical angular distributions. The counting statistics error bars in the angular distributions are carried through the arithmetic operations.

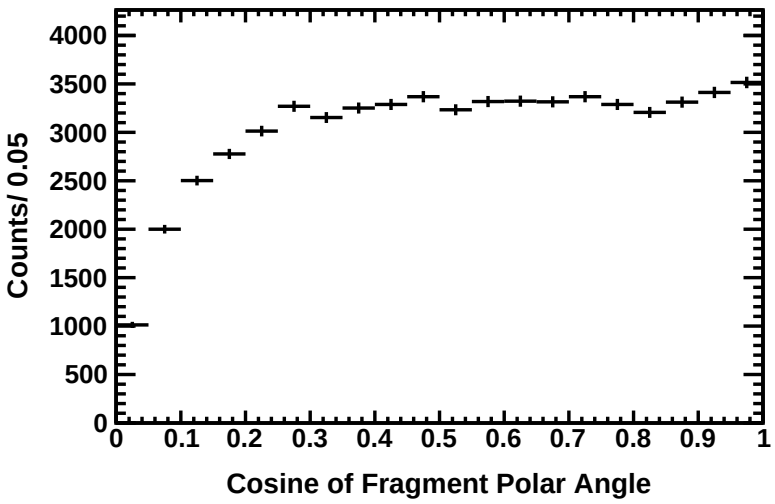

Figure 5.11: The angular distribution of fission fragments in the fissionTPC for incident neutron energies from 130 keV to 160 keV, where emission is assumed to be isotropic. A steep drop-off in efficiency close to $\cos(\theta) = 0$ is observed.

5.6.2 Fitting the Angular Distributions

To extract information like anisotropy or distribution shapes, the corrected angular distributions $W[\theta]$ are fitted with a sum of Legendre polynomials of the form

$$W[\theta] = \sum_n c_n P_{2n}(\cos(\theta)), \tag{5.28}$$

where P_{2n} only includes even Legendre polynomials to conserve forward/backward symmetry. Angular distributions are displayed in $\cos(\theta)$ space, where an isotropic distribution is flat and the form

$$A = \sum_n a_n \cos(\theta)^{2n} \tag{5.29}$$

of equation (5.28) can be used for fitting. Figure 5.12 shows the angular distributions including the polynomial fits at several different neutron energies. Because the distribution $W[\cos(\theta)]$ is normalized to 1 at $\cos(\theta) = 0$ as intro-

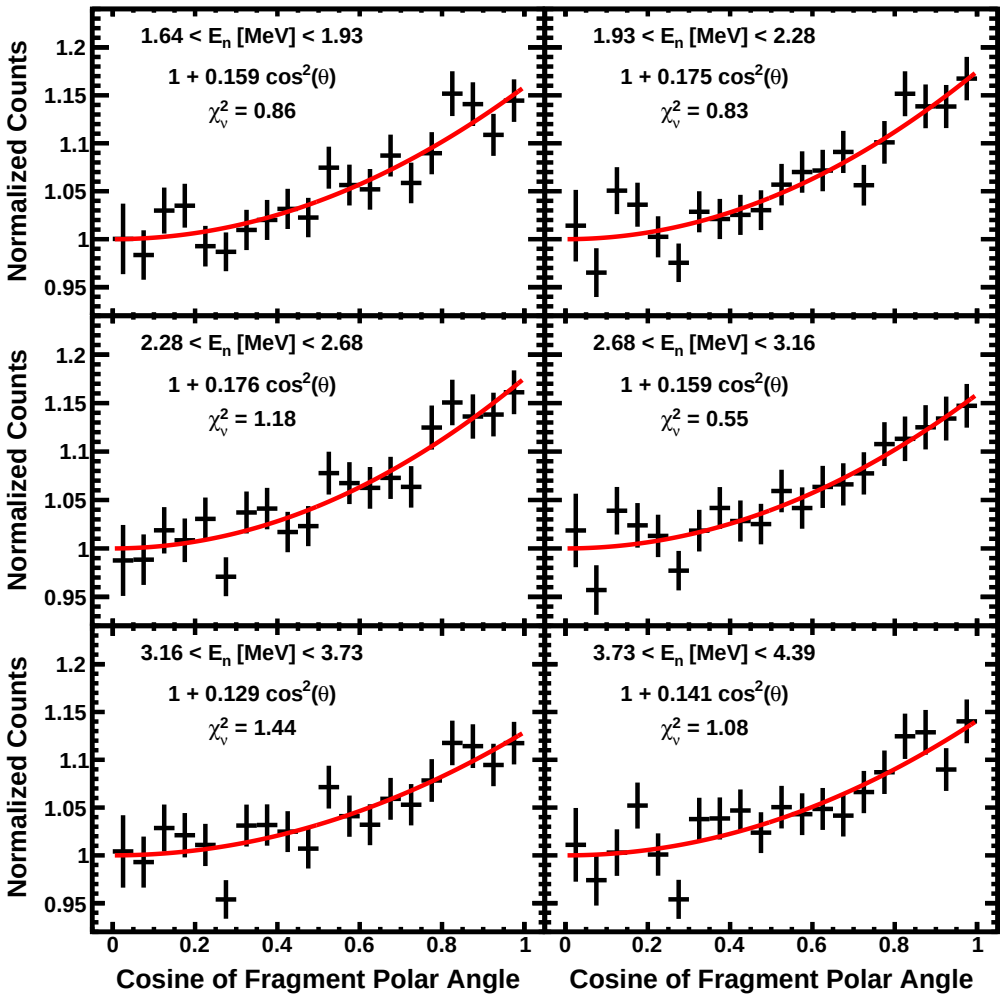

Figure 5.12: The normalized angular distributions in each incident neutron energy bin are fitted with even order polynomials in $\cos(\theta)$ space. The anisotropy is defined as the value of the fit at $\cos(\theta) = 1$. The x-error bars correspond to bin width, the y-error bars reflect counting statistics.

duced in equation (2.31) in section 2.2, the anisotropy is equal to the sum of the fit parameters in the polynomial fit equation (5.29)

$$A = \sum_n a_n. \tag{5.30}$$

The least squares fitting routine used within the ROOT software package determines the fit parameters a_n by minimizing the sum of least squares

$$\chi^2 = \sum_{m=1}^{M} [x_m - x[\cos(\theta), a_n]]^2 / \Delta x_m, \tag{5.31}$$

where M is the number of counts, x_m are the measured data, Δx_m are the statistical errors in each angular bin and $x[\cos(\theta), a_n]$ is the model. The expectation value at the minimum of χ^2 over a normal distribution of measurement values x_m is given by

$$\overline{\chi^2_{min}} = F, \tag{5.32}$$

where $F = M - n$ equals the degrees of freedom. The goodness of fit parameter reduced chi-square χ^2_ν is then given by

$$\chi^2_\nu = \frac{\chi^2_{min}}{F}, \tag{5.33}$$

which should ideally approach 1 for an optimal fit to data x_m with parameters a_n. Figure 5.13 shows the reduced chi-square χ^2_ν for all fits in the current analysis. Different methods of selecting the most optimal order of fit to the angular distributions are found in the literature, see section 3. Including only quadratic order gives acceptable fit quality across all energies in the current data and the associated uncertainties of using only L_2 are discussed in section 5.7.8.

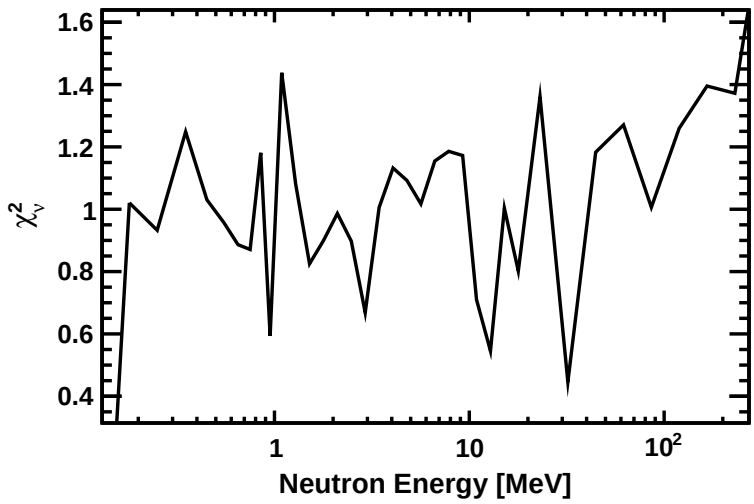

Figure 5.13: The goodness of fit parameter, or reduced chi-square χ^2_ν, for the fits using Legendre polynomials of quadratic order over all neutron energies.

5.7 Uncertainties

The analysis necessary to obtain physical angular distributions and anisotropy values described in the previous sections relies on several corrections which carry an uncertainty. There are also several factors inherent to the experimental method introducing further systematic uncertainties, they are described in detail in the following. The most optimal parameter values for the final anisotropy result were determined using qualitative reasoning; variational analysis of the final anisotropy result was used to quantify the systematic uncertainties.

5.7.1 Statistical Errors

The statistical uncertainty of the anisotropy value can be obtained from linear propagation of uncertainties extracted from the fitting procedure. As seen in equation (5.30), the anisotropy is just the sum of the fitting parameters, while

the uncertainty is defined as

$$\sigma(A) = \sqrt{var(A)}. \tag{5.34}$$

The variance $var(A)$ is

$$var(A) = \sum_{i,j} \frac{\partial A}{\partial a_i} cov(a_i, a_j) \frac{\partial A}{\partial a_j}, \tag{5.35}$$

where the covariance $cov(a_i, a_j)$ can be derived from the fitting routine minimizing χ^2. At its minimum value, the χ^2 introduced in equation (5.31) defines the normal matrix α_{ij}

$$\alpha_{ij} = \frac{\partial^2 \chi^2}{\partial a_i \partial a_j}, \tag{5.36}$$

which in turn gives the covariance

$$\alpha_{ij}^{-1} = cov(a_i, a_j). \tag{5.37}$$

Because of linearity in the fit equations, the partial derivatives in equation (5.35) vanish

$$\frac{\partial A}{\partial x_i} = \frac{\partial A}{\partial x_j} = 1, \tag{5.38}$$

so that the uncertainty is just the square root of the sum over all covariance elements of the fit

$$\sigma(A) = \sqrt{cov(x_i, x_j)} \tag{5.39}$$

obtained with the least squares fitting method. The resulting statistical error is around 1 % for all neutron energy bins up to 100 MeV and then increases to 3 % for higher energies.

5.7.2 Tracking Uncertainty

A potential bias in the three-dimensional reconstruction of particle tracks from raw data in the fissionTPC is difficult to determine. One source of error that

can hint at systematics is the uncertainty in the drift speed. Changing the drift speed value in the reconstruction changes the z-positions of reconstructed signals and the track length and polar angle of reconstructed fission fragment tracks. As those changes are uniform and the angular distributions are normalized during the analysis, the change in drift speed should not affect the final angular distributions in a perfect tracking software. Therefore a variation in the result due to a change in drift speed indicates systematic uncertainties that might result from imperfect tracking. A reasonable method to choose a starting drift speed value is the simulation of the drift conditions in a simulation package like Magboltz [80]. The program takes into account the drift gas and its pressure and temperature, and the electric field. For the current experimental conditions, with 95 % Ar and 5 % C_4H_{10} gas at 550 Torr and 30 °C and with an electric field of 520 V/cm, the simulation yields a nominal drift speed of 3.12 cm/μs.

Another method of choosing a drift speed is selecting a value where the angular distribution of alpha particles emitted in spontaneous decay seems reasonably flat over a region with full angular efficiency in the unnormalized angular distribution. Figure 5.14 shows the unnormalized angular distribution for alpha particles (selected using track length and track energy) from spontaneous alpha decay in the target at different drift speeds. The speed where the distribution seems most isotropic and therefore physical is 2.94 cm/μs, different from the simulation. As a consequence of this discrepancy, the different drift speed values have to be treated as a systematic uncertainty. As previously mentioned, a variation of the drift speed also encompasses further systematic tracking issues. The drift speed selected for the final result is 2.94 cm/μs as indicated for the alpha distribution, which describe the experimental conditions most precisely. For the variational analysis the value is varied up to the value predicted by the

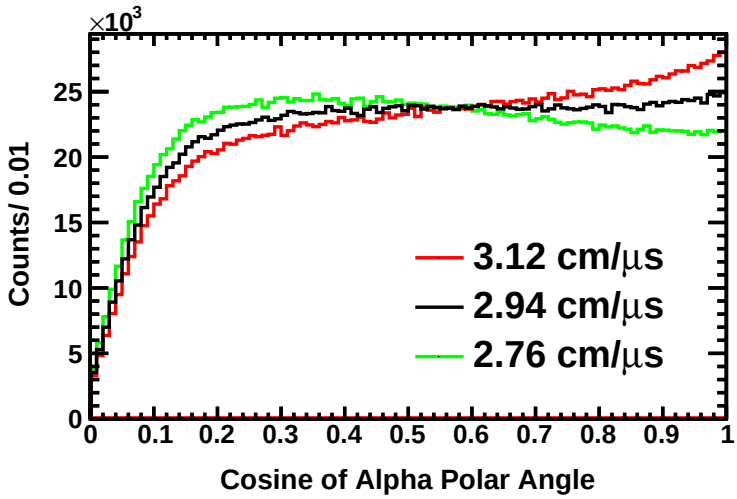

Figure 5.14: The reconstructed angular distribution of alpha particles from spontaneous decay at different drift speeds.

simulation, and down to the value of the alpha determined speed minus the variation between simulation and alpha distribution. The change in the final anisotropy result on the order of 0.5 to 1 % is then the contribution to the uncertainty band. One other concern for the tracking is a slight increase in events in the forward direction close to $\cos(\theta) = 1$, as seen in figure 5.11. To determine the uncertainty introduced by that effect, that part of the angular distribution can be omitted in the fitting, as described in section 5.7.9.

5.7.3 Fission Fragment Identification Uncertainty

It has been mentioned in section 5.2 that the method of choosing fission fragments for the current analysis relies on a simple energy selection. Figure 5.1 in section 5.2 shows a typical track length versus track energy plot from the current ^{235}U data set. It has been discussed that alpha particles are clearly visible in the lower energy portion of the plot as well as the double-humped distribution

of fission fragments at higher energies. The selection cut previously described was put at 12000 ADC to distinguish alpha particles from fission fragments as best as possible. To deduce the uncertainty of the selection cut on the result, a variational study is carried out. The energy threshold is varied in steps of 1000 ADC units to a lowest value of 10000 ADC where one will clearly include alpha particles in the analysis and up to 14000 ADC where large numbers of the lower energy fission fragments are cut out. Figure 5.15 shows the change in anisotropy due to the variation in energy selection. The resulting changes in the anisotropy are largely asymmetric and not obviously showing a trend due to different particle types (alpha particles and fission fragments) being considered. The variation is on the order of 1 to 2 % at incident neutron energies up to 7 MeV and then increases to around 6 % at higher energies and over 10 % in the last neutron energy bin at 230 MeV.

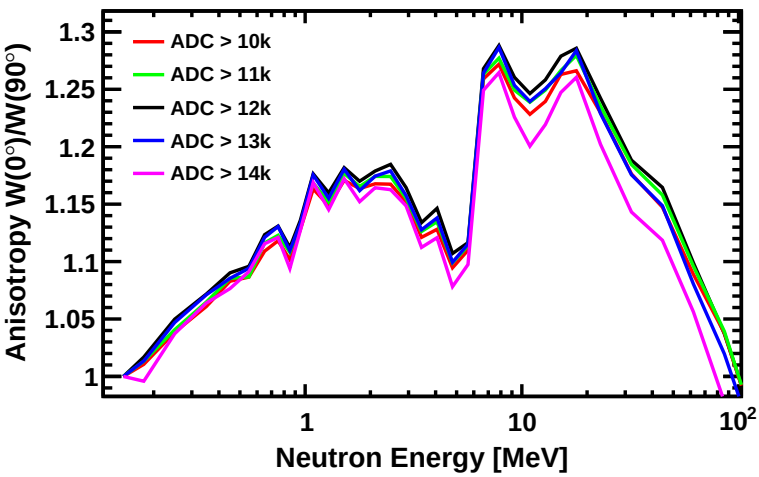

Figure 5.15: Different anisotropy results are obtained by varying the energy selection cut in steps of 1000 ADC units. There is no clear linear relation due to different particle types being included.

5.7.4 Neutron Time of Flight Resolution

The time of flight uncertainty is determined using the photofission peak resolution (FWHM = 8.5 ns, σ = 3.6 ns), obtained from a fit to the peak, see figure 5.4 in section 5.3. Note that the timing uncertainty is the driving force for the neutron energy uncertainty. There is a small contribution from the finite dimension of the spallation target, which changes the flightpath length for neutrons coming from different parts of the target. The effect, however, is extremely small for a flightpath length of 8.028 m and a spallation target size of 7 cm and therefore negligible in the current configuration The uncertainty in timing from the photofission peak resolution is carried through to all neutron energies, which results in an energy uncertainty for each energy. The binning of the anisotropy result is determined by computing neutron energies for all neutron times of flight in steps of σ = 3.6 ns from equation (5.2) and analyzing the spread in neutron energies. The bin width is chosen to be larger than twice the uncertainty in energy. The binning is linear to 1 MeV and then logarithmic with 14 bins/decade up to 20 MeV and 7 bins/decade at higher energies.

5.7.5 Wrap-Around Uncertainty

As described in section 5.4, the wrap-around is corrected for by fitting the shape of the tail of the neutron TOF spectrum. The resulting background can then be subtracted from the final TOF result. It has been shown through MCNP simulations of the neutron beam and the experimental facility that the used fit can differ from the physical distribution by up to 10 %. The simulations were carried out by collaborators at LLNL and the result can be seen in figure 5.16, which shows the difference between the fit to the current data set and the shape of the spectrum as simulated. Subsequently, the fit is scaled by $\pm$10%

to determine the result of the uncertainty on the anisotropy. The error is small (less than 0.1 %) and symmetric around the original result.

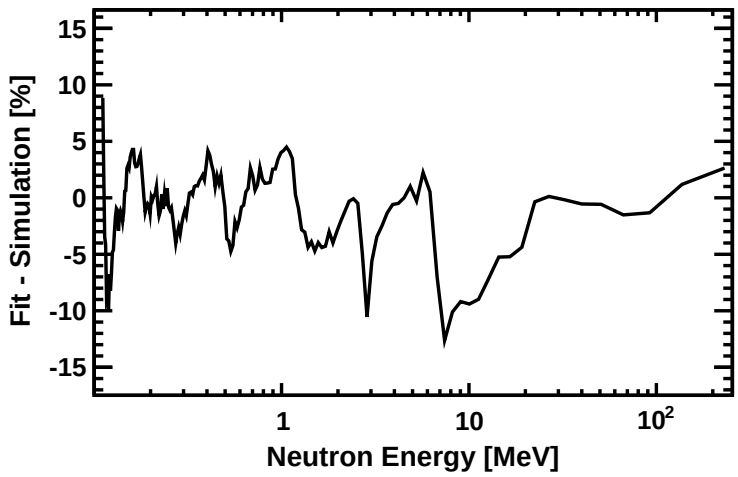

Figure 5.16: The difference between the simulated timing structure shape and the fit used to correct for wrap-around in the data is given in percent at various incident neutron energies.

5.7.6 Momentum Transfer Uncertainty

To correct for the linear momentum transfer of the incident neutron to the fission fragments, an assumption has to be made on the fission fragment mass as described in section 5.5. There are several uncertainties involved with that assumption. First, the mass formula does not include any neutron emission. Second, the formula relies on measuring both fragment energies, while the current thick backing target configuration only allows the measurement of one of the fragments, which is remedied by guessing the two most probable average fragments from the final distribution. Third, the formula relies on the determination of the fragment energy, which the fissionTPC is currently not optimized

for. The individual anode channels in the fissionTPC are not yet gain-calibrated to each other, making energy measurements difficult with a resolution of up to 15 % of the fragment energy. The combined effect of all the assumptions on the mass determination is conservatively estimated to approximately half the width of the mass peak or 15 AMU. From the large uncertainty in mass it follows that there is an uncertainty in the momentum transfer kinematic calculations, which leads to a very small (less than 0.1 %) and symmetric uncertainty in the final anisotropy result.

5.7.7 Efficiency Normalization Uncertainty

As mentioned in section 5.6.1 the anisotropy result relies on the measured detector efficiency based on the assumption that the normalization energy bin of 130 keV to 160 keV exhibits isotropic angular distributions. This assumption is not necessarily correct and the calibration point is almost chosen at random. It is a fact that at very low neutron energies below 10 keV one would only expect s-wave contributions to the states of the nucleus which would yield an isotropic angular distribution. The lowest available energy bin in the current experiment has significantly higher neutron energies, but the expectation is that p-wave contributions would also exhibit isotropic behavior in the lowest spin configuration. The uncertainty on this assumption can not be quantified at the moment and is therefore not included in the total uncertainty in the result, an additional measurement at a low energy neutron source should be made in the future with an overlap into the current energy region. The current anisotropy result has to be read with respect to the normalization point, keeping in mind that it is based on the described assumption.

5.7.8 Fit Selection Uncertainty

The angular distributions are fitted with Legendre polynomials of even orders. As described in section 5.6.2 only quadratic order terms are included in the final result. Including higher orders only gives marginal improvement in the goodness of fit parameter reduced chi-square χ^2_ν while increasing the statistical uncertainty, which means the quadratic fit is consistent with information available in the current data. Previous anisotropy data had been fit with fixed orders of 2 or 4, or the highest order of the fit had been varied with χ^2_ν up to order 6 in each respective neutron energy bin. All mentioned methods have been used to compute the anisotropy and the deviation from quadratic fits is defined to be an uncertainty in the final result. Similar to the fission fragment identification uncertainty the contribution is largely asymmetric, as including higher fit orders seems to systematically lower the anisotropy result, which can be seen in figure 5.17. The uncertainty is on the order of 1 to 5 % and rises to 10 % in the last neutron energy bin at 230 MeV.

5.7.9 Fit Range Uncertainty

In the current analysis the full angular distribution is fitted to obtain the anisotropy result. As mentioned in section 5.6.1, the efficiency for detecting fission fragments in the current configuration drops off steeply close to $\cos(\theta) = 0$, which means that there is very low statistics at one of the points where the anisotropy is defined. Another area of concern is in the forward or beam direction $\cos(\theta) = 1$, where the angular distributions at all neutron energies seem to exhibit an unexpected rise in events. Possible explanations include a tendency of the tracking software to fit in the forward direction or other issues in tracking because of charge saturation of individual channels. The two areas of concern

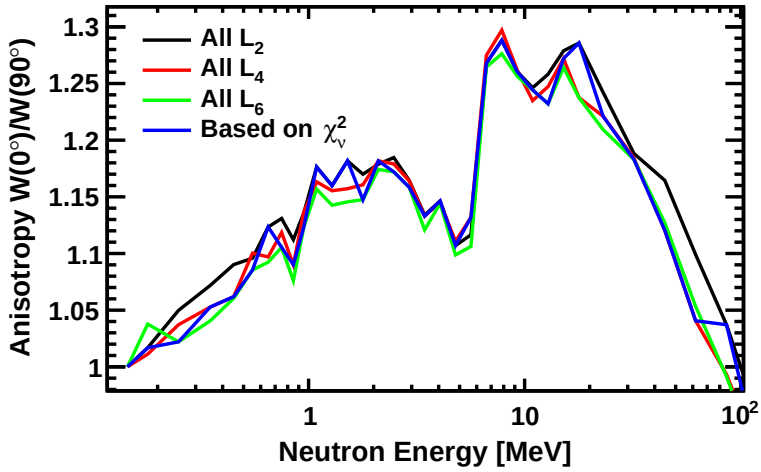

Figure 5.17: The anisotropy result for including different orders in the polynomial fit, either using a specific order across all energies or choosing the highest order in each bin based on goodness of fit χ^2_ν.

(efficiency and forward-peak) can be observed in a typical angular distribution before the normalization step described in 5.6.1, see figure 5.11. Although it generally seems like both effects are uniform over all neutron energies and therefore negligible after normalization, a variational analysis using different fit ranges shows that one of the effects, the forward peaking, introduces additional uncertainty in the final anisotropy result. By studying the anisotropy result obtained with a fit from $\cos(\theta) = 0.4$ to $\cos(\theta) = 1$ and comparing it to the result with a full range fit it is found that the lower cosine region does not introduce additional uncertainty. With the same approach one can fit from $\cos(\theta) = 0$ to 0.8 and from $\cos(\theta) = 0$ to 0.9 and compare to the original result. It can be seen in figure 5.18 that the forward peaking issue does have an effect. The limited fit ranges change the result by about 1 to 3 %.

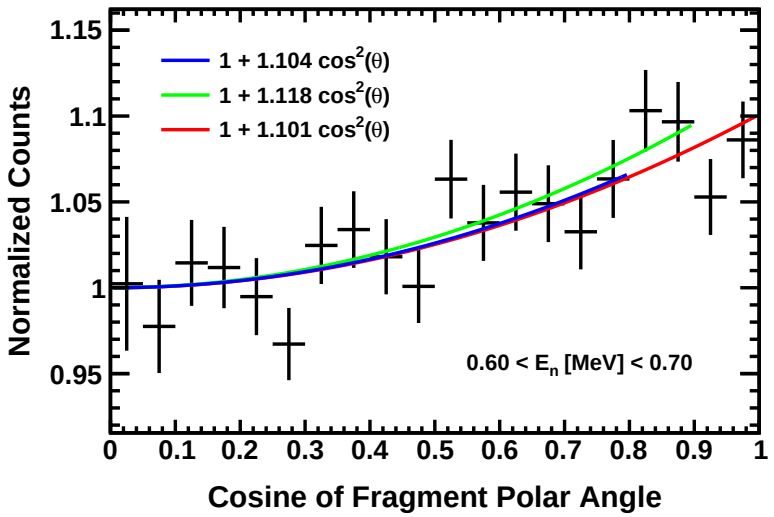

Figure 5.18: The fit result changes when including only a limited range in the angular distribution, hinting at an additional uncertainty from the forward peaking issue.

5.7.10 Target Contamination

Although great care is exercised during fabricating the ^{235}U target as described in section 4.2.1, one can not fully avoid contamination with traces of other uranium isotopes. ^{233}U, ^{234}U, ^{236}U and ^{238}U are all present in small amounts in the target, as determined using destructive mass spectrometry at LLNL. The atom percentages of the isotopes in the order mentioned are 0.02 %, 0.035 %, 0.18 % and 0.2 %, which means that less than half a percent of target atoms are contaminants. All present uranium isotopes have fission cross sections on the order of magnitude of ^{235}U, meaning that less than half a percent of fission fragments are from contaminants. Figure 5.19 shows the atomic percentages multiplied by the cross section of the various isotopes at distinct neutron energies in percent of the same value obtained for ^{235}U. The small uncertainty is considered too insignificant to be included in the final result.

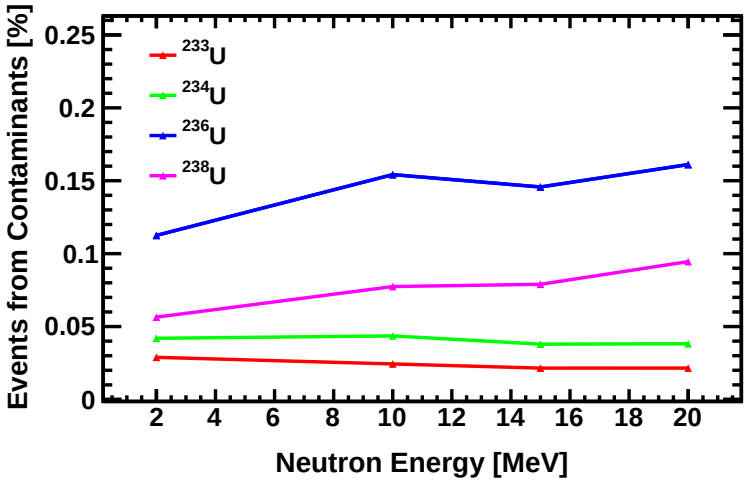

Figure 5.19: A comparison between expected ^{235}U and contaminant isotope fission events in percent, obtained by multiplying the atomic percentage with the cross section for each isotope and given as percentage of the value obtained for ^{235}U.

5.7.11 Resulting Uncertainty Band

The individual systematic uncertainties described in the previous sections are assumed to be independent and can therefore be added in quadrature to obtain the total uncertainty. Some parts of the analysis, like the fission fragment identification selection, or the fit order selection, produce asymmetric uncertainties, which results in an asymmetric uncertainty band around the result. The parameter values for the anisotropy result have not been chosen so the result would fall in the center of the uncertainty band, but to represent the most optimal result based on qualitative reasoning. In the case of fission fragment selection the energy selection cut was placed at the point of greatest separation between energy curves from alpha particles and fission fragments. For the fitting of the angular distribution the simplest fit that represented the data with good goodness of fit parameters was chosen. The uncertainty introduced by the arbitrary

normalization of the anisotropy to 1 in the lowest energy bin, see section 5.7.7, can not be quantified at this moment and is omitted in the result. The uncertainty from target contamination is negligible and is also omitted. The final uncertainty band can therefore be described by

$$\sigma_{Tot} = \sqrt{\sigma_{Stat}^2 + \sigma_{Drift}^2 + \sigma_{FissID}^2 + \sigma_{Wrap}^2 + \sigma_{Moment}^2 + \sigma_{Fit}^2 + \sigma_{Range}^2} \tag{5.40}$$

where $\sigma_{Stat}, \sigma_{Drift}, \sigma_{FissID}, \sigma_{Wrap}, \sigma_{Moment}, \sigma_{Fit}$ and σ_{Range} are the statistical uncertainty, the uncertainty from varying the drift speed, the track energy selection uncertainty, the wrap-around uncertainty, the neutron momentum transfer uncertainty, the fit order selection uncertainty and the fit range selection uncertainty respectively, as discussed in the previous sections. The quadratic sum of uncertainties is calculated separately for positive and negative errors, which yields an asymmetric uncertainty band. The resulting uncertainties are shown in the following chapter 6 and a detailed numerical table of the most important contributions can be seen in appendix B.

5.8 Covariances

While statistical uncertainties depend on the bin size at each neutron energy, they are completely uncorrelated between neutron energies. The systematic uncertainties, however, are correlated between neutron energies. A covariance or correlation matrix can deliver more information on the areas and strength of correlation. Analytically, the covariance of a quantity a_i in energy bin i and the quantity a_j in the energy bin j is given by

$$cov(a_i, a_j) = \int\int (a_i - \langle a_i \rangle)(a_j - \langle a_j \rangle) p(a_i, a_j) da_i da_j, \tag{5.41}$$

which is also the second moment of the probability distribution function $p(a_i, a_j)$ of a_i and a_j. In the case of the anisotropy calculation there is no analytical

expression for the largest uncertainties, therefore one can look at various experimental realizations of a_i and a_j. For a number of realizations k of a_i and a_j around mean (or in this case most optimal) values $\langle a_i \rangle$ and $\langle a_j \rangle$ the covariance elements cov_{ij} are defined as

$$cov(a_i, a_j) = \frac{1}{k} \sum_k (a_i^k - \langle a_i \rangle)(a_j^k - \langle a_j \rangle). \tag{5.42}$$

To interpret the covariance matrix it is necessary to calculate the correlation matrix, which is a normalized version of the covariance matrix with values between -1 and 1, where -1 means fully anti-correlated, 1 means fully correlated and 0 means not correlated. The correlation matrix elements $corr_{ij}$ are computed by

$$corr(a_i, a_j) = \frac{cov(a_i, a_j)}{\sqrt{cov(a_i, a_i) cov(a_j, a_j)}} = \frac{cov(a_i, a_j)}{\sqrt{\sigma_i^2 \sigma_j^2}}. \tag{5.43}$$

The two largest uncertainties in the anisotropy result are the selection of the highest order of fit (see section 5.7.8) and the track energy selection cut used to identify fission fragments (see section 5.7.3). Both those uncertainties are consistently larger than the statistical uncertainty as will be shown in section 6.2 and will most likely influence how the result is treated in a nuclear data evaluation. It is therefore useful to focus on studying covariances of those two uncertainties. One important point to note is that the number of samples k in equation (5.42) has to be large enough in order to adequately conclude correlations from the resulting matrix. Ideally, the parameters should be varied to produce more samples until the covariance cov_{ij} converges. In the case of the fit selection, there are only three samples besides the most optimal value of L_2, namely L_4, L_6 and the method of choosing the highest order in each energy bin based on χ^2_ν. Because the sample size is very small in this case the produced covariance and correlation matrices only give an idea of how the energy bins are correlated. In the case of fission fragment identification using a track energy selection cut a larger sampling size can be considered. The selection cut

can be placed at values larger or smaller than the most optimal value almost arbitrarily up to limits defined by physic reasons, namely obviously including alpha particles into the analysis or cutting out a large number of known fission fragments. Values close to the most optimal selection cut are expected to give a more accurate result than values closer to the limits. To avoid relying too heavily on the more unrealistic selection cuts far from the optimal value, more samples have been chosen near the most optimal value. As it is not feasible in this particular study to sample from a very large number of selection cuts, it is useful to consider the evolution of the standard deviation σ_i in any energy bin i, which should also converge with the number of samples:

$$\sigma_i = \sqrt{cov_{ii}} = \sqrt{\frac{1}{k}\sum_k (a_i^k - \langle a_i \rangle)(a_i^k - \langle a_i \rangle)}. \tag{5.44}$$

Figure 5.20 shows how the standard deviation seems to converge sufficiently in most energy bins with an increase to ten samples, which is then used to compute the resulting covariance and correlation matrix for the fission fragment identification as shown in the following chapter. Note that for the uncertainty calculation as described in section 5.7.3 the largest positive and negative values of σ_i in each energy bin are used.

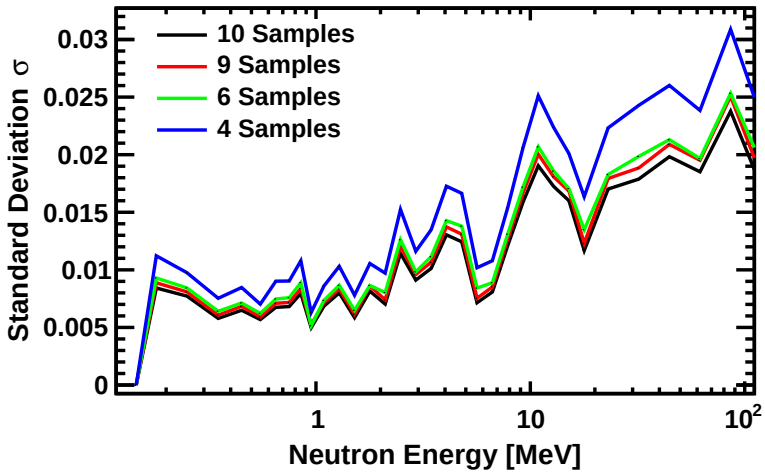

Figure 5.20: The standard deviation σ in each energy bin seems to converge sufficiently with an increasing number of samples between the most extreme track energy selection cut limits.

Chapter 6

Results and Discussion

This chapter presents the fission fragment anisotropy result for ^{235}U(n,f) over neutron energies from 160 keV to 230 MeV. While the anisotropy parameter represents a valuable tool for identifying overall trends and comparing to previous work, the complete angular distributions need to be considered for detailed study of the fission process. The interested reader can find the fitted angular distributions for each energy bin in appendix C. The following sections also present the results of the uncertainty study previously described in chapter 5.7, which detail the components of the total uncertainty band seen in the anisotropy result.

6.1 Anisotropy Result

Figure 6.1 shows the fission fragment anisotropy result, defined as the emission in beam direction over emission perpendicular to beam $A = W[0°]/W[90°]$, for neutron-induced fission of ^{235}U over neutron energies from 160 keV to 230 MeV. Appendix A contains a table with the numerical result in ENDF format. The result is shown in figure 6.1 in comparison with the two most comprehensive

data sets introduced in chapter 3 [44, 46], as available in the EXFOR library. As mentioned already, the present measurement differs from those in the literature primarily by the choice of neutron source. All previous experiments shown in EXFOR have been carried out using mono-energetic neutron sources, which makes coverage of a large energy range more difficult. The current result constitutes one of the first data sets providing continuous data for the medium to high neutron energy regime. When comparing the present data to literature, one has to note that the first depicted neutron energy bin from 130 to 160 keV was used for normalization and cannot be considered a measured data point, as discussed in detail in section 5.6.1. The result needs to be interpreted with respect to the normalization to an anisotropy value of 1 of the first neutron energy bin (see section 5.7.7).

Certain characteristic trends can be identified in the overall shape of the anisotropy curve: The anisotropy is assumed to be isotropic for very low neutron energies, but is seen to increase steadily to about 2 MeV. From 2 to 5 MeV the curve seems to flatten and eventually decline towards the second chance fission threshold. The threshold for second chance fission (the emission of a neutron before fission) at ∼6 MeV sees a sharp increase in anisotropic emission. The region between 6 and 14 MeV exhibits a dip and another sharp rise just before 14 MeV and the third chance fission threshold. From 14 MeV to several hundred MeV a steady decline in anisotropy is observed. The current result differs from the literature data in several regions. The dip in anisotropy just before the sharp rise at 6 MeV is not observed in the old data. That dip brings the anisotropy to about 5 % lower than the literature, which carries through to the region between 7 and 10 MeV and the 14 MeV point. One should note that a different normalization than the normalization to 1 would change that difference to the literature as well. There is an uncertainty associated with assuming the

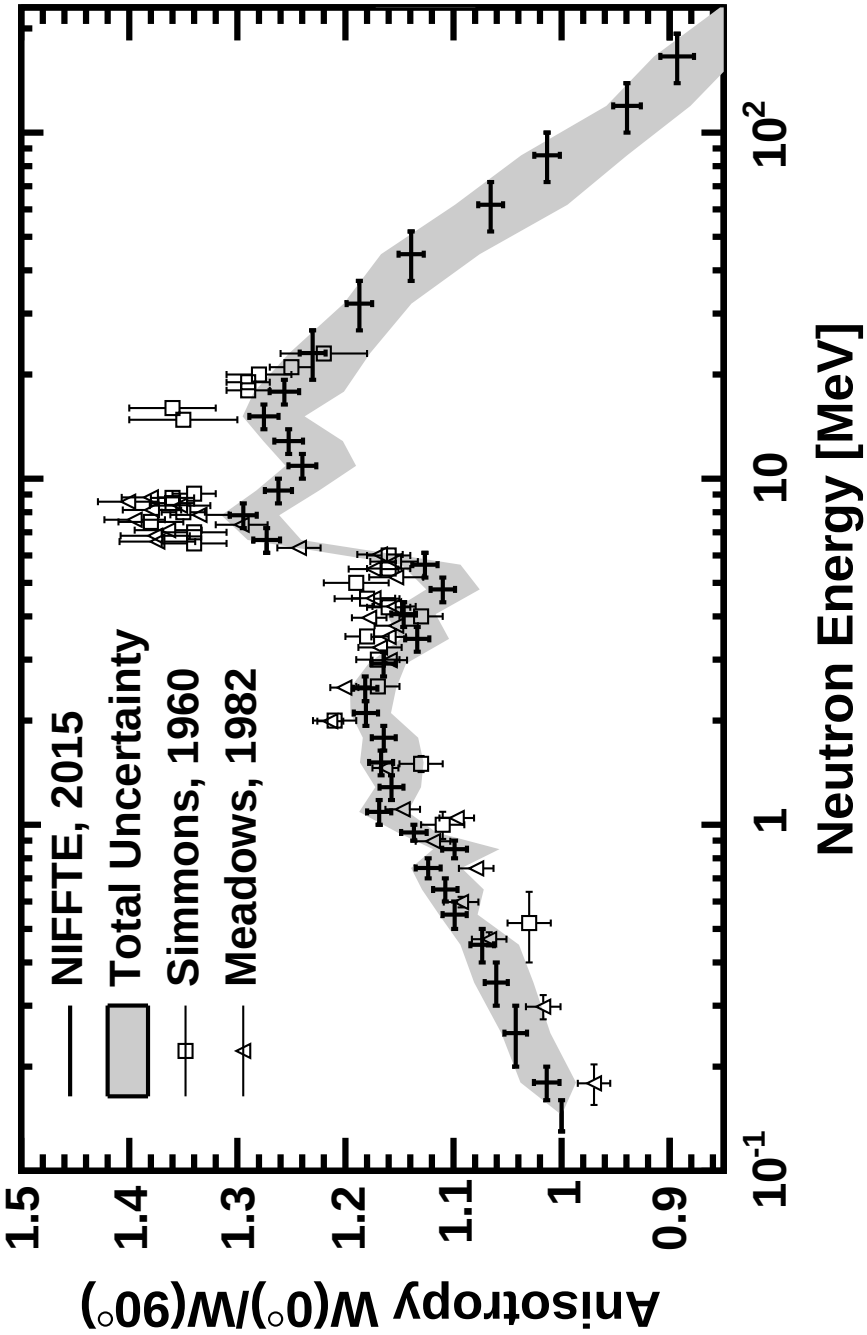

Figure 6.1: The fission fragment anisotropy over neutron energy for the neutron-induced fission of ^{235}U compared to the two most comprehensive data sets available in the literature [44, 46].

normalization point to be 1. If one chose a lower anisotropy value, like it might be suggested by the trend of the Meadows data, the result would scale to higher values for all points greater than 1 by the same percentage. The overall shape of the result, however, agrees well with the previous work.

Figure 6.2 shows that the result follows the neutron-induced fission cross section of ^{235}U very closely between 1 and 20 MeV, even more so than the previous data. The result especially mimics the step-like structure in the cross section, which is due to multi-chance fission. Note the sharp rises at 6 and 13 MeV. Multi-chance fission constitutes a major contribution to the neutron-

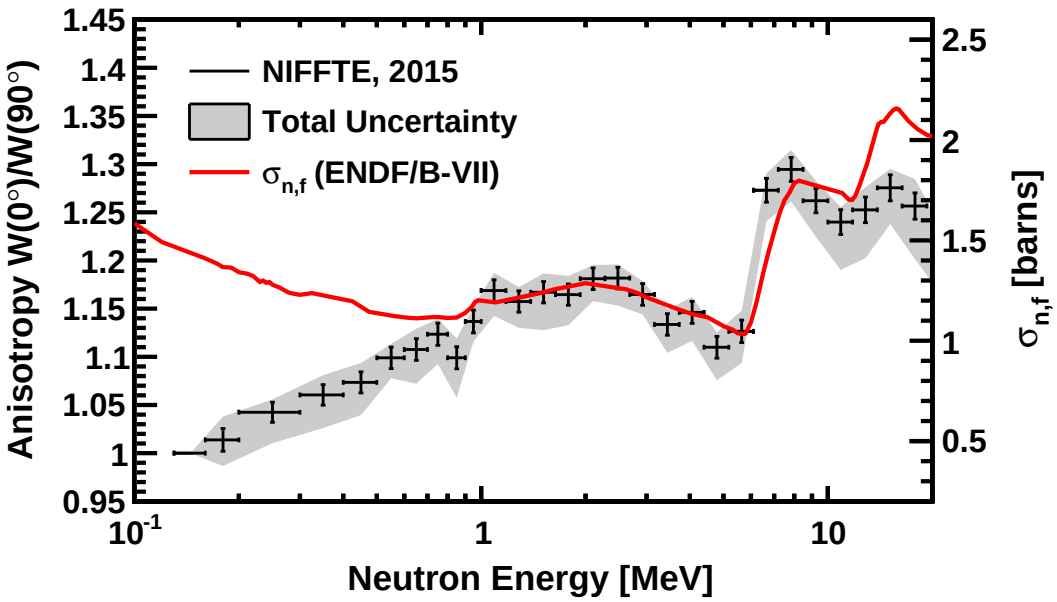

Figure 6.2: The fission fragment anisotropy for the neutron-induced fission of ^{235}U from 0 to 20 MeV compared to the neutron-induced fission cross section of ^{235}U, taken from ENDF/B-VII.

induced fission cross section of ^{235}U. As already mentioned, multi-chance fission denotes the process of emission of one or more neutrons before the compound

nucleus scissions. Figure 6.3 shows the different chance fission probabilities in percent of the total fission cross section. The calculations presented here were produced for a fission yield measurement [81] using the GEF code [82]. One can see that at higher neutron energies, the transition compound nucleus that undergoes fission is not always ^{236}U, but can be ^{235}U in the case of second chance fission, ^{234}U for third chance fission, and so on. Note that the probabilities of multi-chance fission do not add up to one hundred percent at higher energies, as also protons and light particles can be emitted, which is taken into account in GEF. One can see in figure 6.3 that the ^{235}U(n,f) reaction is only a small

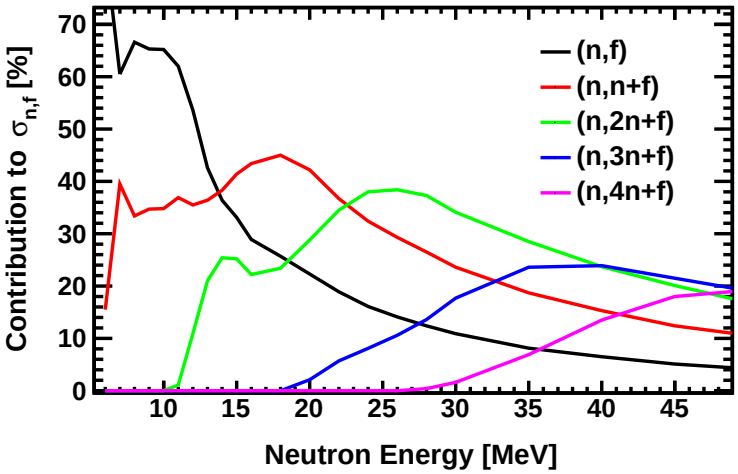

Figure 6.3: The contributions of several multi-chance components to the overall fission cross section of ^{235}U(n,f) as calculated in GEF.

fraction of reactions producing fission fragments at higher incident neutron energies, which makes theoretical predictions of all fission observables including fission fragment angular distributions difficult. If the experiment was able to distinguish between different channels of multi-chance fission, one would observe different anisotropies for each channel at a given neutron energy, as opposed to

seeing a superposition of channels. A few phenomenological deductions, however, can be made based on the statistical theory introduced in chapter 2.2: One of the characteristic properties of the transition nucleus in the statistical saddle point model is its thermodynamical temperature, the energy available to populate different level states. In a simplified picture the fissioning nucleus will exhibit anisotropic emission when it is thermodynamically cold and only very few energy levels are populated. If the available energy increases, more states are populated and the emission becomes more isotropic. This concept can, in principle, explain some of the structure in the anisotropy curve with neutron energy. It seems reasonable that the anisotropy would exhibit a plateau or even decrease with higher energy until a neutron is emitted which carries away excitation energy, when the now thermodynamically colder nucleus populates fewer states and exhibits a sharp rise an anisotropy. The concept explains the slow decline before and then the sharp increase in anisotropy at the multi-chance fission thresholds at $\sim$6 and $\sim$13 MeV.

With similar arguments derived from the statistical model one would expect the anisotropy to go towards 1 at even higher energies. As mentioned earlier, it is difficult to make any predictions though, when higher orders of multi-chance fission and additional proton and light particle emissions complicate the system, a large number of transition nuclei contribute to the final result. Preliminary results at higher energies from n_TOF and GNEIS [48, 49] do not give much more information as uncertainties in those results are large. Both new data sets also indicate a steady decline of anisotropy towards higher neutron energies, but while the n_TOF data seems to approach 1, the GNEIS data goes below 1 similarly to the result obtained in this study.

6.2 Uncertainties and Correlations

The anisotropy result in figure 6.1 shows the data points with statistical error bars obtained from the fitting procedure as described in section 5.7.1. The errors shown in neutron energy are actually the bin width of the result. The binning is linear below 1 MeV, the logarithmic binning at higher energies has a variable number of bins per decade. The bin width was chosen to be larger than the neutron energy uncertainty derived from the neutron time of flight calibration (see 5.3 and 5.7.4). The uncertainty band drawn in gray shade and labeled 'Total Uncertainty' contains both the statistical errors plus all systematic uncertainties, as described in section 5.7. Figure 6.4 shows the result of the uncertainty study with the individual contributions of all considered uncertainties. A detailed numerical table of the most important uncertainties can be found in appendix B. One can see that the statistical uncertainty is relatively constant at 1 %, which shows that the binning was chosen optimally. The uncertainties introduced with the linear momentum transfer and the wrap-around correction are minimal, while uncertainties related to tracking - the fit range and the drift speed selection - are in the 1 % range. The most significant uncertainties in the current result are attributed to the track energy cut which constitutes the particle identification in this study and the selection of the order of expansion into Legendre polynomials for the angular distribution fit; both uncertainties are in the 3 to 5 % range. Choosing the highest order of fit polynomial introduces a large uncertainty, which reflects the limited information content in the data. Some authors chose a highest order of 2 or 4, while Simmons chose to vary the highest order based on goodness of fit in each bin, which interestingly makes his statistical uncertainties non-continuous between neutron energy bins. The current result features a highest order of fit of 2, but included all options as a systematic uncertainty (see 5.7.8). It should also be noted that the errors shown in figure 6.1 by

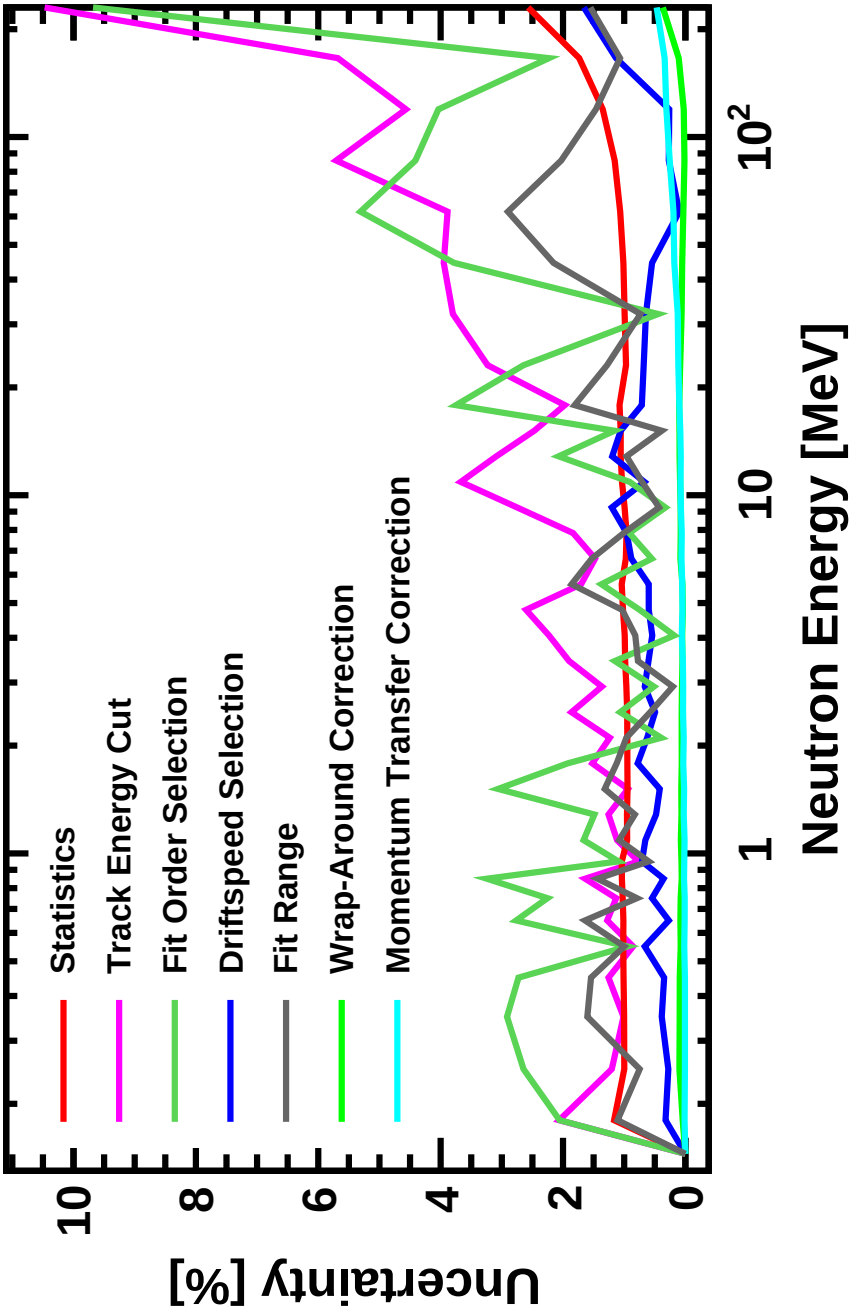

Figure 6.4: The individual uncertainty terms considered in the uncertainty study of the anisotropy result, given in percent of the anisotropy result.

Meadows are statistical only, while Simmons included some of his corrections but mentioned the uncertainty was dominated by statistics also.

At present the angular distributions or the anisotropy are not included in any of the evaluated nuclear data files. Due to demand by novel nuclear technologies their inclusion can, however, be expected in the future. One important tool for evaluators to understand uncertainties and compare different data sets and models are covariances and correlations. As already described in 5.8 the different uncertainties in this study are assumed to be uncorrelated. The uncertainties themselves, however, are correlated between neutron energy bins, unlike statistical uncertainties. The correlation can be understood in simple terms by describing it as the effect a small change in uncertainty in one energy bin would have on the uncertainty in a different bin. As a reminder: A correlation value of 1 means fully correlated - a positive change results in a positive change of the same magnitude, while -1 means fully anti-correlated - a positive change results in a negative change of the same magnitude. Correlation matrices were produced in this study only for the two largest sources of uncertainty. Figure 6.5 shows the correlation matrix for the track energy selection, while figure 6.6 shows the correlation matrix for the fit order selection. One should note that the sample size for the matrix was limited in both cases as described in section 5.8. It is interesting to see a strong variation in the correlation for the fit selection at the threshold for second chance fission where the anisotropy changes rapidly, while the uncertainty seen in figure 6.4 stays relatively constant. The track energy selection correlation seems to be much smoother overall.

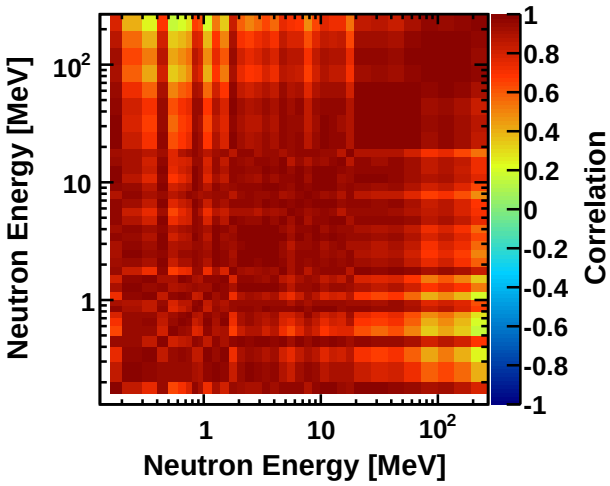

Figure 6.5: The correlation matrix in neutron energy for the track energy selection. Ten sample values around the optimal selection cut were used to compute the matrix.

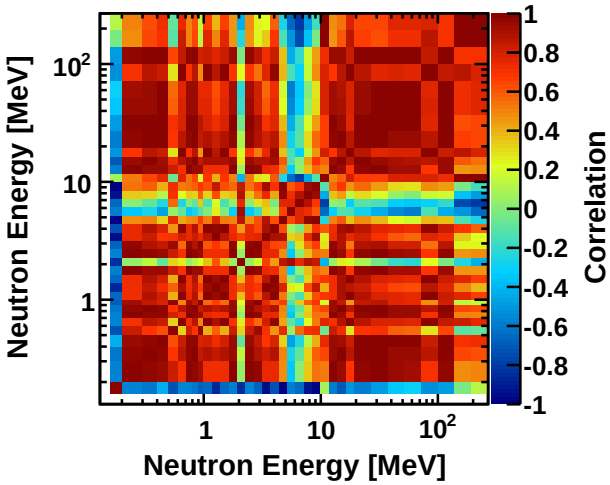

Figure 6.6: The correlation matrix in neutron energy for the fit order selection. While the anisotropy result was determined from quadratic fits, fitting with highest order of four and six plus a variation were used to compute the matrix.

Chapter 7

Conclusions

Fission fragment angular distributions and anisotropy values for neutron-induced fission of ^{235}U are provided in this thesis over a wide incident neutron energy range from 160 keV to 230 MeV. In the current study, fission fragment angular distributions were determined from three-dimensional tracking of charged particles in the newly developed fissionTPC instrument, a custom-built time projection chamber for the detailed investigation of the process of nuclear fission. It should be noted that the presented anisotropy data constitute the first physics result obtained with the novel detector.

The fission fragments were selected based on a simple energy threshold in this first analysis; the fissionTPC, however, is capable of more advanced particle identification for future studies. The geometrical efficiency of the detector was corrected by normalizing all angular distributions in all energy bins to the distribution in the first energy bin from 130 to 160 keV, which was assumed to exhibit a flat angular distribution - an anisotropy of 1. The normalization is not arbitrary though, as fission is isotropic for thermal incident neutron energies and theoretical work seems to indicate that for very low neutron energies it would almost be as well. The angular distributions were then fit over the full 2π

range with Legendre polynomials of quadratic order and the anisotropy value - emission in beam direction over emission perpendicular to beam $W[0°]/W[90°]$ - extracted.

The anisotropy result presented agrees well with previous measurements. Available literature data are, however, relatively sparse. The two most comprehensive data sets are by Simmons and Meadows [44, 46], which cover neutron energies from 0 to 9 MeV and 14 to 23 MeV. The measurements found in the EXFOR database were all carried out with mono-energetic neutron sources, which makes studying a large incident energy range difficult. The current result marks one of the first continuous measurements of a wide energy range up to several hundred MeV. While the result generally agrees with the literature, it provides additional information on the structure of the anisotropy between 1 and 20 MeV. The anisotropy found in this study differs from the literature by about 5 % between 3 and 14 MeV, the anisotropy value is slightly lower than in previous measurements in this range. The overall shape trend is similar, but one characteristic seems to be more pronounced in the current result: It was found that the anisotropy follows the fission cross section closely in the energy range from 1 to 20 MeV. The current study showed a slight decline in anisotropy followed by a sharp rise at both thresholds for second and third chance fission. The result can be explained phenomenologically within the framework of the statistical theory of nuclear fission. When available excitation energy decreases through emission of a neutron, less energy levels are populated in the transition state and the angular distributions are more anisotropic. The same is true for regions where more energy becomes available to the nucleus, as is the case right before the threshold for multi-chance fission, more states are populated and the anisotropy declines.

Within the statistical theory framework one could assume that for high neu-

tron energies beyond 20 MeV to several hundred MeV the anisotropy would eventually approach 1 or isotropic emission. The current result does show a steady decline between 20 and over 200 MeV, but the anisotropy value eventually dips below 1. It is hard to tell whether that indicates a potential issue with the data, as theoretical predictions are difficult. As described in chapter 6.1 many different isotopes fission at those energies, due to multi-chance fission, and they all exhibit different characteristic angular distributions. There are two preliminary data sets available from other high energy neutron sources, from n_TOF and GNEIS [48, 49], that indicate the same decline towards 1, but while the n_TOF data set seems to only approach 1, the GNEIS data goes below 1 similar to the current result.

The measurement presented here does not only provide valuable data for simulations needed in all nuclear applications, it also aids in the further development of fission models, and has a direct application within the NIFFTE fission cross section campaign. As already mentioned, one goal of the NIFFTE project is to measure a precise ^{239}Pu(n,f)/^{235}U(n,f) ratio cross section. The measurement is complicated by different angular distributions for the two isotopes, which become important in the computation of the ratio due to geometrical efficiency effects in the detector. Together with a measurement for the ^{239}Pu(n,f) angular distributions, which is currently being analyzed, the efficiency effects can be properly corrected for with the current data set. In the future, measurements of ^{238}U(n,f) are also planned.

The ^{235}U(n,f) anisotropy shown here constitutes the first nuclear physics result from the fissionTPC, a completely novel detector for the field of nuclear fission. With its powerful three-dimensional tracking capability the fissionTPC is suitable for many future physics measurements. One could easily study the process of ternary fission, where the nucleus splits into two fragments plus a

lighter particle. Cross section measurements on a range of isotopes are being planned and the suitability for (n, alpha) reaction measurements is being investigated. The fissionTPC has proven to be a valuable tool for studying the fundamental science of nuclear fission and eventually decoding the mystery of this complicated quantum process.

Appendix A

Tabulated Anisotropy Result

This appendix displays the anisotropy result for neutron-induced fission of ^{235}U shown in figure 6.1 in a tabular form. The used column headings are customary in the EXFOR database. EN and EN-ERR denote the neutron energy and its error (corresponding to half the bin width), given in MeV. DATA is the anisotropy result and ERR-NEG, ERR-POS and ERR-STAT correspond to the total negative, total positive (the total uncertainty is asymmetric), and statistical error respectively, all dimensionless.

Table A.1: The ^{235}U(n,f) anisotropy result as shown in figure 6.1.

EN	**EN-ERR**	**DATA**	**ERR-NEG**	**ERR-POS**	**ERR-STAT**
MEV	**MEV**	**NO-DIM**	**NO-DIM**	**NO-DIM**	**NO-DIM**
0.145	0.015	1	0	0	0
0.18	0.02	1.014	0.027	0.024	0.012
0.25	0.05	1.042	0.032	0.013	0.010
0.35	0.05	1.060	0.034	0.020	0.011
0.45	0.05	1.073	0.034	0.020	0.011

Continued on next page

Table A.1 – *Continued from previous page*

EN MEV	EN-ERR MEV	DATA NO-DIM	ERR-NEG NO-DIM	ERR-POS NO-DIM	ERR-STAT NO-DIM
0.55	0.05	1.099	0.021	0.014	0.011
0.65	0.05	1.108	0.036	0.022	0.011
0.75	0.05	1.123	0.031	0.016	0.012
0.85	0.05	1.099	0.042	0.020	0.012
0.95	0.05	1.137	0.021	0.015	0.012
1.09	0.09	1.169	0.026	0.019	0.011
1.28	0.11	1.157	0.027	0.015	0.011
1.51	0.12	1.167	0.039	0.020	0.011
1.78	0.15	1.165	0.032	0.019	0.011
2.10	0.17	1.181	0.023	0.014	0.011
2.48	0.20	1.182	0.029	0.014	0.011
2.92	0.24	1.165	0.021	0.014	0.011
3.44	0.28	1.134	0.029	0.015	0.011
4.06	0.33	1.146	0.030	0.016	0.011
4.79	0.39	1.110	0.034	0.015	0.011
5.64	0.46	1.126	0.033	0.022	0.012
6.65	0.55	1.273	0.032	0.018	0.012
7.84	0.64	1.294	0.033	0.020	0.012
9.24	0.76	1.262	0.038	0.020	0.013
10.89	0.89	1.240	0.050	0.016	0.013
12.84	1.05	1.253	0.050	0.023	0.013
15.14	1.24	1.275	0.038	0.020	0.014
17.84	1.46	1.256	0.055	0.028	0.014

Continued on next page

Table A.1 – *Continued from previous page*

EN	**EN-ERR**	**DATA**	**ERR-NEG**	**ERR-POS**	**ERR-STAT**
MEV	**MEV**	**NO-DIM**	**NO-DIM**	**NO-DIM**	**NO-DIM**
23.07	3.76	1.230	0.053	0.022	0.012
32.05	5.22	1.187	0.048	0.015	0.012
44.54	7.26	1.139	0.063	0.028	0.012
61.88	10.09	1.066	0.071	0.033	0.012
85.98	14.02	1.013	0.074	0.024	0.012
119.48	19.47	0.939	0.059	0.019	0.013
166.01	27.06	0.893	0.057	0.021	0.016
230.67	37.60	0.820	0.120	0.033	0.022

Appendix B

Uncertainty Contributions

The table below shows the contribution of the four largest systematic uncertainties to the anisotropy result as detailed in sections 5.7 and 6.2. The uncertainties considered are the track energy cut, the fit order selection, the fit range and the drift speed selection. The contributions are given in percent of the anisotropy value for each neutron energy bin EN in MeV. As described in section 5.7, the systematic uncertainties are largely asymmetric and exhibit a positive and a negative error. The uncertainty values shown here and in figure 6.4 are the absolute maximum in each bin, whether negative or positive.

Table B.1: The contribution of the four largest systematic uncertainties (track energy cut, fit order selection, fit range and drift speed) to the ^{235}U(n,f) anisotropy result in percent in each neutron energy bin as shown in figure 6.4.

EN	**Track Energy**	**Fit Order**	**Fit Range**	**Drift Speed**
MEV	**%**	**%**	**%**	**%**
0.18	2.06	2.06	1.11	0.32
0.25	1.20	2.65	0.75	0.28

Continued on next page

Table B.1 – *Continued from previous page*

EN	**Track Energy**	**Fit Order**	**Fit Range**	**Drift Speed**
MEV	**%**	**%**	**%**	**%**
0.35	1.01	2.92	1.60	0.39
0.45	1.26	2.73	1.54	0.35
0.55	0.85	0.95	1.00	0.66
0.65	1.28	2.77	1.64	0.27
0.75	1.13	2.25	0.79	0.55
0.85	1.64	3.25	1.44	0.36
0.95	0.77	1.09	0.60	0.71
1.09	1.12	1.66	1.08	0.65
1.28	1.26	1.49	0.83	0.48
1.51	0.94	3.06	1.32	0.42
1.78	1.52	1.92	1.12	0.78
2.10	1.24	0.39	0.97	0.62
2.48	1.86	1.07	0.57	0.50
2.92	1.36	0.51	0.20	0.66
3.44	1.90	1.15	0.78	0.60
4.06	2.23	0.18	0.82	0.54
4.79	2.60	0.75	1.03	0.60
5.64	1.70	1.37	1.86	0.60
6.65	1.48	0.55	1.53	0.88
7.84	1.83	0.92	1.01	0.96
9.24	2.75	0.33	0.43	1.20
10.89	3.67	0.91	0.71	0.67
12.84	3.09	2.07	0.96	1.20

Continued on next page

Table B.1 – *Continued from previous page*

EN	**Track Energy**	**Fit Order**	**Fit Range**	**Drift Speed**
MEV	**%**	**%**	**%**	**%**
15.14	2.47	1.16	0.39	1.06
17.84	1.97	3.75	1.81	0.71
23.07	3.23	2.65	1.28	0.68
32.05	3.80	0.44	0.73	0.64
44.54	3.95	3.78	2.16	0.54
61.88	3.89	5.31	2.90	0.10
85.98	5.71	4.41	2.03	0.27
119.48	4.57	4.04	1.46	0.26
166.01	5.68	2.23	1.07	1.13
230.67	10.52	9.75	1.56	1.66

Appendix C

Angular Distributions

The following section contains the individual angular distributions for neutron-induced fission of ^{235}U in all neutron energy bins. The distributions are fitted with Legendre polynomials of quadratic order. The fit equations are shown as well as the goodness of fit parameters reduced chi-square χ^2_ν. Note that the value in the fit equation is not immediately the anisotropy, as small wrap-around corrections change the value by up to 0.75 %. The distributions are binned into 20 angular bins each, the x-error shown corresponds to the bin width, while the y-error reflects counting statistics in each bin.

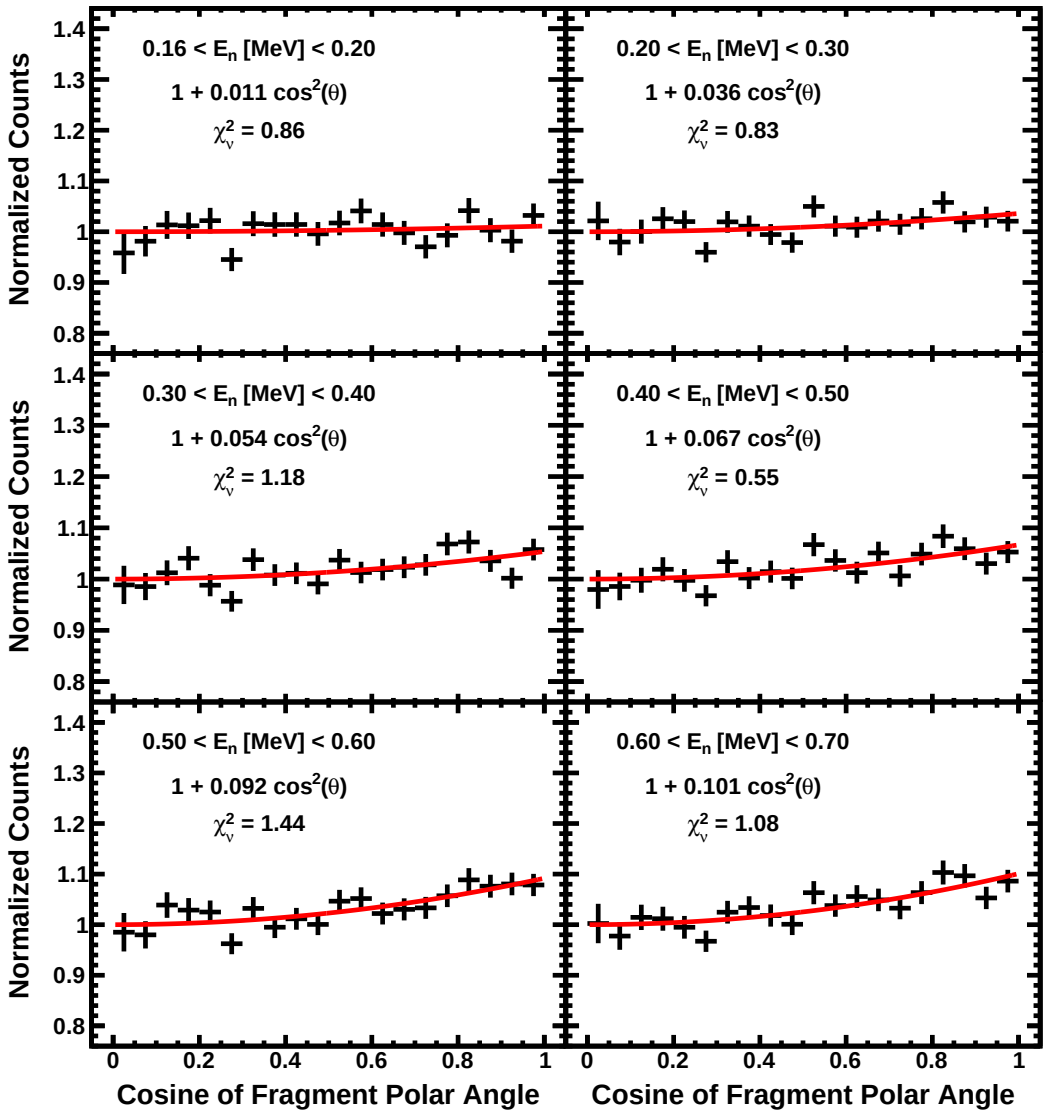

Figure C.1: The ^{235}U(n,f) angular distributions for incident neutron energies from 160 keV to 700 keV.

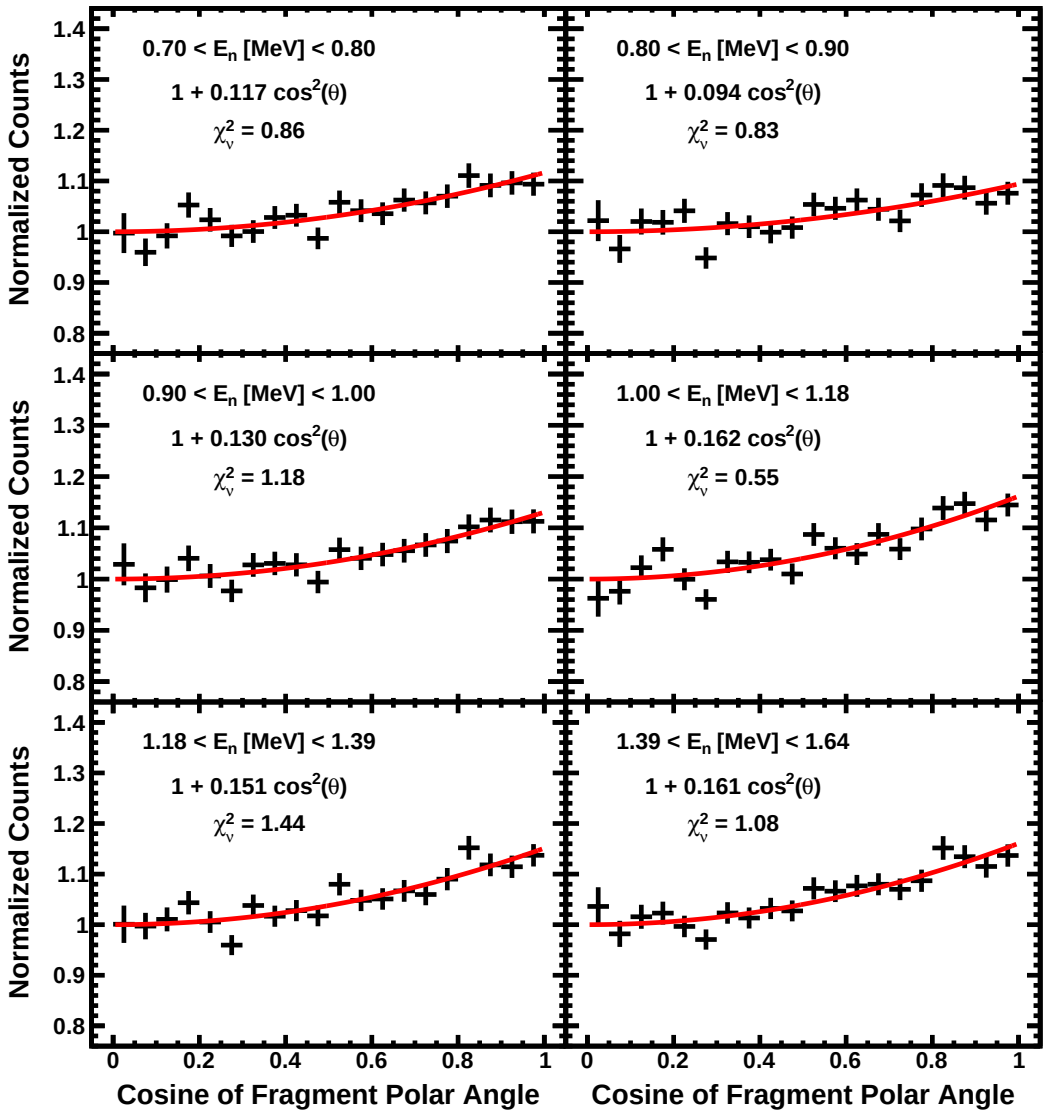

Figure C.2: The ^{235}U(n,f) angular distributions for incident neutron energies from 700 keV to 1.64 MeV.

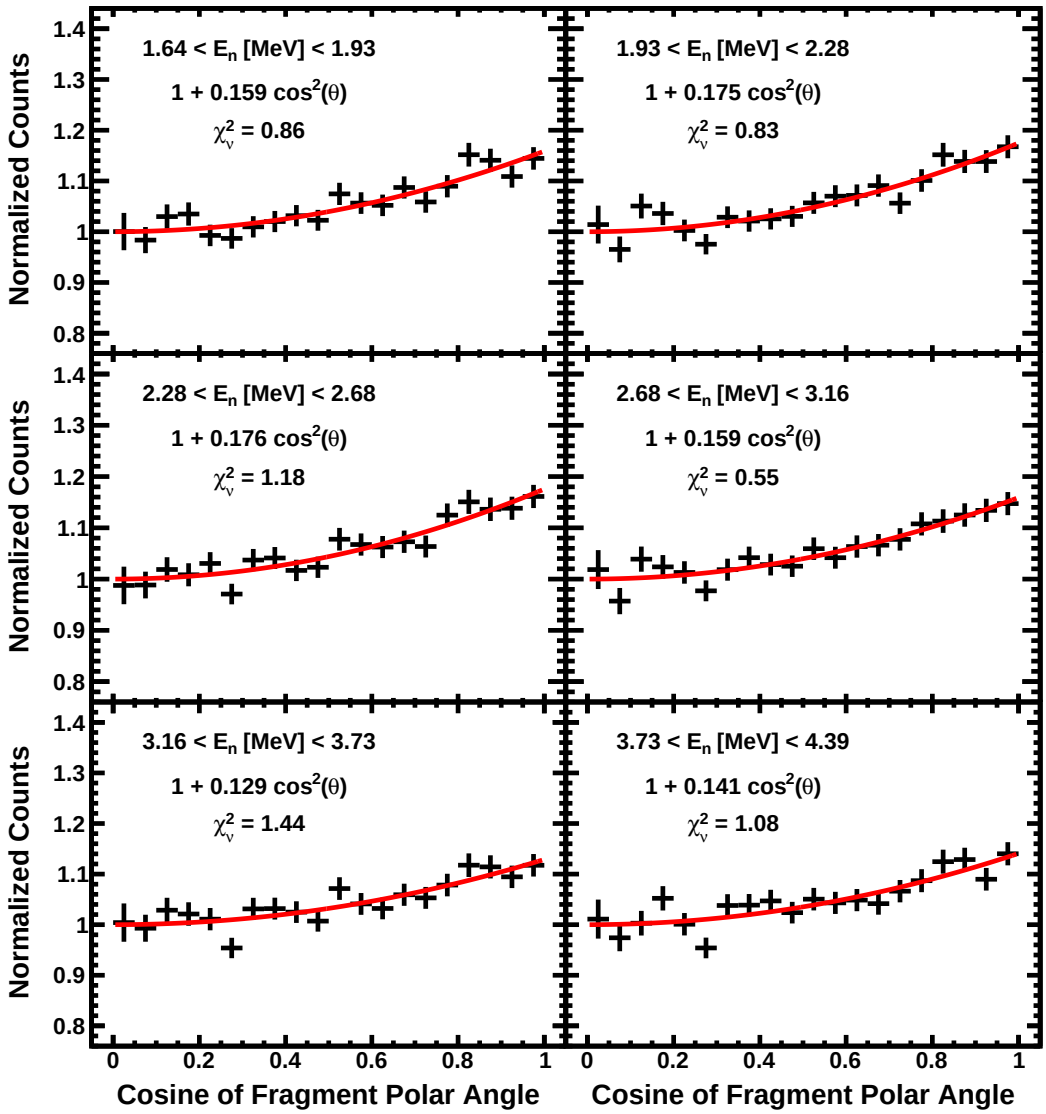

Figure C.3: The ^{235}U(n,f) angular distributions for incident neutron energies from 1.64 to 4.39 MeV.

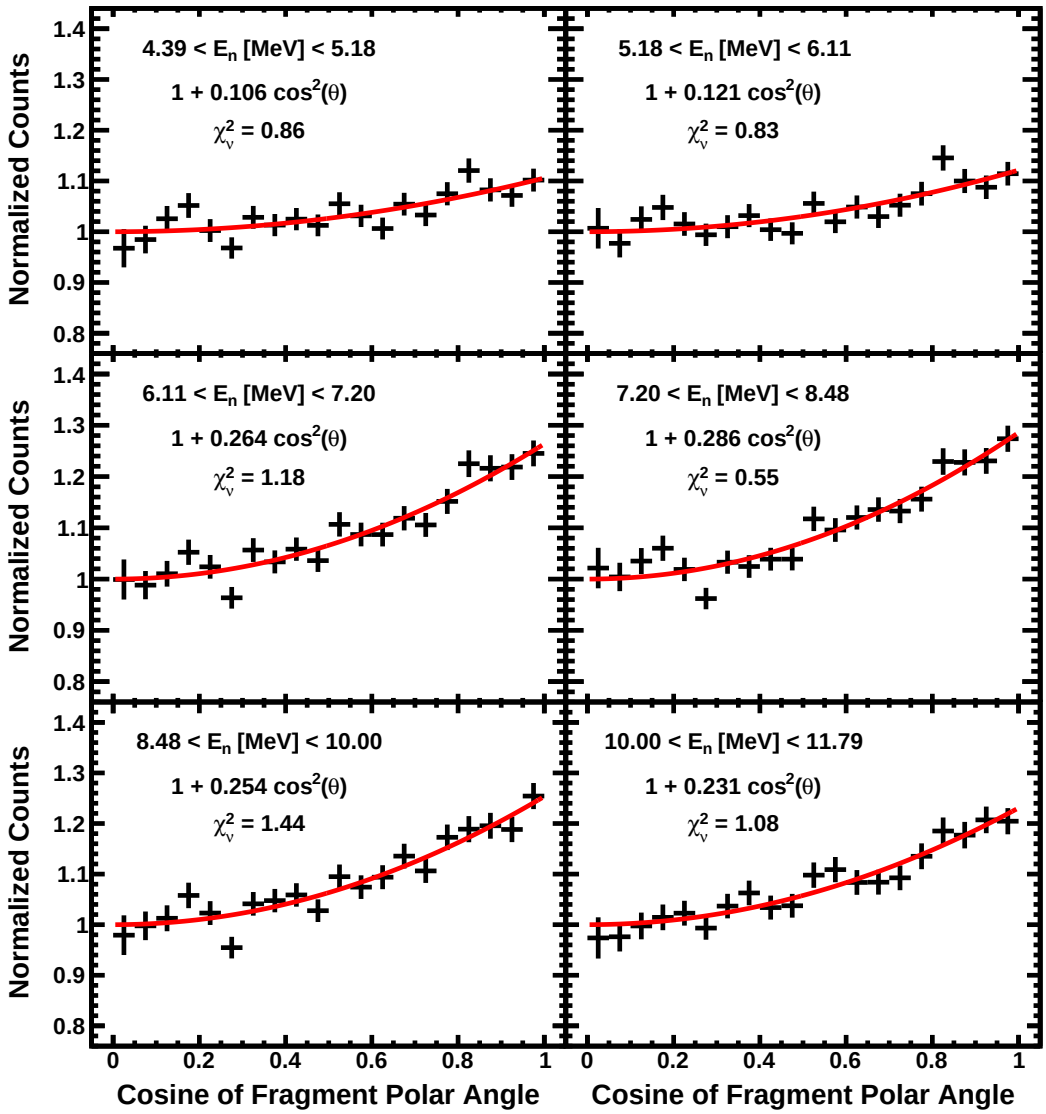

Figure C.4: The ^{235}U(n,f) angular distributions for incident neutron energies from 4.39 to 11.79 MeV.

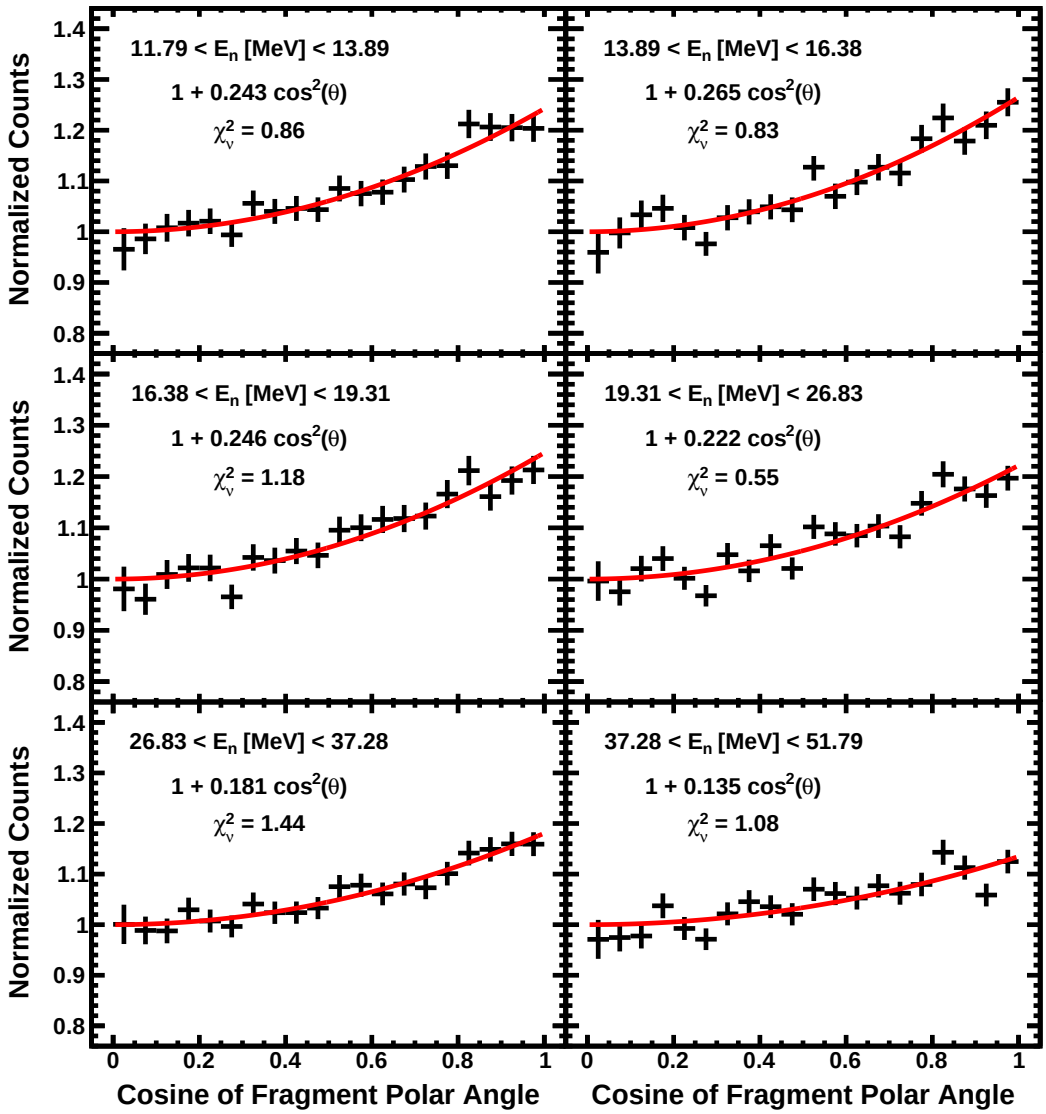

Figure C.5: The ^{235}U(n,f) angular distributions for incident neutron energies from 11.79 to 51.79 MeV.

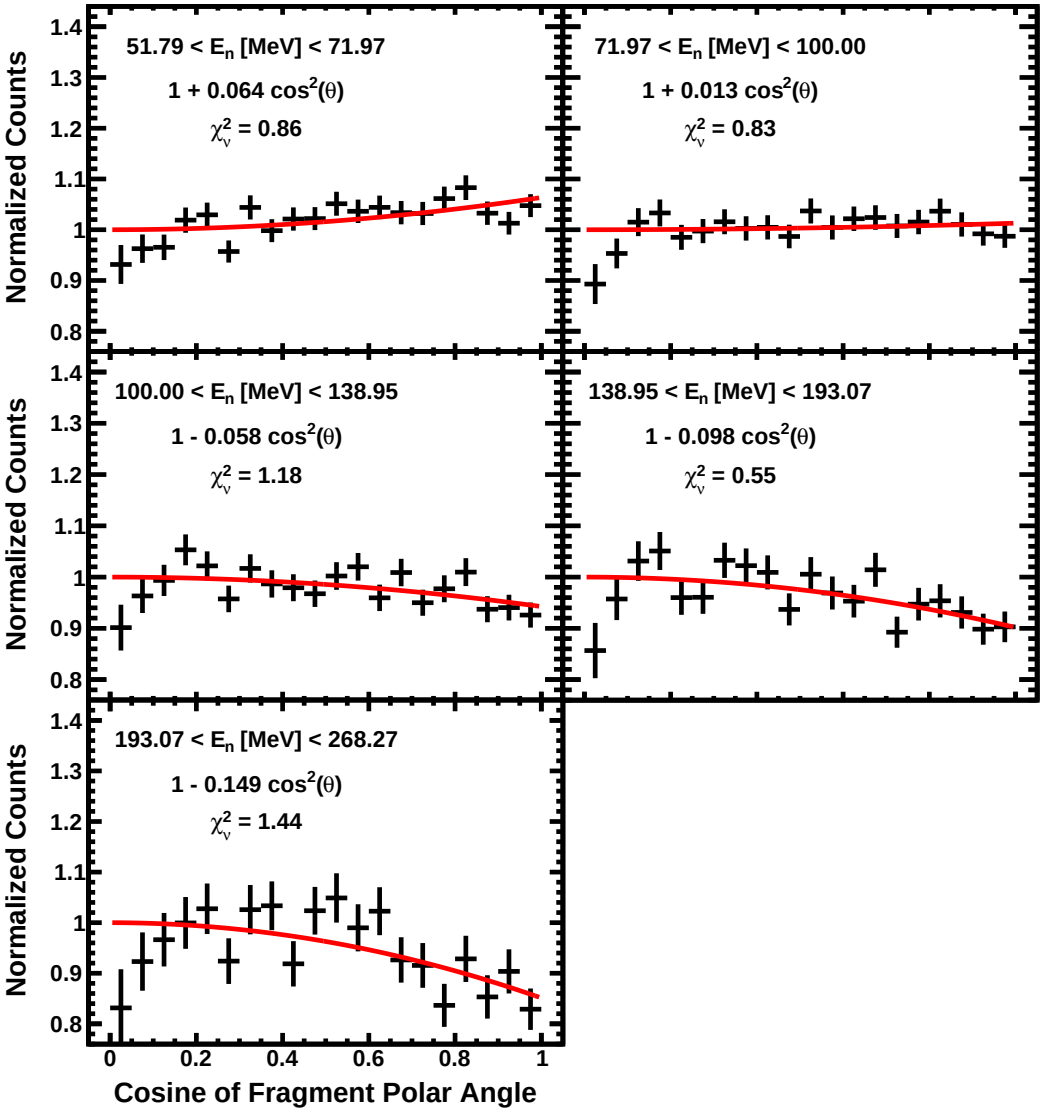

Figure C.6: The ^{235}U(n,f) angular distributions for incident neutron energies from 51.79 to 268.27 MeV.

Bibliography

[1] N. Otsuka, E. Dupont, V. Semkova, *et al.*, "Towards a More Complete and Accurate Experimental Nuclear Reaction Data Library (EXFOR): International Collaboration Between Nuclear Reaction Data Centres (NRDC)," *Nuclear Data Sheets*, vol. 120, pp. 272 – 276, 2014.

[2] M. Chadwick, M. Herman, P. Obložinský, *et al.*, "ENDF/B-VII.1 Nuclear Data for Science and Technology: Cross Sections, Covariances, Fission Product Yields and Decay Data," *Nuclear Data Sheets*, vol. 112, pp. 2887–2996, Dec. 2011.

[3] A. Santamarina, D. Bernard, P. Blaise, *et al.*, "The JEFF-3.1.1 nuclear data library," Tech. Rep. 10.2, 2009.

[4] K. Shibata, O. Iwamoto, T. Nakagawa, *et al.*, "JENDL-4.0: A New Library for Nuclear Science and Engineering," *Journal of Nuclear Science and Technology*, vol. 48, no. 1, pp. 1–30, 2011.

[5] M. B. Chadwick, "Future Challenges for Nuclear Data Research in Fission," *Journal of the Korean Physical Society*, vol. 59, p. 752, Aug 2011.

[6] P. Salvador-Castiñeira, T. Brys, R. Eykens, *et al.*, "Neutron-induced fission cross section of ^{240}Pu from 0.5 MeV to 3 MeV," *Physical Review C: Nuclear Physics*, vol. 92, p. 014620, Jul 2015.

[7] C. Paradela, M. Calviani, D. Tarrío, *et al.*, "High-accuracy determination of the ^{238}U/^{235}U fission cross section ratio up to $\approx$ 1 GeV at n_TOF at CERN," *Physical Review C: Nuclear Physics*, vol. 91, p. 024602, Feb 2015.

[8] A. Bohr, "On the Theory of Nuclear Fission," in *Proceedings of the International Conference on the Peaceful Uses of Atomic Energy*, vol. 2, (New York), pp. 151–154, United Nations, 1956.

[9] E. Winhold, P. Demos, and I. Halpern, "The angular distribution of fission fragments in the photofission of thorium," *Physical Review*, vol. 87, no. 6, p. 1139, 1952.

[10] W. Loveland, J. Huizenga, A. Behkami, and J. Roberts, "Identification of single-particle states in the fission transition nucleus ^{235}U," *Physics Letters B: Particle Physics, Nuclear Physics and Cosmology*, vol. 24, no. 13, pp. 666 – 668, 1967.

[11] A. N. Behkami, J. H. Roberts, W. Loveland, and J. R. Huizenga, "Structure of the Fission Transition Nucleus U235," *Physical Review*, vol. 171, pp. 1267–1277, Jul 1968.

[12] J. E. Lynn, "Fission in nuclear reaction theory," *Journal of Physics A: Mathematical, Nuclear and General*, vol. 6, no. 4, p. 542, 1973.

[13] O. Bouland, J. E. Lynn, and P. Talou, "R-matrix analysis and prediction of low-energy neutron-induced fission cross sections for a range of Pu isotopes," *Physical Review C: Nuclear Physics*, vol. 88, p. 054612, Nov 2013.

[14] O. Hahn and F. Strassmann, "Über den Nachweis und das Verhalten der bei der Bestrahlung des Urans mittels Neutronen entstehenden Erdalkalimetalle," *Die Naturwissenschaften*, vol. 27, pp. 11–15, Jan. 1939.

[15] L. Meitner and O. R. Frisch, "Disintegration of Uranium by Neutrons: A New Type of Nuclear Reaction," *Nature*, vol. 143, pp. 239–240, Jan. 1939.

[16] N. Bohr, "Disintegration of Heavy Nuclei," *Nature*, vol. 143, pp. 330–330, Feb. 1939.

[17] N. Bohr and J. A. Wheeler, "The Mechanism of Nuclear Fission," *Physical Review*, vol. 56, no. 5, pp. 426–450, 1939.

[18] O. R. Frisch, "Physical evidence for the division of heavy nuclei under neutron bombardment," *Nature*, vol. 143, no. 3616, pp. 276–276, 1939.

[19] K. S. Krane, *Introductory Nuclear Physics*. Wiley, 1987.

[20] S. Bjørnholm and J. E. Lynn, "The double-humped fission barrier," *Reviews of Modern Physics*, vol. 52, pp. 725–931, Oct 1980.

[21] M. Goeppert-Mayer, "On Closed Shells in Nuclei. II," *Physical Review*, vol. 75, pp. 1969–1970, June 1949.

[22] B. R. Mottelson and S. G. Nilsson, "Classification of the Nucleonic States in Deformed Nuclei," *Physical Review*, vol. 99, pp. 1615–1617, Sep 1955.

[23] S. Nilsson, "Binding states of individual nucleons in strongly deformed nuclei," *Kgl. Danske Videnskab. Selskab., Mat.-fys Medd.*, vol. Vol: 29, No. 16, Jan 1955.

[24] V. Strutinsky, "Shell effects in nuclear masses and deformation energies," *Nuclear Physics A: Nuclear and Hadronic Physics*, vol. 95, pp. 420–442, Apr. 1967.

[25] *McGraw-Hill Concise Encyclopedia of Physics.* Concise Encyclopedia Series, McGraw-Hill, 2002.

[26] J. R. Huizenga, "Nuclear Fission Revisited," *Science*, vol. 168, no. 3938, pp. 1405–1413, 1970.

[27] N. Bohr, "Neutron Capture and Nuclear Constitution," *Nature*, vol. 137, pp. 344–348, Feb. 1936.

[28] W. Hauser and H. Feshbach, "The Inelastic Scattering of Neutrons," *Physical Review*, vol. 87, pp. 366–373, Jul 1952.

[29] S. Hilaire, "Statistical nuclear reactions," in *Workshop on nuclear reaction data and nuclear reactors: Physics, design and safety; Trieste (Italy)* (N. Paver, M. Herman, and A. Gandini, eds.), pp. 105–119, 2000.

[30] R. Vandenbosch and J. Huizenga, *Nuclear Fission.* Academic Press, 1973.

[31] J. J. Griffin, "Transition States at the Fission Barrier," in *Proceedings of the Symposium on the Physics and Chemistry of Fission, Salzburg, Austria*, International Atomic Energy Agency (IAEA), 1965.

[32] C. Wagemans, *The Nuclear Fission Process.* CRC Press, 1991.

[33] F. Reiche, "Die Quantelung des symmetrischen Kreisels nach Schrödingers Undulationsmechanik," *Zeitschrift für Physik*, vol. 39, pp. 444–464, 1926.

[34] R. d. L. Kronig and I. I. Rabi, "The Symmetrical Top in the Undulatory Mechanics," *Physical Review*, vol. 29, pp. 262–269, Feb 1927.

[35] E. Wigner, *Gruppentheorie und ihre Anwendung auf die Quantenmechanik der Atomspektren.* Die Wissenschaft, Braunschweig: Vieweg Verlag, 1931.

[36] J. A. Wheeler, *Fast Neutron Physics*, ch. Channel Analysis of Fission. New York: Interscience, 1963.

[37] I. Halpern and V. Strutinski in *Proceedings of the Second International Conference on Peaceful Uses of Atomic Energy, Geneva*, vol. 15, (New York), p. 452, United Nations, 1958.

[38] P. Hodgson, *The Nucleon Optical Model.* World Scientific, 1994.

[39] R. L. Henkel and J. E. Brolley, "Angular Distribution of Fragments from Neutron-Induced Fission of U238 and Th232," *Physical Review*, vol. 103, pp. 1292 – 1295, Sep 1956.

[40] S. Nigro and C. Milone, "Angular distributions of fragments from 238U(n, f) reactions near the threshold," *Nuclear Physics A: Nuclear and Hadronic Physics*, vol. 151, pp. 182–186, Aug. 1970.

[41] H. Afarideh, S. Durrani, and K. Randle, "Angular distribution of fragments from the fission of 238U induced by neutrons in the energy range 1-18 MeV," *Annals of Nuclear Energy*, vol. 17, no. 3, pp. 143 – 151, 1990.

[42] A. Al-Adili, F.-J. Hambsch, S. Pomp, and S. Oberstedt, "Indication of anisotropic TKE and mass emission in 234U(n,f)," *Physics Procedia*, vol. 31, pp. 158–164, Jan. 2012.

[43] D. Tarrío, L. Leong, L. Audouin, *et al.*, "Measurement of the angular distribution of fission fragments using a PPAC assembly at CERN n_TOF," *Nuclear Instruments and Methods in Physics Research Section A: Accelerators, Spectrometers, Detectors and Associated Equipment*, vol. 743, pp. 79–85, Apr. 2014.

[44] J. E. Simmons and R. L. Henkel, "Angular Distribution of Fragments in Fission Induced by Mev Neutrons," *Physical Review*, vol. 120, pp. 198–210, Oct. 1960.

[45] J. Meadows and C. Budtz-Jørgensen, "The Fission Fragment Angular Distributions and Total Kinetic Energies for 235U(n,f) from 0.18 to 8.83 MeV," Tech. Rep. ANL/NDM-64, Argonne National Laboratory, 1982.

[46] J. Meadows and C. Budtz-Jørgensen, "Fission Fragment Angular Distributions and Total Kinetic Energies for 235U(n,f) from 0.18 to 8.83 MeV," in *Nuclear Data for Science and Technology* (K. Bčkhoff, ed.), pp. 740–743, Springer Netherlands, 1983.

[47] D. Tarrío, L. Leong, L. Audouin, *et al.*, "Fission Fragment Angular Distribution of 232Th(n,f) at the CERN n_TOF Facility," *Nuclear Data Sheets*, vol. 119, pp. 35 – 37, 2014.

[48] L. S. Leong, *Fission fragment angular distribution and fission cross section validation.* PhD thesis, Université Paris Sud - Paris XI, Sept. 2013.

[49] A. Vorobyev, A. Gagarski, O. Shcherbakov, L. Vaishnene, and A. Barabanov, "Anisotropy of the fission fragments from neutron-induced fission

in the intermediate energy range of 1-200 MeV," *JETP Letters*, vol. 102, no. 4, pp. 203–206, 2015.

[50] N. Abrosimov, G. Borukhovich, A. Laptev, *et al.*, "Neutron time-of-flight spectrometer GNEIS at the Gatchina 1 GeV proton synchrocyclotron," *Nuclear Instruments and Methods in Physics Research Section A: Accelerators, Spectrometers, Detectors and Associated Equipment*, vol. 242, no. 1, pp. 121 – 133, 1985.

[51] G. F. Knoll, *Radiation Detection and Measurement.* John Wiley & Sons, 2010.

[52] C. Budtz-Jørgensen, H.-H. Knitter, C. Straede, F.-J. Hambsch, and R. Vogt, "A twin ionization chamber for fission fragment detection," *Nuclear Instruments and Methods in Physics Research Section A: Accelerators, Spectrometers, Detectors and Associated Equipment*, vol. 258, pp. 209–220, Aug 1987.

[53] C. Straede, C. Budtz-Jørgensen, and H.-H. Knitter, "235U(n, f) Fragment mass-, kinetic energy- and angular distributions for incident neutron energies between thermal and 6 MeV," *Nuclear Physics A: Nuclear and Hadronic Physics*, vol. 462, no. 1, pp. 85 – 108, 1987.

[54] E. Birgersson, A. Oberstedt, S. Oberstedt, and F.-J. Hambsch, "Properties of the reaction 238U at the vibrational resonances," *Nuclear Physics A: Nuclear and Hadronic Physics*, vol. 817, no. 1 - 4, pp. 1 – 34, 2009.

[55] F. Vives, F.-J. Hambsch, H. Bax, and S. Oberstedt, "Investigation of the fission fragment properties of the reaction 238U(n,f) at incident neutron energies up to 5.8 MeV," *Nuclear Physics A: Nuclear and Hadronic Physics*, vol. 662, no. 1 - 2, pp. 63 – 92, 2000.

[56] H. J. Hilke, "Time projection chambers," *Reports on Progress in Physics*, vol. 73, no. 11, p. 116201, 2010.

[57] V. Lepeltier, "Review on TPC's," *Journal of Physics: Conference Series*, vol. 65, no. 1, p. 12001, 2007.

[58] J. N. Marx and D. R. Nygren, "The Time Projection Chamber," *Physics Today*, vol. 31, p. 46, Oct. 1978.

[59] M. Anderson, J. Berkovitz, W. Betts, *et al.*, "The STAR time projection chamber: a unique tool for studying high multiplicity events at RHIC," *Nuclear Instruments and Methods in Physics Research Section A: Accelerators,*

Spectrometers, Detectors and Associated Equipment, vol. 499, pp. 659–678, Mar. 2003.

[60] The STAR collaboration, "Observation of the antimatter helium-4 nucleus," *Nature*, vol. 473, pp. 353–6, May 2011.

[61] G. Charpak, J. Derré, Y. Giomataris, and P. Rebourgeard, "Micromegas, a multipurpose gaseous detector," *Nuclear Instruments and Methods in Physics Research Section A: Accelerators, Spectrometers, Detectors and Associated Equipment*, vol. 478, pp. 26–36, Feb. 2002.

[62] Y. Giomataris, P. Rebourgeard, J. Robert, and G. Charpak, "MICROMEGAS: a high-granularity position-sensitive gaseous detector for high particle-flux environments," *Nuclear Instruments and Methods in Physics Research Section A: Accelerators, Spectrometers, Detectors and Associated Equipment*, vol. 376, pp. 29–35, June 1996.

[63] M. Heffner, ..., V. Kleinrath, *et al.*, "A time projection chamber for high accuracy and precision fission cross-section measurements," *Nuclear Instruments and Methods in Physics Research Section A: Accelerators, Spectrometers, Detectors and Associated Equipment*, vol. 759, pp. 50 – 64, 2014.

[64] M. Heffner, V. Riot, and L. Fabris, "A Compact, Flexible, High Channel Count DAQ Built From Off-the-Shelf Components," *Nuclear Science, IEEE Transactions on*, vol. 60, pp. 2196–2202, June 2013.

[65] W. Loveland and J. Baker, "Target preparation for the fission TPC," *Journal of Radioanalytical and Nuclear Chemistry*, vol. 282, no. 2, pp. 361–363, 2009.

[66] W. Loveland, ..., V. Kleinrath, *et al.*, "Targets for Precision Measurements," *Nuclear Data Sheets*, vol. 119, pp. 383 – 385, 2014.

[67] S. Agostinelli, "GEANT4 - a simulation toolkit," *Nuclear Instruments and Methods in Physics Research Section A: Accelerators, Spectrometers, Detectors and Associated Equipment*, vol. 506, no. 3, pp. 250–303, 2003.

[68] R. Brun and F. Rademakers, "ROOT - an object oriented data analysis framework," *Nuclear Instruments and Methods in Physics Research Section A: Accelerators, Spectrometers, Detectors and Associated Equipment*, vol. 389, pp. 81–86, Apr. 1997.

[69] R. Mankel, "Pattern recognition and event reconstruction in particle physics experiments," *Reports on Progress in Physics*, vol. 67, no. 4, p. 553, 2004.

[70] P. V. Hough, "Machine analysis of bubble chamber pictures," in *International Conference on High Energy Accelerators and Instrumentation*, vol. 73, 1959.

[71] R. O. Duda and P. E. Hart, "Use of the Hough Transformation to Detect Lines and Curves in Pictures," *Communications of the ACM*, vol. 15, pp. 11–15, Jan. 1972.

[72] J. Illingworth and J. Kittler, "A survey of the hough transform," *Computer Vision, Graphics, and Image Processing*, vol. 44, pp. 87–116, Oct. 1988.

[73] R. E. Kalman, "A new approach to linear filtering and prediction problems," *Journal of Fluids Engineering*, vol. 82, no. 1, pp. 35–45, 1960.

[74] R. Frühwirth, "Application of Kalman filtering to track and vertex fitting," *Nuclear Instruments and Methods in Physics Research Section A: Accelerators, Spectrometers, Detectors and Associated Equipment*, vol. 262, no. 2 - 3, pp. 444 – 450, 1987.

[75] G. Welch and G. Bishop, "An Introduction to the Kalman Filter," *Design*, vol. 7, no. 1, pp. 1–16, 2001.

[76] P. W. Lisowski and K. F. Schoenberg, "The Los Alamos Neutron Science Center," *Nuclear Instruments and Methods in Physics Research Section A: Accelerators, Spectrometers, Detectors and Associated Equipment*, vol. 562, no. 2, pp. 910 – 914, 2006.

[77] P. Lisowski, C. Bowman, G. Russell, and S. Wender, "The Los Alamos National Laboratory spallation neutron sources," *Nuclear Science and Engineering*, vol. 106, no. 2, pp. 208–218, 1990.

[78] "LANSCE Nuclear Science User Guide," tech. rep., Los Alamos National Laboratory, 2011.

[79] E. Birgersson, *Determination of binary fission-fragment yields in the reaction 251Cf(nth, f) and Verification of nuclear reaction theory predictions of fission-fragment distributions in the reaction 238U(n, f)*. PhD thesis, Örebro University, 2007.

[80] S. Biagi, "A description of the Magboltz program, with results compared to experiment," *Nuclear Instruments and Methods in Physics Research Section A: Accelerators, Spectrometers, Detectors and Associated Equipment*, vol. 421, pp. 234–240, 1999.

[81] D. Duke, *Fission Fragment Mass Distributions and Total Kinetic Energy Release Of 235-Uranium and 238-Uranium in Neutron-induced Fission at Intermediate and Fast Neutron Energies.* PhD thesis, Colorado School of Mines, 2015.

[82] K.-H. Schmidt, B. Jurado, and C. Amouroux, "General description of fission observables: GEF model," JEFF Report, Nuclear Energy Agency, June 2014.

Verena Kleinrath

PhD Candidate in Nuclear Physics

Karajangasse 3/9
1200 Vienna, Austria
✉ *verena.kleinrath@gmail.com*
+43 677 612 60807

Education

2010 - 01/2016 **PhD in Nuclear Physics**, *Vienna University of Technology, Austria.*
Fission Fragment Angular Distributions in Neutron-Induced Fission of ^{235}U Measured with a Time Projection Chamber.
Advisors: Fredrik Tovesson (LANL), Helmut Leeb (Vienna UT).

2004 - 2010 **MSc in Technical Physics**, *Vienna University of Technology, Austria.*
A Study of Gamma Interference Scenarios for Nuclear Security Purposes.
Advisors: Helmuth Böck (Vienna UT), Rolf Arlt (IAEA).

2008 - 2009 **Technical Physics Graduate Coursework**, *Uppsala University, Sweden.*
Graduate courses in Technical Physics, funded through ERASMUS (European Community Action Scheme for the Mobility of University Students).

Schools and Workshops

09/2014 Los Alamos National Laboratory FIESTA Nuclear Fission School and Workshop. Santa Fe, USA.

11/2011 Theory and Practice of Criticality Calculations with MCNP5. Idaho National Laboratory, Idaho Falls, USA.

03/2010 6th ESARDA Course on Nuclear Safeguards and Non-Proliferation. European Commisssion, Institute for the Protection and Security of the Citizen, Ispra, Italy.

08/2009 Scientists Cooperate for Peace - Nuclear Issues Summer School. Carl Friedrich von Weizsäcker Center, Hamburg, Germany.

Experimental Skills

Time Projection Chambers	Ionization Chambers
Silicon Surface Barrier Detectors	Gamma Spectrometry
RadWorker II, Glovebox	Vacuum Technology
NIM Electronics	Digital Data Acquisition

Computing Skills

Languages	C++, C, Bash	**Data**	ROOT
Math	Mathematica	**Simulation**	MCNP, Geant4, SRIM
Networks	SSH, VPN	**Versioning**	SVN, Git

Research Experience

11/2015 - present **L'Oréal Austria For Women in Science Fellow**, *Vienna University of Technology*, Vienna, Austria.

- Completed and documented analysis on fission fragment angular distributions in neutron-induced fission of ^{235}U measured with the Neutron Induced Fission Fragment Experiment (NIFFTE) fission time projection chamber (fissionTPC).
- Prepared manuscript on fission fragment angular distributions for publication.

10/2012 - 10/2015 **Graduate Research Associate**, *Los Alamos National Laboratory, P-27 LANSCE Weapons Physics (previously LANSCE-NS Nuclear Science)*, Los Alamos, USA.

- Ran in-beam experiments with the NIFFTE fissionTPC at Los Alamos Neutron Science Center (LANSCE).
- Maintained hardware and troubleshot the fissionTPC during beam time, including Ethernet-based Data Acquisition (DAQ) hardware and NIM electronics.
- Updated fissionTPC gas handling system for mixing of (flammable) gases.
- Loaded radioactive samples into the fissionTPC inside a glovebox.
- Developed software for fissionTPC data analysis in both ROOT and stand-alone C++ modules, including neutron time-of-flight algorithms, data summary tree structures and macros for analysis of angular distributions and tracking performance.
- Wrote large-scale parallel data processing scripts in Bash to run on Lawrence Livermore National Laboratory Aztec supercomputer for fissionTPC data reconstruction.
- Measured fission fragment angular distributions in neutron-induced fission of ^{235}U with the NIFFTE fissionTPC.
- Measured Total Kinetic Energy (TKE) and masses of fission fragments at LANSCE using a Frisch-gridded ionization chamber and silicon surface barrier detectors. Supported instrument and DAQ system setup for the experiment.
- Wrote analysis software in ROOT for the TKE experiment.

01/2011 - 10/2012 **Graduate Research Assistant**, *Idaho State University, Department of Nuclear Engineering and Health Physics*, Pocatello, USA.

- Supported development of track reconstruction software for the fissionTPC in C++.
- Improved and validated fissionTPC detector simulation in C++ and Geant4.
- Benchmarked tracking performance in the fissionTPC through detector simulations and ROOT analysis.

10/2010 - 12/2010 **Junior Scientist**, *Austrian Center of Competence for Tribology*, Wiener Neustadt, Austria.

- Consulted on a novel system to measure wear on the nano-scale in automobile engines using previous experience in activation analysis and gamma detection.
- Derived all calibration equations for the experiment, taking into account fluid dynamics, neutron activation analysis and gamma detector response.

09/2009 - 05/2010 **Nuclear Safeguards and Security Trainee**, *European Commission, Institute for Transuranium Elements*, Karlsruhe, Germany.

- Measured the gamma masking effect of various isotopes for nuclear security and illicit trafficking applications using sodium iodide, high-purity germanium and cadmium zinc telluride gamma detectors.
- Improved and validated existing gamma detector simulations in MCNP.
- Supported software development for the Nucleonica nuclear science web-portal, including detector simulations and library creation software for various commercial gamma detectors.

Honors and Scholarships

2014 **L'Oréal For Women in Science Fellowship.** Awarded for research with the NIFFTE fissionTPC. L'Oréal Austria with the Austrian UNESCO Commission and the Austrian Academy of Sciences.

2011 **Marshall Plan Scholarship.** Awarded for research with the NIFFTE fissionTPC at Idaho State University. Austrian Marshall Plan Foundation.

2008 **ERASMUS Mobilitätsstipendium.** Scholarship for pursuing graduate coursework in Technical Physics at Uppsala University, Sweden. ERASMUS.

2008 **NÖ TOP Stipendium Ausland.** Scholarship for pursuing graduate coursework in Technical Physics at Uppsala University, Sweden. State Academy of Lower Austria.

2006 **NÖ TOP Stipendium Inland.** Awarded for passing the first diploma exam in Technical Physics at Vienna UT with distinction. State Academy of Lower Austria.

Professional Organizations

2009 - present **Austrian Nuclear Society** - Young Generation.

2009 - present **Students4Excellence** - Austrian high potentials mentoring programme.

2012 - present **American Physical Society** - Division of Nuclear Physics.

Outreach

04/2014 - present **LANL Bradbury Scientist Ambassador Academy.** Built and demonstrated a cloud chamber, gave regular talks to the public and school classes as part of a LANL outreach program with eight other scientists. Los Alamos, USA.

03/2010 **Sterne. Kerne. Teilchen.** Hosted an expert panel discussion on nuclear and particle physics for high school students. Wiener Neustadt, Austria.

Outside Interests

US National Ski Patrol (Alpine Patroller, Emergency Medical Responder and Instructor for Outdoor Emergency Care with the Pajarito Mountain Patrol).

Los Alamos Mountain Search and Rescue.

Long distance cycling.

Languages

German (native)

English (fluent)

List of Publications

Peer-reviewed

[1] M. Heffner, D. M. Asner, R. G. Baker, J. Baker, S. Barrett, C. Brune, J. Bundgaard, E. Burgett, D. Carter, M. Cunningham, J. Deaven, D. L. Duke, U. Greife, S. Grimes, U. Hager, N. Hertel, T. Hill, D. Isenhower, K. Jewell, J. King, J. L. Klay, V. Kleinrath, R. Kudo, N. Kornilov, A. B. Laptev, M. Leonard, W. Loveland, T. N. Massey, C. McGrath, R. Meharchand, L. Montoya, N. Pickle, H. Qu, V. Riot, J. Ruz, S. Sangiorgio, B. Seilhan, S. Sharma, L. Snyder, S. Stave, G. Tatishvili, R. T. Thornton, F. Tovesson, D. Towell, R. S. Towell, S. Watson, B. Wendt, L. Wood, and L. Yao. "A Time Projection Chamber for High Accuracy and High Precision Fission Cross Section Measurements". In: *Nuclear Instruments and Methods in Physics Research Section A: Accelerators, Spectrometers, Detectors and Associated Equipment* (2014).

[2] W. Loveland, L. Yao, D. Asner, R. Baker, J. Bundgaard, E. Burgett, M. Cunningham, J. Deaven, D. Duke, U. Greife, S. Grimes, M. Heffner, T. Hill, D. Isenhower, J. Klay, V. Kleinrath, N. Kornilov, A. Laptev, T. Massey, R. Meharchand, H. Qu, J. Ruz, S. Sangiorgio, B. Selhan, L. Snyder, S. Stave,

G. Tatishvili, R. Thornton, F. Tovesson, D. Towell, R. Towell, S. Watson, B. Wendt, and L. Wood. "Targets for Precision Measurements". In: *Nuclear Data Sheets* 119 (2014), pp. 383–385.

[3] R. Meharchand, D. Asner, R. Baker, J. Bundgaard, E. Burgett, M. Cunningham, J. Deaven, D. Duke, U. Greife, S. Grimes, M. Heffner, T. Hill, D. Isenhower, J. Klay, V. Kleinrath, N. Kornilov, A. Laptev, W. Loveland, T. Massey, H. Qu, J. Ruz, S. Sangiorgio, B. Seilhan, L. Snyder, S. Stave, G. Tatishvili, R. Thornton, F. Tovesson, D. Towell, R. Towell, S. Watson, B. Wendt, and L. Wood. "Commissioning the NIFFTE Time Projection Chamber: Towards the 238U / 235U (n, f) Cross-section Ratio". In: *Nuclear Data Sheets* 119 (2014), pp. 373 –376.

[4] S. Mosby, F. Tovesson, A. Couture, D. Duke, V. Kleinrath, R. Meharchand, K. Meierbachtol, J. ODonnell, B. Perdue, D. Richman, and D. Shields. "A fission fragment detector for correlated fission output studies". In: *Nuclear Instruments and Methods in Physics Research Section A: Accelerators, Spectrometers, Detectors and Associated Equipment* (2014).

[5] L. Snyder, D. Asner, R. Baker, J. Bundgaard, E. Burgett, M. Cunningham, J. Deaven, D. Duke, U. Greife, S. Grimes, M. Heffner, T. Hill, D. Isenhower, J. Klay, V. Kleinrath, N. Kornilov, A. Laptev, W. Loveland, T. Massey, R. Meharchand, H. Qu, J. Ruz, S. Sangiorgio, B. Seilhan, S. Stave, G. Tatishvili, R. Thornton, F. Tovesson, D. Towell, R. Towell, S. Watson, B. Wendt, and L. Wood. "Measuring the α/SF Branching Ratio of 252Cf with the NIFFTE TPC". In: *Nuclear Data Sheets* 119 (2014), pp. 386 –388.

[6] S. Stave, D. Asner, R. Baker, J. Bundgaard, E. Burgett, M. Cunningham, J. Deaven, D. Duke, U. Greife, S. Grimes, M. Heffner, T. Hill, D. Isenhower, J. Klay, V. Kleinrath, N. Kornilov, A. Laptev, W. Loveland, T. Massey, R. Meharchand, H. Qu, J. Ruz, S. Sangiorgio, B. Seilhan, L. Snyder, G. Tatishvili, R. Thornton, F. Tovesson, D. Towell, R. Towell, S. Watson, B. Wendt, and L. Wood. "The Data Analysis Framework for the NIFFTE Fission Time Projection Chamber". In: *Nuclear Data Sheets* 119 (2014), pp. 380 –382.

[7] L. Wood, D. Asner, R. Baker, J. Bundgaard, E. Burgett, M. Cunningham, J. Deaven, D. Duke, U. Greife, S. Grimes, M. Heffner, T. Hill, D. Isenhower, J. Klay, V. Kleinrath, N. Kornilov, A. Laptev, W. Loveland, T. Massey, R. Meharchand, H. Qu, J. Ruz, S. Sangiorgio, B. Seilhan, L. Snyder, S. Stave, G. Tatishvili, R. Thornton, F. Tovesson, D. Towell, R. Towell, S. Watson, and B. Wendt. "An Ethernet-based Data Acquisition System for the NIFFTE Time Projection Chamber". In: *Nuclear Data Sheets* 119 (2014), pp. 377 –379.

[8] J. Ruz, D. M. Asner, R. G. Baker, J. Bundgaard, E. Burgett, M. Cunningham, J. Deaven, D. L. Duke, U. Greife, S. Grimes, M. Heffner, T. Hill, D. Isenhower, J. L. Klay, V. Kleinrath, N. Kornilov, A. B. Laptev, W. Loveland, T. N. Massey, R. Meharchand, H. Qu, S. Sangiorgio, B. Seilhan, L. Snyder, S. Stave, G. Tatishvili, R. T. Thornton, F. Tovesson, D. Towell, R. S. Towell, S. Watson, B. Wendt, and L. Wood. "The NIFFTE project". In: *Journal of Instrumentation* 8.12 (2013).

Proceedings and Reports

[9] V. Kleinrath. "Particle Tracking Development for a Fission Time Projection Chamber". In: *Transactions of the American Nuclear Society* 106 (2012), pp. 909–911.

[10] V. Kleinrath. *Precision Fission Cross Section Measurements using a Time Projection Chamber*. Tech. rep. Final Scholarship Report. Vienna, Austria: Austrian Marshall Plan Foundation, 2012.

[11] V. Kleinrath. "A Study of Gamma Interference Scenarios for Nuclear Security Purposes". MA thesis. Vienna University of Technology, 2010.

[12] V. Kleinrath. *A Study of Gamma Interference Scenarios for Nuclear Security Purposes*. Tech. rep. JRC-ITU-TN-2010/21. Karlsruhe, Germany: Institute for Transuranium Elements, European Commission Joint Research Center, 2010.

[13] V. Kleinrath. "A Study of Gamma Interference Situations for Nuclear Security Purposes - Experiments and Simulations using the Nucleonica Tools". In: *Proceedings of the 2010 International Youth Nuclear Congress, Capetown, South Africa*. IYNC. 2010.

[14] V. Kleinrath, R. Arlt, A. Berlizov, and J. Magill. "Application of Nucleonica's Gamma Spectrum Generator and easyMonteCarlo simulation tools on nuclear security issues". In: *Nuclear Science Symposium Conference Record (NSS/MIC), 2010 IEEE*. IEEE. 2010, pp. 900–901.

[15] V. Kleinrath. *Determination of Radioactivity of Concrete Samples with Longitudinal Direction of the Biological Shield of the ASTRA - Reactor Seibersdorf*. Tech. rep. AIAU–28310. Vienna, Austria: Atominstitut of the Austrian Universities, 2008.

[16] V. Kleinrath. *Determination of Radioactivity of Concrete Samples with Transversal Direction of the Biological Shield of the ASTRA - Reactor Seibersdorf*. Tech. rep. AIAU–28309. Vienna, Austria: Atominstitut of the Austrian Universities, 2008.

Selected Conference Talks and Seminars

05/2015 **Active Targets and TPC for Nuclear Physics Experiments Workshop**, East Lansing, USA. "Precision Nuclear Data Measurements with the NIFFTE fissionTPC."

04/2015 **LANL Informal Seminar Series on Experimental Data and Their Uncertainty Quantification**, Los Alamos, USA. "Fission Fragment Angular Distributions measured with a Time Projection Chamber."

09/2014 **LANL FIESTA Nuclear Fission School and Workshop**, Santa Fe, USA. "Fragment Angular Distributions in Neutron-Induced Fission of ^{235}U and ^{239}Pu using a Time Projection Chamber" (poster presentation).

12/2012 **LANSCE Nuclear Science Seminar**, Los Alamos, USA. "Fission Yield Measurements with Incident Neutron Energy using a Time Projection Chamber."

06/2012 **American Nuclear Society Annual Meeting**, Chicago, USA. "Particle Tracking Development for a Time Projection Chamber."

12/2010 3rd **IAEA Research Coordination Meeting (CRP 22.007)**, IAEA, Vienna, Austria. "A Study of Gamma Interference Scenarios for Nuclear Security Purposes."

11/2010 **IEEE Nuclear Science Symposium**, Knoxville, USA. "Application of Nucleonica's Gamma Spectrum Generator and easyMonteCarlo Simulation Tools on Nuclear Security Issues."

10/2010 **NuTroNS, Joint IAEA/European Commission Training Course on Nuclear Science**, Monaco. Invited: "Gamma Library Creation using Nucleonica" (1st talk) and "The mysterious Ba-133 Case - Applying the Nucleonica Tools onto a realistic Nuclear Security Issue" (2nd talk).

07/2010 **International Youth Nuclear Congress**, Cape Town, South Africa. "A Study of Gamma Interference Situations for Nuclear Security Purposes - Experiments and Simulations using the Nucleonica Tools."

11/2009 2nd **Advanced Training Course on Illicit Trafficking and Consequence Management with Nucleonica**, European Commission, Institute for Transuranium Elements, Karlsruhe, Germany. "Interference Situations in Gamma Spectrometry."

09/2009 2nd **IAEA Research Coordination Meeting (CRP 22.007)**, IAEA, Vienna, Austria. "The Nucleonica Gamma Spectrum Generator and its possible Nuclear Security Applications."

References

Fredrik Tovesson, PhD. PhD co-advisor and LANL mentor.
Acting Group Leader, P-27 LANSCE Weapons Physics
Los Alamos National Laboratory
tovesson@lanl.gov
+1 505 665 9652

Helmut Leeb, PhD. PhD advisor.
Team Leader AG Kernphysik, Atominstitut
Dean of Studies, Technical Physics
Vienna University of Technology
helmut.leeb@tuwien.ac.at
+43 1 58801 142101

Lucas A. Snyder, PhD. Collaborator on the NIFFTE fissionTPC.
Staff Scientist, Nuclear and Chemical Sciences Division
Lawrence Livermore National Laboratory
snyder35@llnl.gov
+1 925 422 1794

Additional references available upon request.

Updated December 16, 2015.